

Unterschrift des Betreuers



TECHNISCHE
UNIVERSITÄT
WIEN

DIPLOMARBEIT

ATR FTIR Spectroscopy for *In Situ* Monitoring of Protein Interaction with Mesoporous Silica Films

ausgeführt am

Institut für Chemische Technologien und Analytik
der Technischen Universität Wien

unter der Anleitung von

Univ.Prof. Dipl.Ing. Dr.techn. Bernhard Lendl
und Projektass. Dipl.Ing. Bettina Baumgartner

durch

Sophia Steinbacher, Bsc

01225591

Am Zimmerplatz 37

A-3343 Hollenstein an der Ybbs

Wien, am 28.2.2019

„Die Wissenschaft fängt eigentlich erst da an interessant zu werden,
wo sie aufhört.“

Justus von Liebig (1803-73), dt. Chemiker

meiner liebevollen Familie

Acknowledgments

First of all, I am gratefully thankful for my parents and my family for supporting me in every aspect of life, and loving me just the way I am. I want to thank Christoph for being always there for me and for showing me, that life is more than just studies. Thanks to all my colleagues, who became friends over the last years. Without, I wouldn't have made it.

I am thanking Bettina for giving me all her knowledge and support for performing this thesis.

As well as great thanks to Bernhard for making this project possible.

Abstract

Within this thesis a method for the *in situ* monitoring of the adsorption of proteins from aqueous solutions into mesoporous silica supports, was established. Therefore, mesoporous silica films were coated onto ATR crystals for their later implementation in ATR FTIR spectroscopy. Films were prepared using a sol-gel process in combination with an evaporation induced self-assembly approach. Here the formation of mesoporous films with a thickness of ~600 nm and ~15 nm in pore size using Pluronic F127 as surfactant was accomplished. The proteins Lysozyme and Lipase from *Candida rugosa* were used for performing adsorption experiments on prepared films monitored by ATR FTIR spectroscopy. The preparation of a stable film and the application of theoretical basics of ATR spectroscopy allowed to ascertain the protein being inside the pores. Lipase from *Candida rugosa* showed adsorption inside the methylated mesoporous silica film with 15 nm in pore size. Thereby, low concentrations of Lipase in buffer solution (pH 7) ranging from 0.025 - 0.5 mg/mL were detectable. First approaches showed a linear correlation between obtained absorbance and applied concentration. Furthermore, attempts towards monitoring the activity of lipase inside the porous structure were performed.

Hence, throughout the preparation of a stable mesoporous silica films on an ATR crystal the interaction of proteins with mesoporous silica can be followed by FTIR spectroscopy. Thereby, first steps towards a potential detection method for low concentrations of proteins in aqueous media were accomplished.

Kurzfassung

Im Rahmen dieser Diplomarbeit wurde eine Methode für die Untersuchung der Adsorption von Proteinen aus wässriger Lösung in mesoporöse Siliciumdioxidschichten mittels ATR FTIR Spektroskopie etabliert. Für die Herstellung von hoch geordneten porösen Silica Schichten auf ATR Kristallen wurde ein Sol-Gel Prozess in Kombination mit einer induzierten Selbstassemblierung von Tensiden verwendet. Durch die Optimierung der Synthese konnten Schichten, mit einer Höhe von ~600 nm und einer Porengröße bis zu ~15 nm erzielt werden. Für die Adsorptionsversuche wurden die Proteine Lysozyme und Lipase (*Candida rugosa*) verwendet. Durch die Grundlagen der ATR Spektroskopie in Kombination mit der Bereitstellung von stabilen porösen Schichten, konnten Berechnungen bezüglich des Eintritts der Proteine in die Poren angestellt werden. Dadurch wurde die Adsorption von Lipase in methylierte Silica Schichten mit 15 nm Porengröße bewiesen. Durch die Anreicherung von Lipase in den Poren, konnten in weiterer Folge geringe Konzentrationen von 0.0025 - 0.5 mg/mL detektiert werden, wobei erste Messungen einen linearen Zusammenhang zwischen Konzentration und erhaltenem Signal aufwiesen. Des Weiteren wurden erste Versuche hinsichtlich der Verfolgung der Aktivität von Lipase in den Poren mittels FTIR Spektroskopie angestellt.

Im Rahmen dieser Diplomarbeit wurde, eine neue Möglichkeit für die Untersuchung der Interaktion von Proteinen mit Mesoporösen Silicaten etabliert. Durch die Anreicherung von Proteinen in der Schicht konnte ein erster Weg Richtung die Detektierung von Proteinen in geringen Konzentrationen mittels ATR FTIR Spektroskopie entwickelt werden.

List of Abbreviations

A	absorbance
ATR	attenuated total reflection
A.U.	absorption units
a.u.	arbitrary units
CMC	critical micelle concentration
CTAB	cetyltrimethylammoniumbromid
EISA	Evaporation Induced Self-Assembly
F127	Pluronic® F127 (PEO ₁₀₆ -PPO ₇₀ -PEO ₁₀₆)
FTIR	fourier transform infra red
H	hours
HMDS	hexamethyldisilazane
I	intensity
IRS	internal reflection setup
kDa	kilo Dalton
λ	wavelength
LCR	Lipase from <i>Candida rugosa</i>
LYS	Lysozyme
mid -IR	mid infrared
MW	molecular weight
MTES	methyltriethoxysilane
N	active bounces inside ATR crystal
n	refractive index
o/n	over night
PEG	poly ethylenglycol
PEO /PPO	poly ethylene oxide / poly propylene oxide
pI	isoelectric point
PMMA	polymethylmethacrylate
PZC	point of zero charge
RT	room temperature
Si	silicon
silica	silicondioxide
t	time
th	thickness
TEOS	tetraethylorthosilicat
TGA	thermogravimetric analysis
UV	ultra violet
$\tilde{\nu}$	wavenumber
ν	frequency
X-rays	electromagnetic radiation (0,25 x 10 ¹⁸ Hz – 60 x 10 ¹⁸ Hz)

Contents

<i>Acknowledgments</i>	<i>vi</i>
<i>Abstract</i>	<i>vii</i>
<i>Kurzfassung</i>	<i>viii</i>
<i>List of Abbreviations</i>	<i>ix</i>
1. Motivation	1
2. Theoretical Part	3
2.1 Synthesis of Mesoporous Silica Films	3
2.1.1 General Reaction Mechanism of the Sol-Gel Process.....	3
2.1.2 Formation of Mesoporous Silica <i>via</i> Evaporation Induced Self-Assembly (EISA).....	6
2.1.3 Post and Co-Functionalization of Mesoporous Silica	9
2.2 Principles of ATR FTIR Spectroscopy	11
2.2.1 A Short Introduction to Mid Infrared Spectroscopy	11
2.2.2 Quantification through Beer's Law	12
2.2.3 Basics of Attenuated Total Reflection FTIR Spectroscopy.....	13
2.3 Infrared Spectroscopy of Proteins	16
2.3.1 Characteristic Vibrational Bands of Proteins	17
2.3.2 Experimental Aspects of Protein FTIR Spectroscopy in Aqueous Solutions.....	18
3. Considerations, Results and Discussion	20
3.1 Considerations	20
3.1.1 Considerations of the Determination of the Protein Inside the Pore	21
3.1.2 Considerations Concerning the Interaction of Proteins with Mesoporous Silica Surfaces.....	26
3.1.3 Characteristics of the Used Proteins	27
3.2 Formation of Mesoporous Silica Thin Films with Large Pore Sizes	29
3.2.1 Proof of Concept: Film Synthesis Using CTAB as Template	29
3.2.2 Synthesis of Thick Mesoporous Films with Large Pore Sizes Using Pluronic F127	31
3.2.3 Evaluation of the Stability of the Mesoporous Silica Films in Buffer	33
3.3 Protein Adsorption on Mesoporous Silica Monitored by ATR FTIR Spectroscopy ...	37
3.3.1 Workflow for Protein Adsorption Experiments.....	37
3.3.2 Protein Adsorption Experiments on Uncoated Silica Surfaces.....	39
3.3.3 Protein Adsorption Experiments on Unfunctionalized Mesoporous Silica Films.....	41
3.3.4 Protein Adsorption Experiments on Methylated Silica Surfaces	43
3.3.5 Protein Adsorption Experiments with Methylated Mesoporous Silica Films.....	48

3.3.6	Detection of Lipase at Low Concentrations	53
3.3.7	Approaches towards Activity Monitoring of LCR in Silica Pores and on Silica Surfaces	55
4.	<i>Conclusion</i>	58
5.	<i>Experimental Part</i>	59
5.1	Optical Setup	59
5.1.1	Spectra and Data Processing	60
5.2	Materials and Methods	61
5.2.1	Chemicals.....	61
5.2.2	Spin coating and Dip coating	61
5.2.3	Characterization of Mesoporous Silica Films.....	62
5.3	Synthesis of the Mesoporous Silica Films	63
5.3.1	Synthesis of Silica Films Using CTAB as Surfactant	63
5.3.2	Synthesis of Silica Films Using F127 as Surfactant	63
6.	<i>References</i>	78

1. Motivation

Million years of evolutionary fine-tuning formed various enzymes catalyzing diverse chemical reactions as *e.g.* hydrolases performing hydrolysis reactions. In contrast to chemical catalysts, enzymes are designed to work under ambient conditions, and to exhibit high chemo-, regio-, and stereo-selective properties [1]. Therefore, their exploitation in biotechnological applications shows great potential for novel, more environmentally friendly and more economical industrial processes. But, one major drawback for the usage of enzymes in bio catalysis is their limited reusability, which arises from low structural stability under harsh conditions *e.g.* organic solvents, or temperatures $> 50^{\circ}\text{C}$. Throughout immobilization on solid substrates, enzymes show higher tolerance against extreme pH, elevated temperature, higher ionic strength and against organic solvents, compared to unprotected enzymes. In addition, throughout immobilization on high-surface area materials new possibilities concerning enzyme reusability arise [2]. There is a variety of immobilization supports, such as organic polymers *e.g.* biopolymers, synthetic polymers or inorganic material as metal oxides or carbon-based materials [3]. In particular, silica is one of the most frequently employed inorganic support and it shows advantages, such as high chemical and thermal resistance as well as the broad spectrum of possible surface modifications *via* functionalization [4]. In the last decades, especially mesoporous silica particles drew more and more attention as a support to immobilize enzymes for bio catalysis, biosensing or drug delivery [5].

A benefit of mesoporous silica with pore sizes in the range between 2-50 nm is a possible high enzyme loading. The porous structure forms a protective environment for the protein. Monitoring the immobilization process of enzymes into the pores is important to determine efficiency of protein loading and the protein-silica affinity. Common analytical methods for monitoring immobilization, are mainly indirect as they just trace *e.g.* the decrease of free space within the material's pore, but not the presence of protein [6] or analyzing the protein content in remaining supernatant [7]. The used methods for determination of the protein content on porous particles are: (i) N_2 adsorption [7,8], (ii) X-ray diffraction [8], (iii) Fourier transform infrared spectroscopy (FTIR) of particles [8], (iv) thermogravimetric analysis (TGA) [10] as well as (v) simple optical measurements of the supernatant after immobilization of the protein on the support *e.g.* measuring the UV absorption at 280 nm [11].

However, all of these indirect methods do not provide direct experimental evidence of the actual location of the enzyme. Hence, if the protein is solemnly adsorbed on the particle surface or if it is actually located inside a pore.

By now, two imaging methods to determine the protein location in mesoporous silica were reported: (i) in 2004 CHANG Woo Suh *et al.* labeled proteins with a fluorescent dye with later investigation by fluorescence microscopy [12] and (ii) in 2011 by Monica PIRAS *et al.* combined transmission electron microscopy with post-embedding immunogold staining (IGS) [13]. These methods require either protein modification (dye labeling) or additional antibodies, laborious preparation as well as the natural environment of the protein gets lost during measurement. In 2013, HARTMANN and ZHOU additionally stated that there is a gap of knowledge in the understanding of how surface properties of the support effect enzyme immobilization and activity [14].

The aim of this work was to establish a method to determine protein adsorption into mesoporous silica by the combination of mesoporous silica films with attenuated total reflection (ATR) FTIR spectroscopy. Based on quantitative analysis established for small molecules by Baumgartner *et al.* [15], theoretical considerations for the ratio of protein adsorbed on the surfaces versus within the film were retrieved. Therefore, a statement concerning the definite protein location (adsorbed on the surface or located inside a pore) can be performed. Since the protein adsorption is limited by the pore diameter of the mesoporous film, the synthesis of film with large pores (> 10 nm) was optimized and accomplished. The obtained films were thoroughly characterized by FTIR spectroscopy, X-ray diffraction, ellipsometric porosimetry and their stability towards physiological solutions was determined.

In summery, a platform for deepening the understanding of the adsorption of proteins from aqueous solutions into mesoporous silica supports, as well as the possibility to investigate proteins at low concentrations as well as their activity inside the pores was established.

2. Theoretical Part

This chapter provides the theoretical background of the main topics within this thesis. In **section 2.1** the basics for the synthesis of mesoporous silica films *via* the sol-gel process are presented. Secondly, theoretical basics of mid-IR Spectroscopy with focus on ATR spectroscopy are given in **section 2.2**. The specific characteristics of FTIR spectroscopy of proteins within the mid-IR region are presented in **section 2.3**.

2.1 Synthesis of Mesoporous Silica Films

Mesoporous silica films are mainly prepared *via* the sol-gel process. This is a method to synthesize solid materials by condensation and gelation of small precursor molecules (typically metal alkoxides $M(OH)_x$) out of solution [16]. In the case of silica (silicon dioxide), silicon alkoxides precursors ($Si(OR)_4$) form the solid network throughout progressive hydrolysis and polycondensation.

This chapter is divided into the general reaction mechanism of the sol-gel process (**section 2.1.1**) and the synthesis method for mesoporous silica films *via* the Evaporation Induced Self-Assembly (EISA) process (**section 2.1.2**). Since the versatility of functionalization of silica materials is unique the possible ways for modification are given in **section 2.1.3**.

2.1.1 General Reaction Mechanism of the Sol-Gel Process

In sol-gel chemistry, metal oxide networks are obtained through progressive hydrolysis and polycondensation of metalalkoxides. Starting from molecules in solution, the networks are formed by going through a sol and a gel stage. SCHUBERT *et al.* defined the two terms as [17]:

“A ***sol*** is a stable suspension of colloidal particles of polymers in a liquid.”

“A ***gel*** consists of a porous, three-dimensionally continuous solid network surrounding and supporting a continuous liquid phase (“wet gel”).”

The first step in a sol-gel process is the hydrolysis of Si-OR to Si-OH (see **Figure 1 (1)**). The formed silicon hydroxyl moieties further react by a condensation reaction **(2)**. Here, either a silicon alkoxide or a silicon hydroxide species acts as reaction partner and upon cleaving of one alcohol or water molecule the Si-O-Si bond is formed.

2.1.1 General Reaction Mechanism of the Sol-Gel Process

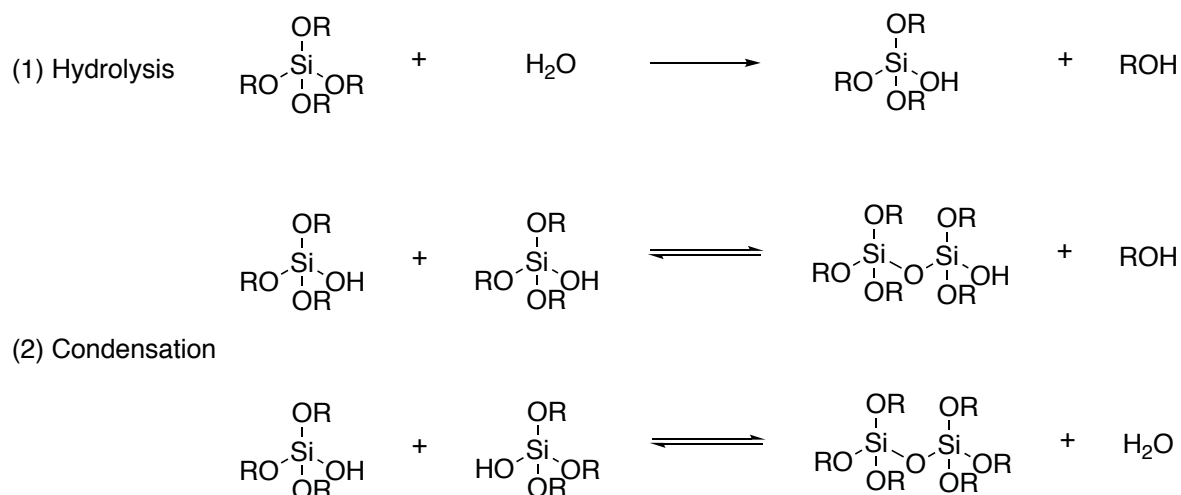


Figure 1: Scheme of the reaction equations of the sol-gel process. (1) Hydrolysis and subsequent (2) condensation with $R =$ alkyl chain e.g. in (1) $R = \text{C}_2\text{H}_5$ for tetraethylorthosilicate (TEOS), in (2) $R = \text{H}$ or $R = \text{C}_2\text{H}_5$ depending on the degree of hydrolysis.

The formed oligomers undergo further condensation and in order to obtain a network, the number of siloxane (Si-O-Si) bonds has to be maximized. The kinetics of the ongoing reactions can be altered through modification of reaction conditions e.g. pH or temperature.

The initial hydrolysis reaction can be catalyzed *via* acidic or basic conditions. At $\text{pH} < 3$, the oxygen atom adjacent to the silicon is protonated, forming a good leaving group. Now a nucleophilic attack on the free electron pair of the oxygen at the silicon atom can occur (condensation reaction). In the case of basic catalysis, the reaction follows an S_{N}^2 -type nucleophilic substitution mechanism. Besides the difference in reaction mechanism forming the siloxane bond, the reversibility of the condensation reaction is also pH dependent. Under basic conditions the condensation reaction is in principle of reversible character, whereas at acidic pH the reaction can be classified as non-reversible.

The ongoing polycondensation reactions lead to the formation of larger particles or a network in solution. This process, where a sol (suspension of particles) to gel (continuous solid network) transition occurs is classified as gelation, which is visualized in **Figure 2**.

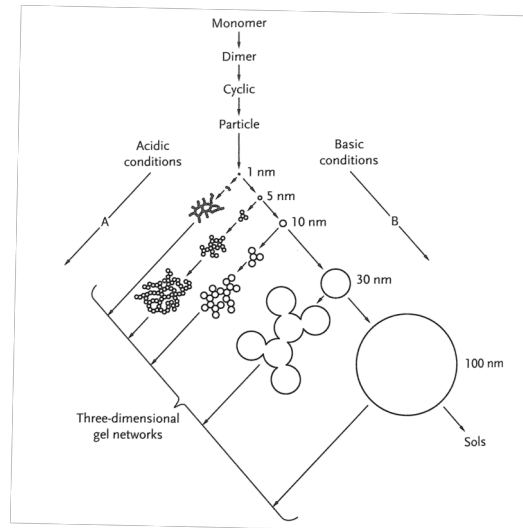


Figure 2: Scheme of the structural development of silica gels. Going from small particles in solution (sol) to (A) under acidic conditions a continuous porous network or (B) under basic conditions forming larger particles in the sol. Adapted from [17]

As illustrated in **Figure 2**, the pH value of the solution influences shape and the structural development of the silica gel: Under basic conditions, condensation reactions are faster than hydrolysis, which leads to the formation of spherical particles. Whereas under acidic conditions hydrolysis of silicon alkoxides is much faster than condensation. This induces the formation of small oligomeric species (clusters), which later form three-dimensional gel networks.

Note that after gelation, the network is not finished since in wet-gels (gels containing liquid in their pores), structural rearrangements take place. These rearrangements are defined as the aging process, which takes place until all liquid is completely removed. This is performed by drying, which can be performed by *e.g.* increasing temperature or decreasing pressure. During this last process step the network becomes increasingly stiffer as well as shrinkage occurs.

This formation process of solids out of solution at ambient conditions, allows for processing metal oxides into different shapes. For example, the sol-gel process is frequently used for the synthesis of a thin film. Here, the two most common film casting techniques are spin coating and dip coating. These methods allow for the formation of thin silica films with controlled pore sizes when using a template as pore forming agent. A special templating method using a surfactant for pore formation is the Evaporation Induced Self-Assembly (EISA) approach. This method for the synthesis of mesoporous thin films will be presented in the next **section 2.1.2**.

2.1.2 Formation of Mesoporous Silica *via* Evaporation Induced Self-Assembly (EISA)

Self-assembly is an ubiquitous phenomenon, where structures are formed spontaneously by non-covalent interactions as *e.g.* hydrogen bonding, Van der Waals forces, electrostatic forces, etc. [18]. WHITESIDES and GRZYBOWSKI defined self-assembly as follows [19]:

“Self-assembly is the autonomous organization of components into patterns of structures without human intervention. Self-assembling processes are common throughout nature and technology. They involve components from the molecular (crystals) to the planetary (weather systems) scale and many different kinds of interactions.” - (G. M. Whitesides and B. Grzybowski, *Science* **2002**, 295, 2418.)

In aqueous systems, with concentration above the critical micelle concentration (CMC), amphiphilic compounds, as *e.g.* ionic surfactants, self-assembly leads to different supramolecular structures. These so called mesophases are an intermediate between liquid and solid and are for example found in gelatin or the lipid bilayer in cells.

For the ionic surfactant cetyltrimethylammonium bromide (CTAB) a scheme of the phase diagram depending on temperature and surfactant concentration is given in **Figure 3**.

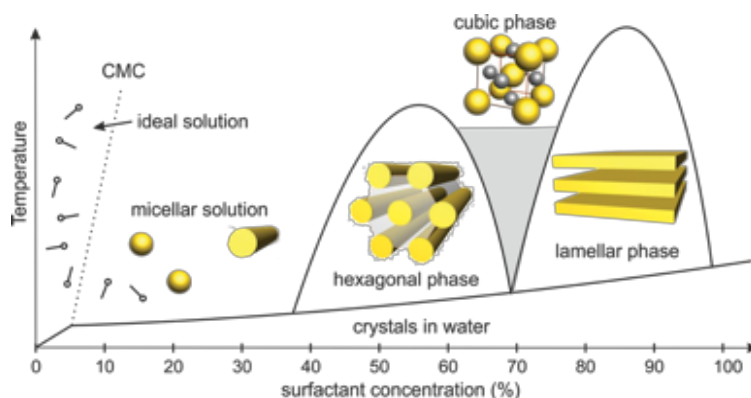


Figure 3 Schematic phase diagram of an aqueous solution of CTAB showing the influence of surfactant concentration and temperature on the formation of different mesophases. At low concentration below the critical micelle concentration (CMC) an ideal solution of the surfactant is present. If the concentration is increased first a micellar solution and later different mesostructures as *e.g.* hexagonal, cubic or lamellar structured phases are obtained.

The obtained mesophases are liquid crystals, since they pose typical characteristics of a liquid (*e.g.* fluidity) as well as certain crystalline properties as *e.g.* periodic arrangement of molecules [20]. In 1992, KRESGE *et al.* reported the combination of the sol-gel process with the self-assembly of amphiphilic compounds for the synthesis of mesoporous silica materials. They calcined aluminosilicate gels in presence of surfactants and obtained regular arrays, and

channels within the material. For the formation process they proposed a liquid crystal (mesophase) templating mechanism, where the silica network is formed between ordered surfactant micelles. This approach was also used for the formation of mesoporous silica films by BRINKER *et al.* [18]. Through the self-assembly process taking place during deposition of a surfactant containing silica sol, highly ordered mesoporous structures are obtained. This Evaporation Induced Self-Assembly (EISA) process, evolved to a versatile preparation method of metal oxide thin films with tunable regular pore sizes within the mesoporous regime ranging from 2-50 nm [21],[22].

For the formation of thin films there are two common processing methods: (i) spin coating and dip coating [23]. During dip coating, the substrate is immersed in the coating solution. After a certain dwell time, the substrate is pulled out with a defined velocity and a thin layer is formed. For spin coating, the substrate is rotated, and a small amount of solution is deposited on top. Through constant spinning, a thin layer is formed on the surface. The processes during EISA using spin coating as deposition method and an ionic surfactant *e.g.* CTAB as template, are schematically visualized in **Figure 4**.

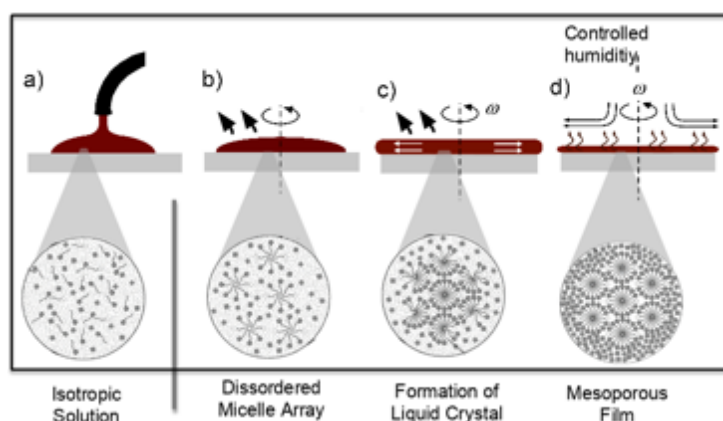


Figure 4: Scheme of spin coating of a sol for the formation of mesoporous silica films via EISA. a) Application of sol on substrate surface b) rotation of substrate and evaporation of solvent, c) micellar mesostructures are formed d) silicon dioxide network is formed while humidity is adjusted to control formation process.

Firstly, a small amount of the sol solution containing an *e.g.* ionic surfactant is deposited on top of a substrate. As spinning is started, the solvent *e.g.* ethanol continuously evaporates, hence the concentration of the surfactant increases as well as silica condensation is proceeding. At a certain point, surfactant concentration exceeds CMC and different liquid-crystalline phases (mesophases) are formed. Throughout ongoing condensation of hydrolyzed precursors and silica oligomers, the silica network is formed around the micelles, forming the mesostructure. If the template (surfactant) is removed by *e.g.* calcination, a solid silica network in the shape of the liquid crystal is obtained.

2.1.2 Formation of Mesoporous Silica *via* Evaporation Induced Self-Assembly (EISA)

The equilibrium between kinetics of the organization of the mesophases and the kinetics of condensation, are crucial for the formation of the resulting ordered silica network. Both are influenced by kinetics of diffusion and evaporation of volatile species during film processing. Controlling these kinetic processes is difficult, since they happen simultaneously. It was discovered that throughout adjusting relative humidity the rate of evaporation of volatile compounds in the film can be trimmed and furthermore, the condensation rate of silica is influenced. An equilibrium between the liquid water (in the film) and water vapor in the gas phase is established, which allows for the formation of the final mesostructure. Especially for ionic-surfactants *e.g.* CTAB, relative humidity (RH) during film deposition, was found to be essential to control the final structure of silica films [22]. Using CTAB as surfactant different mesostructured silica films *e.g.* 3D hexagonal, cubic with pore sizes of 2-5 nm can be synthesized.

Besides ionic surfactants, other surfactants *e.g.* non-ionic, amphiphilic triblock copolymers are used allowing for synthesizing pore sizes up to 20 nm. As for example DUNPHY *et al.* (2014) reported the synthesis of mesoporous silica films with pore sizes up to 15 nm by the use of different poloxamers as template [24]. Poloxamers are block-co-polymers consisting of poly ethylene oxide (PEO) and poly propylene oxide (PPO) blocks with variable block chain length and variable molecular weight.

HOLMQVIST *et. al* investigated the behavior of Pluronic® F127, a commercially available amphiphilic triblock copolymer (poloxamer) with the distinct formula (PEO₁₀₆-PPO₇₀-PEO₁₀₆) in water and butanol mixtures. The resulting phase diagram is given in **Figure 5** [25].

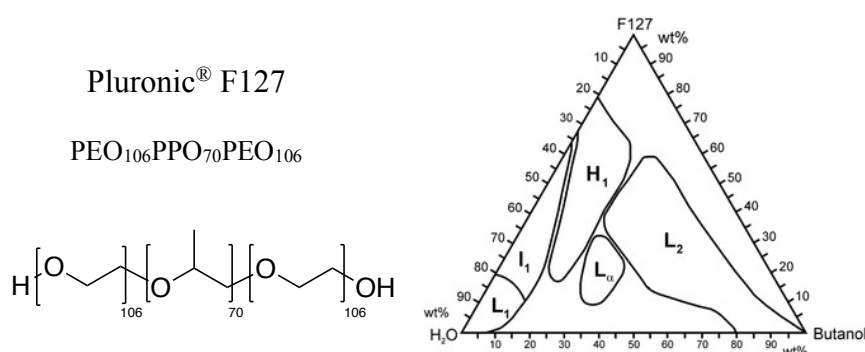


Figure 5: Distinct structure formula of the poloxamer Pluronic® F127. Ternary phase diagram of Pluronic® F127, butanol and water mixtures at 25°C showing the different mesophases: L_α ... Lamellar; L₁ ... normal micellar; L₂ ... reverse micellar; I₁ normal micellar cubic and H₁ ... normal hexagonal. Adapted from [25].

As visible in the ternary phase diagram of F127 in **Figure 5**, different mesophases are formed depending on the concentration of water and butanol. Lamellar (L_α), normal micellar (L₁), reverse micellar (L₂), I₁ normal micellar cubic (I₁) and normal hexagonal (H₁) phases can be

obtained by adjusting right weight ratios. For the EISA process these phase diagrams can be used to derive possible surfactant concentrations needed in the sol for the synthesis of defined structures. Indeed, HOLMQVIST *et al.* reported that the phase diagrams obtained for water/BuOH/F127 were very similar to the ones obtained in the presence of silica [25]. Hence, through the implementation of different templating molecules, pore sizes can be trimmed. Whereas through variation of the surfactant concentration, different mesophases are formed and thereby different 3D structures of a mesoporous silica network are possible.

Besides structural variability, silica chemistry allows for modification of surface properties through functionalization. Organic moieties can be either introduced during formation of the silica network (co-condensation) or afterwards (post-synthesis functionalization). Both approaches are discussed in **section 2.1.3**.

2.1.3 Post and Co-Functionalization of Mesoporous Silica

Silica chemistry allows for the modification with organic groups by covalent linkage formed through the reaction of silica species with *e.g.* organoalkoxysilanes (RSi(OR')_3), chlorosilanes (RSiCl_3) or other silazanes as *e.g.* hexamethyldisilazane (HMDS). Throughout different synthesis approaches different organic moieties can be introduced into mesoporous silica: (i) functionalization by co-condensation of tetraalkoxysilanes (Si(OR)_4) and organoalkoxysilanes (RSi(OR')_3) in a one-pot synthesis or (ii) a post-synthesis functionalization by grafting of the silica network using *e.g.* organoalkoxysilanes (RSi(OR')_3), chlorosilanes (RSiCl_3) or silazanes. The two different reaction routes are visualized by giving a precise example for a co-condensation approach (**Figure 6**) and a post-synthetic approach (**Figure 7**).

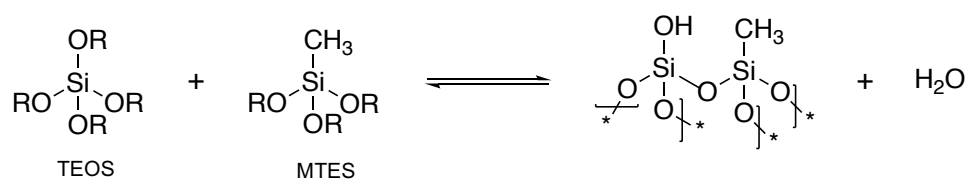


Figure 6: Scheme of the co-condensation reaction with $\text{R} = -\text{C}_2\text{H}_5$, or $-\text{H}$ depending on the degree of hydrolysis. TEOS and MTES forming a silicon dioxide network functionalized with methyl groups.

For co-condensation, the silicon dioxide network is formed through hydrolysis and subsequent condensation of an organotrialkoxysilane *e.g.* methyltriethoxysilane (MTES) and tetraalkoxysilane *e.g.* tetraethoxysilane (TEOS) (see **Figure 6**). Here, the organic moiety is directly inserted into the material during its synthesis and the degree of *e.g.* methylation is directly dependent on the initial TEOS:MTES ratio, allowing for methylation of up to 50 % (1:1 ratio).

2.1.3 Post and Co-Functionalization of Mesoporous Silica

The larger the alkyl chain and the higher the concentration of organotrialkoxysilane, the more deviating is the system from the standard conditions in mesoporous silica synthesis. Especially for the EISA process the functional moieties may disrupt the mesophases self-assembly process, and therefore the formation of mesostructures can be hindered [26]. In addition, it has to be considered that post heat treatment for drying of the silica network at elevated temperatures, *e.g.* calcination, may remove the just introduced moiety. Hence, functionalization of mesoporous silica films *via* co-condensation is limited.

Therefore, the post-synthesis route is frequently used for modifications with more structural demanding organic functionalities. Unreacted silanol groups on the surface are brought to reaction with alkoxy silanes ($\text{RSi}(\text{OR}')_3$), chlorosilanes (RSiCl_3) or other silazanes as *e.g.* hexamethyldisilazane (HMDS) forming a covalently bonded organic moiety.

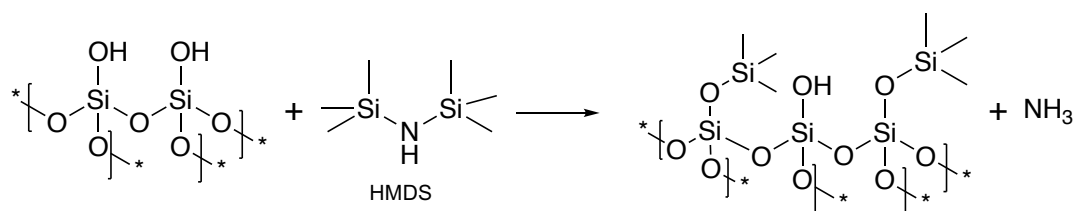


Figure 7: Scheme of the grafting reaction of silicium dioxide network with HMDS to obtain a methylated surface. Silanol groups are reacting with the silazane species forming novel organic moieties on the silica surface.

A scheme of the silica grafting is given in **Figure 7**, where HMDS is used as functionalizing agent. Note that the diversity of commercially available silanes is broad, because the same chemistry is used for modification of silica column material in chromatography, *e.g.* HPLC, and GC. Reaching from methyl-, amino- and sulfo- functionalized organotrialkoxysilanes as well as more complex organoalkoxysilanes with *e.g.* crown ether or porphyrin moieties are available. Hence, the mesoporous thin films can be adjusted in terms of *e.g.* charge, hydrophobicity/hydrophilicity as well as towards other more specific functionalities.

Since in this thesis the interaction of proteins with mesoporous silica films will be monitored with ATR FTIR spectroscopy the second part of the theoretical introduction in **section 2.2** deals with the basic principles of the ATR spectroscopy in the mid infrared region.

2.2 Principles of ATR FTIR Spectroscopy

In **section 2.2** the principles of attenuated total reflection (ATR) Fourier transform infrared (FTIR) spectroscopy are given. First a short introduction to mid infrared spectroscopy is presented in **section 2.2.1**. Then the possibility of quantification through application of BEER'S law is shown in **section 2.2.2**. The last **section 2.2.3** deals with the fundamental principals of ATR spectroscopy as well as approximations for quantification when using multi reflection elements.

2.2.1 A Short Introduction to Mid Infrared Spectroscopy

In spectroscopy, interaction of electromagnetic radiation with matter is used to obtain qualitative and quantitative information about the matter. In **Figure 8** the electromagnetic spectrum is shown. It ranges from long radio waves with low energy (wavelengths of $\lambda = 10^8$ m) to short gamma rays with high energy ($\lambda = 10^{-16}$ m). Energy E and frequency ν of an electromagnetic wave can be related using the Planck constant h with: $E = h \nu$.

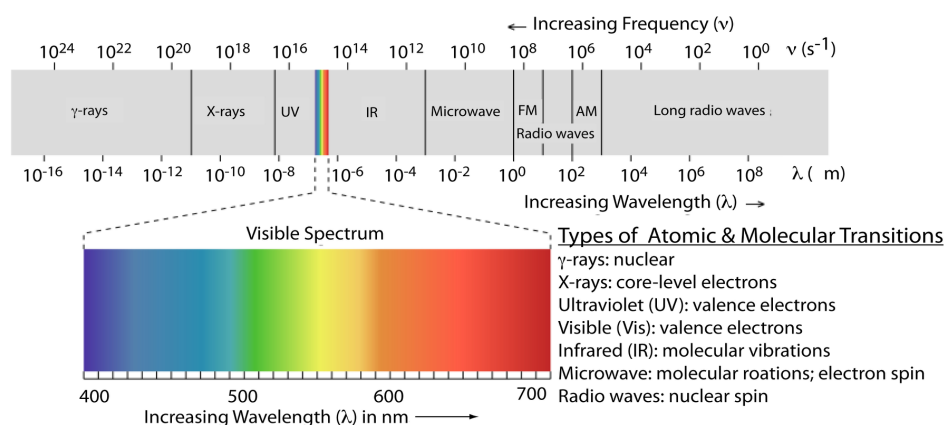


Figure 8: Scheme of the electromagnetic spectrum. Showing the different radiation types depending on the frequency and the wavelength. Types of atomic and molecular transitions resulting from interaction with radiation. Figure adapted from [27].

Depending on the frequency of radiation different atomic and molecular transitions can be excited: (i) γ -rays excite nuclear transitions, (ii) X-rays excite core-level electrons, (iii) ultraviolet (UV) and visible light excites valence electrons, (iv) molecular vibrations absorb infrared (IR) radiation, (v) microwaves stimulates molecular rotations and electron spins and (vi) radio waves lead to transitions of the nuclear spin. The infrared region ranges from frequencies of 3×10^2 to 3.7×10^5 GHz, where excitation of molecular vibrations occurs. IR spectra are typically given in wavenumbers (cm^{-1}). Relation between the wavenumber $\tilde{\nu}$, the speed of light c , the frequency ν and the wavelength λ is given in **Equation (1)**.

$$\tilde{\nu} = \frac{\nu}{c} = \frac{1}{\lambda} \quad (1)$$

The IR radiation is further divided into three regions: the far infrared region (FIR) ranging from $10 - 400 \text{ cm}^{-1}$ ($\lambda = 1000 - 25 \text{ }\mu\text{m}$), the mid infrared region (MIR) from $400 - 4000 \text{ cm}^{-1}$ ($\lambda = 25 - 2.5 \text{ }\mu\text{m}$) and the near infrared region (NIR) from $4000 - 12500 \text{ cm}^{-1}$ ($\lambda = 2.5 - 0.8 \text{ }\mu\text{m}$).

The mid-IR region provides access to group frequency vibrations of common functional groups, as well as and the specific finger print region of organic molecules. These vibrations in molecules are stimulated if the frequency of the radiation matches the vibrational frequency. If in addition during vibration the dipole moment of the bond is changing, the electromagnetic irradiation at these frequencies is absorbed. For diatomic molecules, the vibrational frequency can be described with **Equation (2)**.

$$\nu = \frac{1}{2\pi c} \sqrt{\frac{k_0}{\mu}} \quad (2)$$

with μ as the reduced mass of the two connected bodies *e.g.* two atoms, k_0 as force constant and the speed of light c . The stronger the molecular bond, hence the higher k_0 , the higher frequencies (higher energy) is absorbed. Vice versa the higher the molecular weight, vibrations are excited at lower energies (lower frequencies). The theoretical basis, describing those vibrations is the harmonic oscillator. To explain also transitions in the NIR range (overtones, combinations) the model needs to be refined to the anharmonic oscillator. In order to be IR active, the transition rule $\Delta\nu = \pm 1$ has to be fulfilled as well as the dipole moment has to change while vibration. Qualitative information about chemical compounds can be extracted from the frequency of the absorbed electromagnetic radiation. Therefore, IR spectroscopy is a versatile tool in chemical analysis since molecule specific information can be gained. But IR spectroscopy is not only a qualitative but also a quantitative analysis method. This will be shown in **section 2.2.2**.

2.2.2 Quantification through Beer's Law

In 1852 a fundamental correlation between absorption and the concentration of a substance was published by August Beer [28]. Here, the transmittance T at a certain wavenumber $\tilde{\nu}$ is dedicated as the ratio between the initial intensity of light (I_0) and the intensity of the radiation after sample interaction (I). Transmittance decreases exponentially with the concentration c , pathlength d and the linear absorption coefficient $\alpha(\tilde{\nu})$ (see in **Equation (3)**).

$$T(\nu) = \frac{I}{I_0} = e^{-\alpha(\tilde{\nu}) c d} \quad (3)$$

Absorption is further defined as the decadic logarithm of the reciprocal transmission [29]:

$$A(\nu) = \log \frac{I_0}{I} = \frac{1}{\ln 10} \alpha_i(\tilde{\nu}) c_i d = a_i(\tilde{\nu}) c_i d \quad (4)$$

As given in BEER'S Law (**Equation (4)**) absorption is depending on the concentration of the analyte c_i , the pathlength d and the decadic absorption coefficient $a_i(\tilde{\nu})$. Deviations from the linear correlation between absorbance and concentration of a certain measurement can be arising from different factors *e.g.* spectral resolution and scattering effects. Therefore, to determine the connection between concentration and absorption for a specific experiment a molar decadic absorption coefficient $\epsilon_i(\tilde{\nu})$ (dimension $\text{mol L}^{-1} \text{ cm}^{-1}$) is usually empirically evaluated.

In general, there are two basic setups which are mainly used for IR spectroscopy in chemical analysis: (i) a transmission setup, where the electromagnetic wave is going straight through a sample and (ii) an ATR setup where through total reflection at an interface of an IR transparent element, often called a crystal and sample, an evanescent wave arises which then interacts with adjacent components.

Within this thesis an ATR setup is used for the investigation of the interaction of proteins with mesoporous silica. Therefore, theoretical aspects of the ATR setup are illustrated in the following **section 2.2.3**

2.2.3 Basics of Attenuated Total Reflection FTIR Spectroscopy

If considering two IR transparent media with two different refractive indices $n_1 > n_2$ and an electromagnetic wave going from the optical denser medium (n_1) to the optical rarer medium (n_2) different phenomena occur.

Going from one to another medium the speed of the electromagnetic wave is changed. The relation between the speed of light in vacuum c_0 and the speed of light in a certain medium c_M is given by the refractive index (see **Equation (5)**).

$$n = \frac{c_0}{c_M} \quad (5)$$

Depending on the angle of the incident beam, light is reflected and/or transmitted (see **Figure 9 (A)**). The connection between the angle of incidence θ_I and the angle of the transmitted

wave θ_2 in dependence of the refractive indices of the two weakly absorbing media, gives SNELL'S law in **Equation (6)**.

$$n_1 \sin(\theta_1) = n_2 \sin(\theta_3) \quad (6)$$

Note that, the angle of the reflected wave θ_2 is equal to the angle of the incident beam θ_1 as it is schematically visualized in **Figure 9 (A)**.

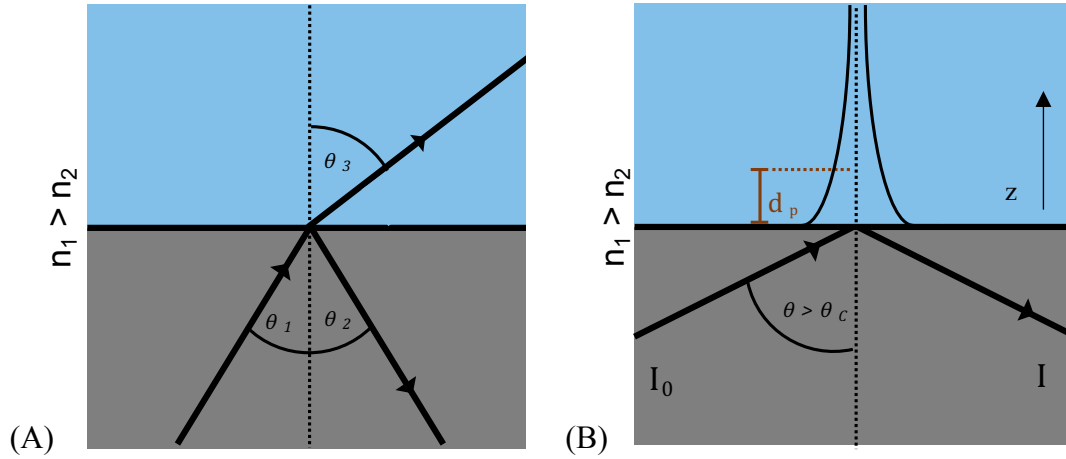


Figure 9: Schematic visualization of an electromagnetic wave going from an optical denser medium to an optical rarer one ($n_1 > n_2$). (A) For an electromagnetic wave with an incident angle θ_1 below the critical angle θ_c , reflection and transmission occur. (B) For an electromagnetic wave with an incident angle above the critical angle $\theta > \theta_c$ total reflection occurs. An evanescent wave with a depth of penetration d_p propagates into the optical rarer medium.

The largest angle of θ_1 for which SNELL'S law is still true is the critical angle θ_c . (**Equation (7)**).

$$\theta_c = \arcsin\left(\frac{n_2}{n_1}\right) \quad (7)$$

Angles larger than the critical angle lead to total reflection of the incident beam. An evanescent electric field is generated upon total reflection and propagates into the optically rarer medium (see in **Figure 9 (B)**) [30]. A common parameter for describing the evanescent wave is the penetration depth d_p . It is defined as the length in direction z where the electrical field falls to $1/e$ of the electrical field at the interface (see **Equation (8)**):

$$d_p = \frac{\lambda_0}{2\pi \sqrt{n_1^2 \sin^2(\theta_1) - n_2^2}} \quad (8)$$

The attenuation of the intensity of the evanescent wave can be used for spectroscopic analysis similar to the attenuation of intensity of the primary beam in transmission experiments.

In order to transfer BEER'S Law (**section 2.2.2, Equation (4)**) from a transmission experiment to an ATR internal reflection setup (IRS), the effective thickness d_e is specified as: 'The thickness d_e is defined as the thickness of a film of the sample material that would give the same absorbance for transmission at normal incidence as that obtained in the IRS experiment' [31]. It was shown that the effective thickness can be approximated for weakly absorbing materials by [30]:

$$d_{e\perp} = \frac{\lambda_0}{n_1} \frac{n_{21} \cos(\theta)}{\pi (1 - n_{21}^2) [\sin^2(\theta) - n_{21}^2]^{1/2}} \quad (9)$$

$$d_{e\parallel} = \frac{\lambda_0}{n_1} \frac{n_{21} \cos(\theta) [2 \sin^2(\theta) - n_{21}^2]}{\pi (1 - n_{21}^2) [(1 + n_{21}^2) \sin^2(\theta) - n_{21}^2] [\sin^2(\theta) - n_{21}^2]^{1/2}} \quad (10)$$

$$d_e = \frac{d_{e,\perp} + d_{e,\parallel}}{2} \quad (11)$$

with parallel \parallel and perpendicular \perp part of the wave and $n_{ij} = n_i/n_j$.

Throughout these approximations, BEER'S Law can be applied to ATR IR experiments. Hence, similar to transmission experiments the concentration of an analyte at a certain wavelength can be calculated (see **Equation (12)**).

If multi-reflection ATR elements are used, the light is reflected several times. With the number of reflections N , absorption increases linearly. The resulting equation for quantification in multi reflection ATR experiments is:

$$A(\nu) \approx \epsilon_{\text{analyte}}(\tilde{\nu}) c_{\text{analyte}} d_e N \quad (12)$$

Throughout these approximations for d_e and a higher number of reflections N the theoretical calculated path length (' $d_e N$ ') is in the scale of typical transmission experiments. For example, a silicon multi reflection element with $n_1 = 3.42$, $n_2 = 1.33$ (*refractive index of water*) at an angle of incidence $\theta = 45^\circ$ ($\theta_c = 26^\circ$ for silicon [29]) results in an effective thickness $d_e = 0.317 \mu\text{m}$ at a wavenumber of 1550 cm^{-1} for one reflection. With a length of 2 cm for the home made multi reflection element used in this thesis (see **section 5.1**), the number of reflections is $N = 20$ and the resulting calculated effective is $d = 20 \cdot 0.317 \mu\text{m} = 6.34 \mu\text{m}$.

Having shown the theoretical basic of ATR spectroscopy, the characteristic bands of proteins in the mid-IR as well as their origin and their possible use for secondary structure determination are presented in **section 2.3**.

2.3 Infrared Spectroscopy of Proteins

Proteins exhibit a complex structure, which is essential for their proper function. The 3-dimensional arrangement is determined through: (i) the primary structure, defined through the sequence of amino acids, (ii) the secondary structure *e.g.* α -helix, β -sheets, formed through intramolecular hydrogen bonds, (iii) the tertiary structure, resulting from a further assembly of secondary structure and/or disulfide bridges forming a polypeptide chain and (iv) the quaternary structure, formed through assembly of subunits and possible co-factors *e.g.* Heme b in hemoglobin (**Figure 10**) [32].

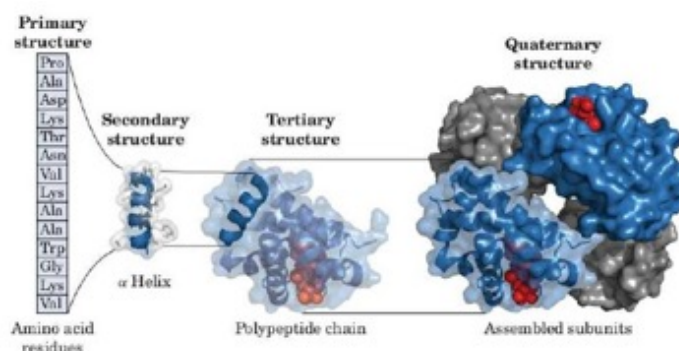


Figure 10: Scheme of the structures of the protein Hemoglobin. Showing assembly of primary structure (amino acid sequence), secondary structure (*e.g.* α -helix, β -sheets), polypeptide chains forming the tertiary structure and assembly to final protein (quaternary structure). Adapted from [32].

Determination of these structures is a key tool in protein analytics. In 1950 ELLIOT *et al.* published the first results of the infrared spectroscopic investigation of synthetic polypeptides [33]. Since then, infrared spectroscopy was more and more established as a valuable tool to investigate the secondary structure of proteins. Through the high information content and the time resolved recording of infrared spectra, the mechanisms of protein reactions, as well as protein folding, unfolding and misfolding can be investigated within the mid-IR region. Proteins show specific vibrational bands, which result from different structural features in the protein backbone *e.g.* amide moiety (Amide bands), as well as from side chain moieties. Those characteristic modes of proteins can be used for quantification but can also be used to determine the relative amounts of secondary structure within the protein. Thereby, the specific amid modes are presented in the following **section 2.3.1**.

2.3.1 Characteristic Vibrational Bands of Proteins

For protein investigation *via* spectroscopy the amide bands arising from IR absorption of the backbone of protein chains are the most informative, especially concerning the secondary structure. Nevertheless, every side chain moiety of the amino acids shows additional absorption bands [34]. Because of high abundance of amide bonds in the polypeptide protein backbone, the bands associated to these modes are more evident compared to other side chain moiety vibrations.

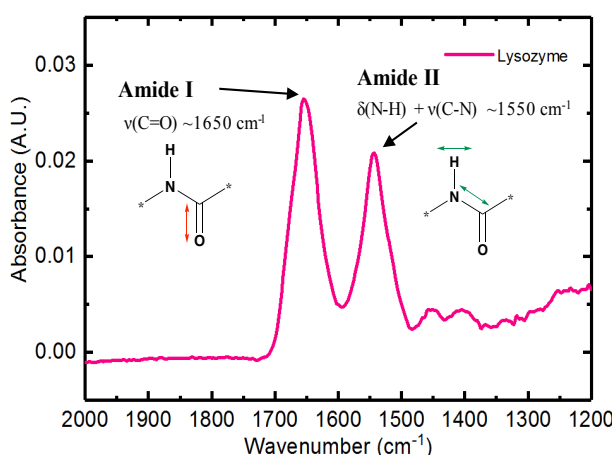


Figure 11: Typical protein absorption spectrum showing the most dominant amide I ($\nu(\text{C}=\text{O}) \sim 1650 \text{ cm}^{-1}$) and amide II ($\delta(\text{N-H}) + \nu(\text{C-N}) \sim 1550 \text{ cm}^{-1}$) bands arising from the amide moiety in the protein backbone. Spectrum of the protein Lysozyme within the mid-IR region from 2000-1200 cm^{-1} .

Figure 11 shows a typical protein spectrum in the region from 2000-1200 cm^{-1} , with the typical amide absorption bands: (i) amide I ($\nu(\text{C}=\text{O}) \sim 1650 \text{ cm}^{-1}$) and (ii) amide II ($\delta(\text{N-H}) + \nu(\text{C-N}) \sim 1550 \text{ cm}^{-1}$). In general, there are additional amide bands as *e.g.* amide III and amide A and B, which are weaker in their absorption.

In the following sections the single absorption bands of proteins in the mid infrared region are discussed in more detail.

2.3.1.1 Amide I Band (1610 - 1695 cm^{-1})

For proteins, the most dominant and best-characterized absorption band in the mid-IR region is the amide I band. It arises mainly from the C=O stretching vibration, with minor contributions from N-H in-plane bending and the out-of-phase C-N stretching vibration in the region 1600-1700 cm^{-1} [35]. Side chain moieties hardly affect the band, whereas the secondary structure, hence intramolecular hydrogen bonds of the protein backbone is strongly contributing to the shape of the amide I band. Therefore, absorption around 1650 cm^{-1} can be used for secondary structure analysis. The shape of the amide I band arises from overlapping

2.3.1 Characteristic Vibrational Bands of Proteins

contributions from single secondary structure vibrations as from α -helix ($\sim 1654\text{ cm}^{-1}$), β -sheet ($\sim 1633\text{ cm}^{-1}$, $\sim 1684\text{ cm}^{-1}$), turns ($\sim 1672\text{ cm}^{-1}$) and disordered structures ($\sim 1654\text{ cm}^{-1}$) [34].

2.3.1.2 The Amide II Band ($\sim 1550\text{ cm}^{-1}$)

The amide II band around 1550 cm^{-1} is a combination of the N-H in plane bend and the C-N stretching vibration of the protein backbone. It is less frequently used for secondary structure analysis, although it provides valuable structural information. Due to possible overlapping of the water absorption mode at $\sim 1640\text{ cm}^{-1}$ with the amide I band, the amide II mode is preferentially used for quantification of protein content in aqueous solutions.

2.3.1.3 The Amide III Band ($1400\text{-}1200\text{ cm}^{-1}$)

The amide III band between $1400\text{-}1200\text{ cm}^{-1}$ arises from C-N stretching and N-H bending. In polypeptides contributions from side chain structures are present [34]. This band is less well defined compared to amide I and amide II [35].

2.3.1.4 The Amide A Band ($\sim 3300\text{ cm}^{-1}$) and the Amide B Band ($\sim 3070\text{ cm}^{-1}$)

The amide A band rises from N-H stretching vibration in the region $\sim 3300\text{ cm}^{-1}$ [34] [35] and its frequency is dependent on hydrogen bonding. The amide B band is related to amide A with weak absorption at $\sim 3070\text{ cm}^{-1}$. For investigation of protein in aqueous solutions amide A is superimposed by the broad -OH vibrational mode ($\nu_{\text{as}} \sim 3400\text{ cm}^{-1}$) of water.

Since aqueous conditions are the natural surrounding of proteins, investigation of the native conformation is preferentially performed in aqueous buffer solutions. The high water content in the protein samples is a major drawback for protein investigation *via* IR spectroscopy, which will be further discussed in **section 2.3.2**.

2.3.2 Experimental Aspects of Protein FTIR Spectroscopy in Aqueous Solutions

Strong absorption of the H_2O bending vibration near 1640 cm^{-1} is a problem for the investigation of proteins in aqueous solutions. For example, if a transmission cell with a pathlength $> 25\text{ }\mu\text{m}$ is filled with aqueous solutions, light at 1640 cm^{-1} is completely absorbed by water. Hence, detection of other components at this frequency is not possible. As a consequence, very short path lengths between $6\text{-}8\text{ }\mu\text{m}$ are used for transmission measurements of proteins in the mid-IR region [35]. According to BEER's Law, absorption is dependent on the concentration c , the sample thickness d as well as the decadic molar absorption coefficient $a_i(\tilde{\nu})$ (see **Equation (4)**). As a consequence, if short path lengths are used, high protein

concentrations of ca. 10 mg/mL are required to be able to investigate the analyte. Nevertheless, investigating proteins at low concentrations using IR spectroscopy is of great interest. Recently, SCHWAIGHOFER *et al.* reported the use of an external cavity-quantum cascade laser in order to increase the intensity of the used radiation and this allowing to increase the optical path. With this setup it is possible to investigate proteins in low concentrations as *e.g.* 0.25 mg/mL in transmission [36].

In this context, possible preconcentration steps of protein in a mesoporous layer could reveal low concentration detection limits beyond 0.5 mg/mL, which was investigated within this thesis (see **section 3.3.6**).

In the following **section 3** the overall work performed within this thesis is presented. In the first **section 3.1**, considerations concerning the possibility to determine protein location inside the pore using coated ATR crystals in combination with FTIR spectroscopy are discussed. Within **section 3.2** the synthesis of the mesoporous silica films on top of the ATR crystals as well as their optimization towards large pore sizes is given. In the last section, adsorption experiments using these mesoporous silica film coated ATR crystals as well as uncoated ATR crystals are presented (**section 3.3**).

3. Considerations, Results and Discussion

Within this chapter the work performed in this thesis is presented. Prior to the practical work, considerations concerning the realization of our approach to determine protein location inside the pore were performed. Here the central question is, if it is possible to the proof the entrance of the proteins into the pores using definite calculations based on principles of ATR spectroscopy. These considerations are presented in the first **part 3.1**.

Concerning the practical work performed within this thesis, the primary task was the optimization of the synthesis of mesoporous silica films towards large pore sizes of >10 nm. The road towards the right conditions for the synthesis of stable and highly homogeneous mesoporous silica films is presented in **chapter 3.2**. For subsequent investigation of the interaction of proteins mesoporous silica coated ATR crystals were used. The results of the investigation of the interaction of proteins (Lysozyme and Lipase from *Candida rugosa*) with different silica surfaces (porous and non-porous, silica and methylated silica) by ATR FTIR spectroscopy are presented in **section 3.3**.

3.1 Considerations

Before any practical work for a project, considerations about the realization are necessary. My goal was to determine whether a protein is located inside the pore of a mesoporous silica structure or solemnly adsorbed on the outer surface. Therefore, extended theoretical thoughts concerning ATR spectroscopy in combination with the mesoporous film were performed. Different possibilities determining the proteins' location inside the film are presented in **section 3.1.1**. For adsorption of a component on a surface, attraction between the component and the surface has to be given. Therefore, considerations concerning surface properties of the silica particles and proteins are discussed in **section 3.1.2**. Within this section some parameters, which are important for adsorption of proteins into the pores are shortly summarized. In the last **section 3.1.3** characteristics of used proteins Lysozyme and Lipase are presented.

3.1.1 Considerations of the Determination of the Protein Inside the Pore

As already stated, my aim is to determine the entrance of a protein into a pore *via* ATR FTIR spectroscopy. Therefore, considerations and calculations were performed. The principle approach is to calculate an absorbance that would be expected if the protein is only adsorbed on the top of the layer and performing an adsorption experiments using a mesoporous film. Through the comparison of the two intensities of the resulting adsorption bands, statements concerning the protein location can be made.

For the first two methods, the variable depth of penetration d_p of the evanescent field is considered. Beside others, d_p is influenced by: (i) the angle of incidence (dependency discussed in **section 3.1.1.1**) or (ii) the wavelength of the used irradiation (see **section 3.1.1.2**). Another method is presented in **section 3.1.1.3**. Here the fraction s of the evanescent field's intensity within the film is used for calculations. Those considerations are transferred from a model established by BAUMGARTNER *et al.* [15].

3.1.1.1 Alternating the Depth of Penetration by Variation of the Angle of Incidence

The angle of the polished facets of an ATR crystal influences the angle of incidence θ_i of the incoming electromagnetic wave, which can be further related to the depth of penetration $d_{p,i}$ of the evanescent field (see **Equation (13)**):

$$d_{p,i} = \frac{\lambda}{2\pi \sqrt{n_1^2 \sin^2(\theta_i) - n_2^2}} \quad (13)$$

Equivalently, the intensity $I(z)$ of the evanescent field at a certain point z changes if the depth of penetration is altered:

$$I(z) = I_0 e^{-\frac{2z}{d_{p,i}}} \quad (14)$$

The overall intensity of the evanescent field from the ATR crystal surface to a certain height z can be calculated (**Equation (14)**). Using the integrals of the intensity of different angles of incidence θ_1 and θ_2 of the incoming beam and at a defined frequency, a ratio f of the two different intensities be formed (see **Equation (15)**). This ratio f is only dependent on the depth of penetration (hence, the angle of incidence θ_1 and θ_2), and the position z (distance of the field from the ATR surface).

$$f = \frac{\int_0^z I_0 e^{-\frac{2z}{d_{p,1}(\theta_1)}} dz}{\int_0^z I_0 e^{-\frac{2z}{d_{p,2}(\theta_2)}} dz} = \frac{I_0 \left(-\frac{2}{d_{p,1}(\theta_1)} \right) e^{-\frac{2z}{d_{p,1}(\theta_1)}} \Big|_0^z}{I_0 \left(-\frac{2}{d_{p,2}(\theta_2)} \right) e^{-\frac{2z}{d_{p,2}(\theta_2)}} \Big|_0^z} = \frac{\left(-\frac{2}{d_{p,1}(\theta_1)} \right) \left(1 - e^{-\frac{2z}{d_{p,1}(\theta_1)}} \right)}{\left(-\frac{2}{d_{p,2}(\theta_2)} \right) \left(1 - e^{-\frac{2z}{d_{p,2}(\theta_2)}} \right)} \quad (15)$$

Considering a mesoporous silica coated ATR crystal, with a film thickness th the following thoughts can be formulated: Assuming the analyte is not penetrating the pores, the signal results only from species which are exactly located on top of the layer ($z = th$). Therefore, a certain ratio f_{th} can be calculated using two different angles of incidence. Throughout two different measurements at those different angles of incidence a ratio of intensities f_{sample} can be determined. Through comparison of the two ratios a statement about the height z hence, the location of the protein can be performed. In the case the analyte is inside the pore: $z < th$, further with $dp_1 > dp_2$ it can be stated if that ratio f_{sample} is smaller than f_{th} . the analyte is inside the pore. If the measured ratio and the calculated one are almost the same, we can state that the analyte must be at position $z = th$, hence it is located on top of the film.

The trend of d_p at wavenumber 1550 cm^{-1} (the position of the amide II mode of proteins) of a silicon and a germanium ATR crystal as a function of the angle of incidence θ (theta) is shown in **Figure 12**. For calculations the refractive indices of silicon ($n_{1,Si} = 3.42$), germanium ($n_{1,Ge} = 4$) as well as for silica ($n_{SiO_2} = 1.26 - 1.37$ ($n_2 = 1.3$)) were used according to **Equation (13)**.

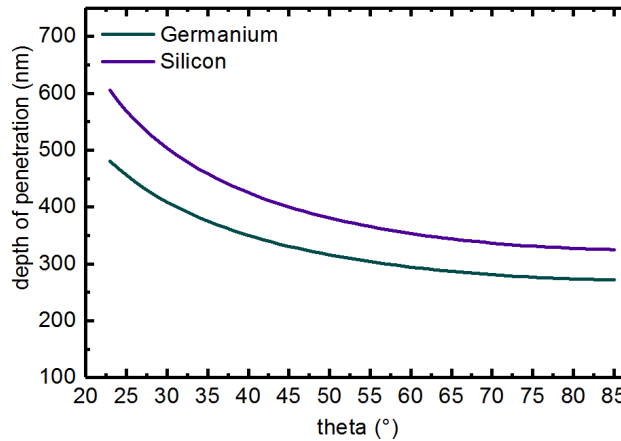


Figure 12: Graph of the depth of penetration (nm) of the evanescent wave at wavenumber 1550 cm^{-1} in dependency of the angle of incidence θ , for silicon and germanium ATR crystals with $n_{1,silicon} = 3.42$, $n_{1,germanium} = 4$ and a silica coating with $n_2 = 1.3$ on top.

As visible in **Figure 12** the change of d_p within a practically realizable region around $40^\circ - 60^\circ$ is quite low. The highest difference in d_p could be reached by taking a germanium crystal

at 60° with $d_p = 294$ nm and a silicon crystal at 40° with $d_p = 425$ nm at wavenumber 1550 cm^{-1} .

Nevertheless, changing the angle of incidence means to change either the mirrors in the setup, or to use two different ATR crystals with *e.g.* 40° and 60° in angle (polished facets). Hence, at least two different measurements have to be performed. Here, providing two times same conditions, as equal thickness of the coated silica layer as well as all other parameters is challenging. Therefore, other, simpler approaches were considered.

Another factor influencing the depth of penetration is the wavelength, which is used for considerations presented in the following **section 3.1.1.2**.

3.1.1.2 Wavelength Dependency of the Depth of Penetration

If an analyte shows absorption at two different wavelengths, a ratio between the two obtained intensities can be formed. Thereby, a ratio of intensities at $z = 0$ can be obtained using an uncoated ATR crystal for a measurement. Knowing the initial ratio at position $z = 0$ the theoretical ratio at $z = th$ can be calculated using an equation similar to **Equation (15)**, while for calculation of d_p using **Equation (13)** the different wavelengths are inserted. If now a measurement using a coating is performed, the so obtained ratio can be compared with the theoretical calculated one. Hence, the basic thought as well as the calculations is similar as performed in **section 3.1.1.1**. But here, one measurement using an uncoated crystal and a measurement using a crystal, which is coated could give enough information for performing the required calculations.

A plot of their interdependence for an angle of incidence of 45° is visualized in **Figure 13**.

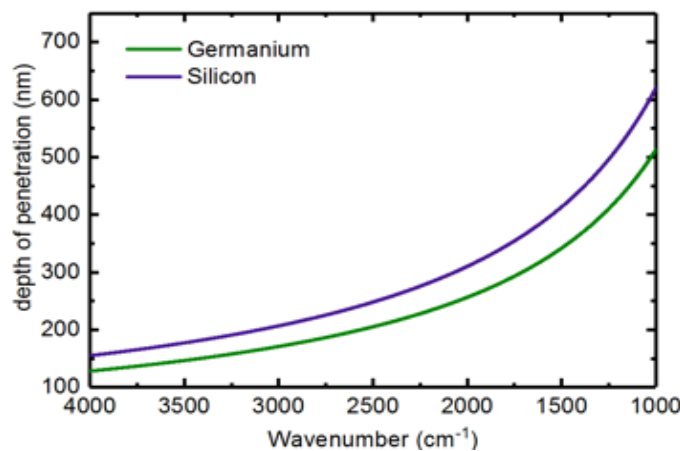


Figure 13: Graph of the depth of penetration in nm of the evanescent wave at an angles of incidence θ of 45° in dependency of the wavenumbers in mid IR region for silicon and germanium ATR crystal with $n_{1,\text{silicon}} = 3.42$, $n_{1,\text{silicon}} = 4$ and a silica coating with $n_2 = 1.3$ (refractive index of silica $n = 1.26\text{--}1.37$). Calculated with equation (14)

As visible in **Figure 13**, the change of d_p within the mid-IR region for wavenumbers from $4000\text{ cm}^{-1} - 1000\text{ cm}^{-1}$ ranges for silicon from $d_p = 155\text{ nm}$ at 4000 cm^{-1} to $d_p = 620\text{ nm}$ at 1000 cm^{-1} and for germanium from $d_p = 128\text{ nm}$ at 4000 cm^{-1} to $d_p = 513\text{ nm}$ at 1000 cm^{-1} . As discussed in **section 2.3**, proteins exhibit vibrational bands in the upper frequency region, namely the amide A ($\nu(\text{N-H}) \sim 3300\text{ cm}^{-1}$) modes, as well as in the lower frequency region *e.g.* the amide II ($\delta(\text{N-H}) + \nu(\text{C-N}) \sim 1550\text{ cm}^{-1}$) mode. Theoretically, it would be possible to use those two modes for calculations. Nevertheless practically, the amide A band is very low in its intensity as well as its accessibility because of the broad water mode in the region $3450 - 3300\text{ cm}^{-1}$ is poor.

A general drawback of this calculation method is that the analyte has to exhibit two absorption bands at two wavenumbers sufficiently apart. Therefore, a third, more generally method was based on the model of BAUMGARTNER *et al.* [15] which will be presented in the next section 3.1.1.3.

3.1.1.3 Calculation of the Fraction of the Evanescent Field within the Mesoporous Film

Due to its exponential nature, the evanescent field extends beyond the coating of an ATR crystal, even if the depth of penetration d_p is within the film thickness th , as schematically visualized in **Figure 14**.

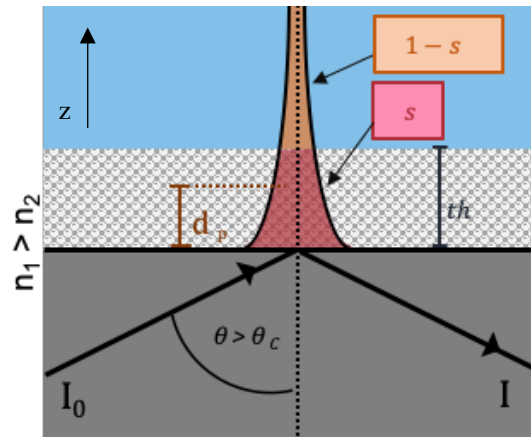


Figure 14: Scheme of the evanescent wave with a coated ATR crystal (film thickness th). Fraction s is visualized in red, fraction of the evanescent wave above the layer ($1-s$) in orange.

The fraction s is the evanescent field's intensity in the film and can be calculated with **Equation (16)** [15].

$$s = \frac{\int_0^{th} I_0 e^{-\frac{2z}{d_p}} dz}{\int_0^{\infty} I_0 e^{-\frac{2z}{d_p}} dz} = 1 - e^{-\frac{2th}{d_p}} \quad (16)$$

The remaining intensity outside the layer can be calculated with $1-s$.

Theoretically the absorbance of the analyte at height th ($A_{z=th}$) can be calculated with measured absorbance on a non-coated ATR crystal $A_{z=0}$ and subsequent multiplication with $1-s$ (see **Figure 15**).

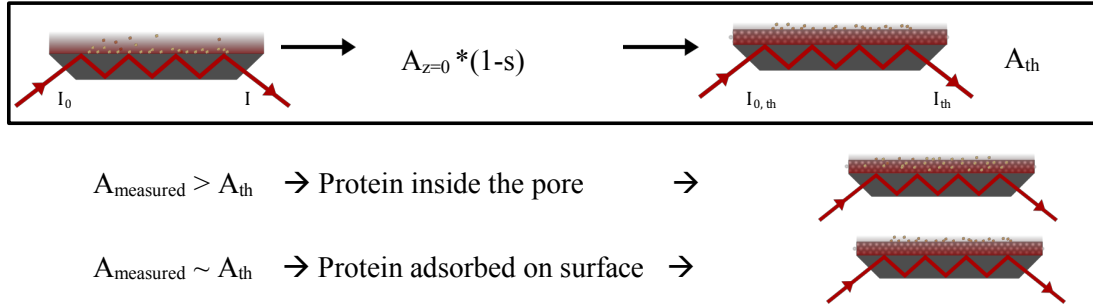


Figure 15: Visualization of the determination of the location of the protein inside the pore or on the surface.

If now the theoretically calculated absorbance (A_{th}) is compared with the measured absorbance using a coated ATR crystal ($A_{measured}$) one can state: If the measured absorbance is larger than the calculated one ($A_{measured} > A_{th}$) the protein must be inside the pore. If the absorbance is almost the same ($A_{measured} \sim A_{th}$) the protein is adsorbed on the surface (see **Figure 15**). For a faster evaluation a ratio of the two intensities can be formed (**Equation (17)**):

$$ratio = \frac{A_{measured}}{A_{z=0} (1-s)} \quad (17)$$

If the ratio is definitely larger than 1, the absorbance of the sample is greater than it would be at position $z = th$. Hence, it can be stated, that the analyte has penetrated the film. Whereas, if the ratio is around 1 the analyte is located on the surface of the film.

This third consideration of calculation a fraction s and performing a measurement with and without a coating was chosen to be the best for evaluation of the location of the protein. Hence it was shown that it is possible to determine the entrance of an analyte (protein) into the pore, given that a stable mesoporous film with a defined thickness is provided.

For adsorption of a molecule on a surface, properties as *e.g.* charge, hydrophilicity/hydrophobicity of both interaction partners are important. Additionally, for adsorption into pores, the pore size and the size of the molecule must be considered. In **section 3.1.2**, surface properties of silica *e.g.* point of zero charge, and the properties and size of the potential proteins are discussed.

3.1.2 Considerations Concerning the Interaction of Proteins with Mesoporous Silica Surfaces

Considerations concerning surface properties of silica in aqueous media and corresponding properties of proteins were performed and are presented within this section. Three parameters are roughly considered to be relevant for adsorption of the protein into the pore:

Electrostatic Interactions: It is reported that electrostatic interactions have a major influence for the interaction of silica and proteins [30,31]. Hence, parameters, which determine the electrostatic properties, as the point of zero charge (PZC) of the support (silica), the isoelectric point (pI) of the protein and the pH of the solution, have impact on the protein-silica interaction. PCZ of mesoporous silica is reported to be around 3.6 [14]. Hence, at solution $\text{pH} < 3.6$ the surface is positively and at $\text{pH} > 3.6$ the silica surface is negatively charged. Similarly, a protein is positively charged if $\text{pH} < \text{pI}$ and negatively charged at $\text{pH} > \text{pI}$. To enhance electrostatic attraction, the surface and the analyte have to carry opposite charge. Thereby, a protein with high pI, *e.g.* Lysozyme with $\text{pI} = 11.3$ [5] in a solution with pH 7 should show high adsorption to silica, since protein and surface are of opposite charge.

Polarity: The unmodified silica surface exhibit unreacted OH moieties and is therefore from polar character. If the surface is functionalized with methyl groups, hence, if the -OH moieties are replaced by methyl groups, the silica surface becomes more hydrophobic. If so, hydrophobic interactions are contributing to adsorption of proteins onto methylated silica surfaces rather than ionic ones [38]. For proteins, the surface properties *e.g.* polarity are predominantly determined by the primary structure, hence by side chain moieties. In addition to primary structure, different posttranslational modifications (PTM) as *e.g.* glycosylation, acetylation, phosphorylation can further alter the surface properties of the protein.

Pore Size: Besides surface properties, the size of the protein has to match with the size of the pores of the mesoporous silica. Thereby, small globular proteins are preferred for our approach, in order to fit the protein inside pores with size ~ 10 nm.

Hence, adsorption of proteins into mesopores is depending on different factors and must be individually investigated for the specific protein. After some research about immobilization of proteins onto mesoporous supports the two proteins Lysozyme (LYS) and Lipase from *Candida rugosa* (LCR) were chosen for performing adsorption experiments. The properties of the single proteins are given in the following **section 3.1.3**.

3.1.3 Characteristics of the Used Proteins

In the following properties and common applications of the investigated proteins are highlighted. Lysozyme from chicken egg-white and a Lipase from the yeast *Candida rugosa* were used for investigation of their adsorption on different silica surfaces.

3.1.3.1 Lysozyme

The protein Lysozyme (LYS) is a small polypeptide of 129 amino acids. It hydrolyzes $\beta(1\rightarrow4)$ linkages between N-acetyl muramic acid and N-acetyl-D-glucosamine residues in peptidoglycan, which is the major component of bacterial cell walls. Hence, the protein is used for cell lysis of particularly gram-positive, but also gram-negative bacteria and is therefore an antibacterial agent. Lysozyme from hen egg-white has a molecular mass about 14.3 kDa, which contributes to an approximate size of 1.5 x 2.5 x 4.3 nm [5]. Furthermore, the protein has an isoelectric point (pI) of 11.3[5].

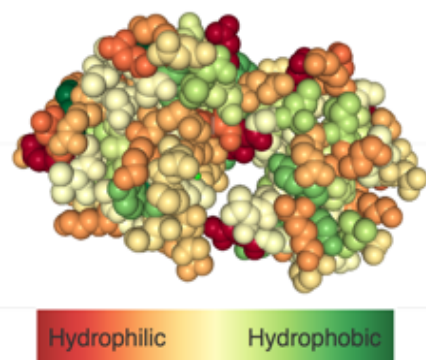


Figure 16: Structure of hen egg-white Lysozyme 253L in PDB (protein database). Surface color shows hydrophobicity (green), hydrophilicity (red). Picture adapted from PDB.

In **Figure 16**, the structure of Lysozyme from the online protein database (Nr. 235L in PDB) is given. The color represents surface hydrophobicity (green) or hydrophilicity (red). It can be concluded that for LYS the amino acid side chains on the surface are more of hydrophilic than of hydrophobic character.

Within the research for suitable proteins for performing adsorption experiments I considered it likely that Lysozyme is adsorbed inside the pores of mesoporous silica. This is because of the small size and a high pI. Furthermore, adsorption of the protein onto the mesoporous particles (MCM-41) was reported ([11], [39]). As mentioned **section 3.1.2** for Lysozyme adsorption on silica at buffer solution pH 7 is favored through electrostatic attraction, whereas by lowering the pH the repulsing electrostatic interaction should lead to desorption of the protein from the surface. The experimental results of these considerations are presented in **section 3.3**.

3.1.3.2 Lipases from *Candida rugosa*

Lipase from *Candida rugosa* (LCR), is a single polypeptide built from 534 amino acids, which has a molecular weight of ~ 60 kDa, a molecular volume of $5\text{ nm} \times 4.2\text{ nm} \times 3.3\text{ nm}$ [40], and a pI of 4.4 [41]. In **Figure 17** the surface structure of LCR is given with colors representing surface hydrophilicity (red) or hydrophobicity (green).

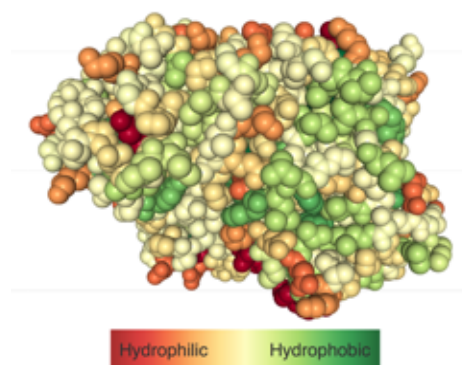


Figure 17: Structure of Lipase from *Candida rugosa* 1TRH in PDB (protein database). Surface color shows hydrophobicity (green), hydrophilicity (red). Picture adapted from PDB.

Lipases are triacylglycerol ester hydrolases (EC 3.1.1.3) and therefore catalyze primarily the hydrolysis of acylglycerols to glycerol and three fatty acids [40]. In general lipases are interfacial enzymes, since they have adapted to act on interfaces of two-phase systems *e.g.* oil in water. For catalytic activity no co-factor is needed, but lipases require interfaces for free access of their active site. This phenomenon is commonly referred to as “interfacial activation” [41]. However, lipases are seen as one of the most important enzymes for bio catalysis as they are implemented in various different sectors as [42]: (i) food industry, (ii) organic synthesis, (iii) pulp and paper industry, (iv) biodiesel production or (v) in biosensors. Hence, immobilization of Lipases onto mesoporous silica is interesting concerning their use for biocatalysis [43]. Enhanced properties of the immobilized enzymes have been reported and it was traced back to the protective environment if the protein is located inside the pore [5].

With the considerations made in **section 3.1.1**, we could show that with my setup it is possible to determine if the protein is really located inside the pore or solemnly adsorbed on the silica surface. Furthermore, for protein adsorption into the pores, the pore size of the mesoporous silica has to be larger than the size of the protein itself. Therefore, my goal was to synthesize mesoporous silica thin films with large pore sizes, greater than 10 nm. Here, a sol-gel process using Pluronic F127 as surfactant, for the EISA templating process, was optimized.

The results of the practical work performed towards the formation of those enlarged pore sizes are summarized in the following **chapter 3.2**.

3.2 Formation of Mesoporous Silica Thin Films with Large Pore Sizes

Within this section the practical work for the formation of the mesoporous silica thin films is presented. Firstly, film formation using CTAB as template was reproduced from BAUMGARTNER *et al.* ([15] **section 3.2.1**). On the basis of the knowledge of the process using an ionic surfactant, and in combination with reported film formation using F127 ([24],[44]), pore sizes of ~15 nm and a film thickness of ~600 nm could be reached. The road towards finding these conditions is described in **section 3.2.2**, while exact synthesis conditions are described in detail in the experimental part (**section 5**). In addition, the stability of different functionalized films under aqueous conditions was tested. These results are important concerning the use of films for adsorption experiments of proteins in buffer solutions (**section 3.2.3**).

3.2.1 Proof of Concept: Film Synthesis Using CTAB as Template

The first synthesis of mesoporous silica films was performed using a surfactant templating route, which was recently reported from BAUMGARTNER *et al.* (2018 [15]), here the starting conditions were adapted from the literature ([45],[46]).

The silica network formation was performed *via* an acidic hydrolysis and condensation of tetraethoxysilane (TEOS) in ethanol. By the use of cetyltrimethylammonium bromide (CTAB) in combination with EISA, films with highly ordered ~3 nm pores were synthesized, by spin coating under controlled humidity. Template removal was performed by solvent extraction. By varying the concentration of CTAB in the starting solution, two different mesostructures were obtained. A 3D hexagonal structure, using a molar ratio of 1:0.12 for TEOS:CTAB and a cubic structure using a molar ratio of 1:0.16 for TEOS:CTAB. Other components as well as more detailed synthesis explanation is given in the experimental part in **section 5**.

For learning the practical procedure of mesoporous film synthesis, both the 3D hexagonal and cubic structured mesoporous films were synthesized. The outcome was checked using low-angle X-ray diffraction (see **Figure 18**).

Throughout the highly ordered pore structure within the film, diffraction is occurring. The position of the peak in the diffraction pattern can be compared with reported patterns in order to evaluate the pore size and mesostructure [18], [24].

3.2.1 Proof of Concept: Film Synthesis Using CTAB as Template

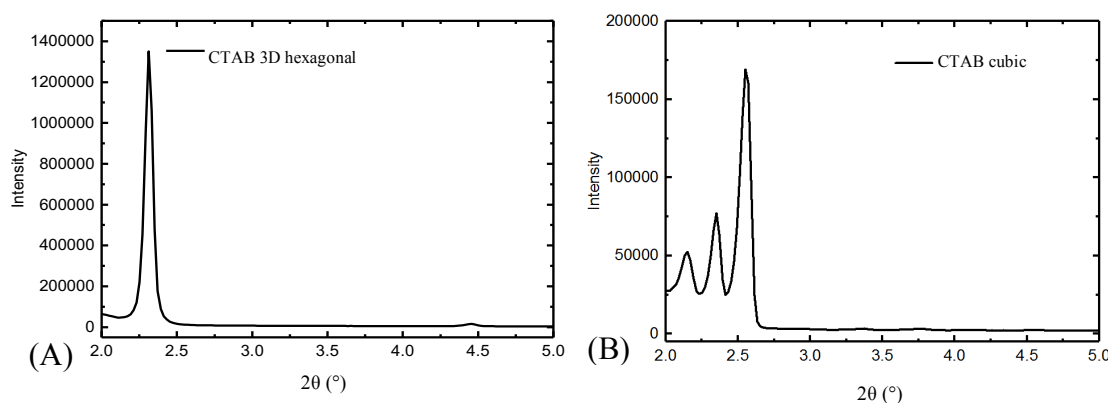


Figure 18: Low-angle X-ray diffraction patterns of: A) 3D hexagonal and (B) cubic mesoporous films obtained in Bragg-Brentano geometry ($\text{CuK}\alpha$ $\lambda = 1.54 \text{ \AA}$). Using a sol composition of: 1:13:5:5x10⁻³:0.12 (3D hexagonal) – 0.16 (cubic) for TEOS:EtOH:H₂O:HCl:CTAB. Spin coating at 50% RH – 65% RH, 2000 rpm, heat treatment at 110° over night, template removal: 6 h acetone reflux.

In **Figure 18** the X-ray diffraction patterns of the 3D hexagonal **(A)** and the 3D cubic **(B)** mesostructured films are visible. The diffractogram of the 3D hexagonal film shows an intense peak at 2.3° (2θ) and a peak of lower intensity at 4.49° (2θ). The diffractogram in **Figure 18 (B)** shows a characteristic diffraction pattern for the cubic structure with most intense peaks at 2.6°, 2.36° and 2.16° (2θ). Both patterns correspond well with literature [46].

Further characterization of the films concerning their thickness was investigated by measuring a scratch in the film with the profilometer. Using the ionic surfactant CTAB pore sizes of 2-4 nm and a thickness of ~500 nm were obtained. Given this results, I could proof the reproducibility of the results reported by BAUMGARTNER *et al.* (2018 [15]).

In order to obtain larger pore sizes, the knowledge concerning templating using CTAB was combined with reported synthesis of enlarged pore sizes using Pluronic F127 ([24], [44]). **Section 3.2.2** gives the starting point as well as steps towards the successful synthesis of mesoporous silica thin films with large pore sizes of ~ 15 nm and a film thickness of ~600 nm.

3.2.2 Synthesis of Thick Mesoporous Films with Large Pore Sizes Using Pluronic F127

As a reference point for synthesizing larger pores using F127, the protocol reported by Dunphy *et. al* ([24]) was reproduced. They reported pore sizes up to 15 nm by using Pluronic F127 as template for film synthesis *via* EISA. For the synthesis, the reactants were mixed in a one-pot reaction and reaction time for sol formation before spin coating was 10 min. In the reported study different concentrations of F127 in possible combination with another Pluronic (P104) were used for the formation of various pore sizes.

I reproduced the synthesis using 45.4 mg F127 per mmol SiO₂, which is a ratio of 1:0.0036 of TEOS:F127 in the starting solution. For first experiments relative humidity, from 20 – 80 % and spinning speed 2000-3000 rpm during spin coating were altered. After calcination at 350°C for 4 h samples were characterized by low-angle X-ray diffraction. The resulting X-ray diffractograms showed no distinct reflections, but rather broad and undefined reflections. Hence the reported highly ordered structure could not be obtained.

In addition, the resulting thickness of the obtained films was around 300 nm after calcination. For the later implementation of the mesoporous films as a coating of an ATR crystal a larger film thickness is desired. The larger the thickness of the film, the higher the fraction s of the evanescent wave inside the layer and therefore the lower the absorbance of substances which are not adsorbed inside the porous layer. For that reason, besides large pore sizes a high thickness of the film > 500 nm is favored.

Hence in order to increase film thickness and pore size, sol compositions concerning the amount of template, as well as the reaction time of the sol before spin coating were altered. However, X-ray diffraction patterns remained without reflections in the low-angle region, therefore we conclude no formation of ordered mesopores occurred. Therefore, the overall sol composition was modified as well as the deposition method was changed to dip coating. By the use of this deposition method higher film thicknesses are reported in literature [47]. The exact synthesis of mesoporous silica film performed by dip and spin coating are given in the experimental part in **section 5**.

3.2.2 Synthesis of Thick Mesoporous Films with Large Pore Sizes Using Pluronic F127

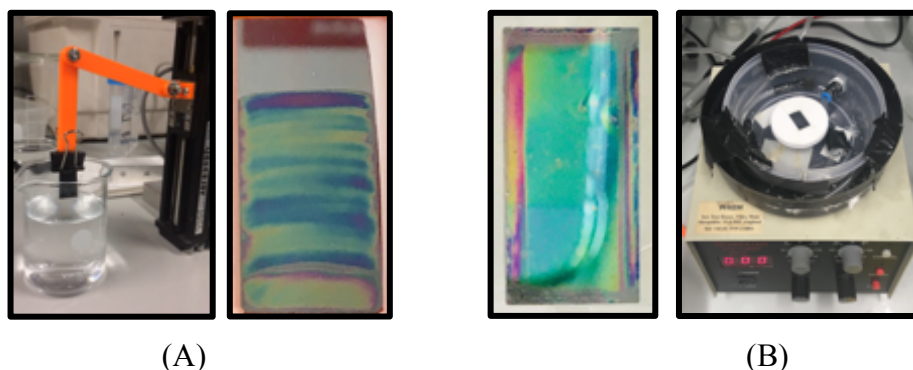


Figure 19: Pictures of films casted by dip coating (A) and spin coating (B) as well as pictures of the used home built dip coater and the used spin coater.

In **Figure 19** the two different casting setups (A) home-built dip coater and (B) a modified spin coater and pictures of films obtained from the corresponding methods are shown. It is visible that the film prepared by dip coating is more inhomogeneous in color as the spin coated one. The color depends on the film thickness. This results from optical phenomena (interference pattern), if the film thickness is in the range the wavelength of visible light (400 – 800 nm). Therefore, the inhomogeneous colors show the variation in film height.

For the coating on the ATR crystal a homogeneous coating is desired. Therefore, spin coating was used for preparation of the films for investigation using ATR FTIR spectroscopy. Further optimization of the sol composition lead to the final highly ordered large pore silica film with a thickness of about 600 nm.

The final sol composition was found with sample “SS63B” and is given in **Table 1**.

Table 1: Sol composition for Sample SS63B, obtaining 15 nm pore sizes and a film thickness of 625 nm.

SS63B	TEOS	F127	EtOH	H ₂ O	HCl (0.1 M)	Sol formation: 3 h RT Spin coating: 30% RH, 2000 rpm Aging: 4 – 12 h 80°C Calcination: 4 h 400°C
molar ratio	1	0.0096	0.016	16.28	0.0153	
[g]	1.3	0.75	4.6	0.884	0.947	

The optimized synthesis conditions were the following: (i) preparing a sol solution containing 2.5 g ethanol, 1.3 g TEOS, 0.675 g HCl (0.1 M) and a template solution of 0.75 g F127, 2.1 g EtOH, 0.884 g H₂O and 0.272 g HCl (0.1 M), ii) slowly stirring both solutions for 20 min at room temperature (RT), (i) merging solutions and stirring for another 3 h (for sol formation), (iii) spin coating at 30% relative humidity with a spinning speed of 2000 rpm, (iv) subsequent heat treatment at 80°C for 4-12 h and (v) final calcination at 400°C for 4 h.

The X-ray diffraction pattern of the thereby obtained mesoporous silica film is shown in **Figure 20**.

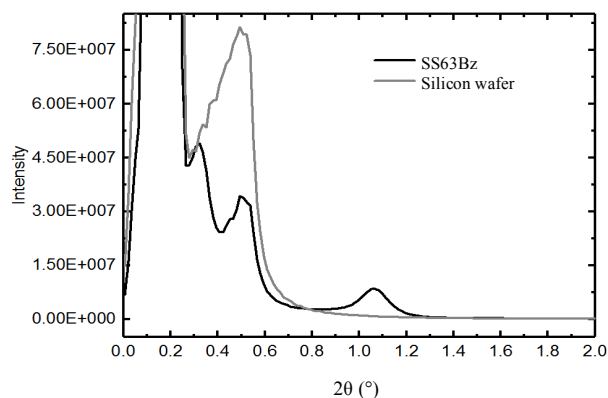


Figure 20: X-ray diffraction patterns of mesoporous silica film sample SS63Bz after calcination (black) and a blank silicon wafer used for coatings (grey) obtained in Bragg-Brentano geometry ($\text{CuK}\alpha \lambda = 1.54 \text{ \AA}$).

In **Figure 20** the X-ray diffraction pattern of an uncoated silicon wafer is given (grey line). Here a peak at 0.5° (2θ) arises from reflections of the primary beam at the silicon substrate and/or sample holder. Therefore, it must be excluded for analysis of all diffraction patterns of mesoporous silica films. The peaks at 0.3° (2θ) and 1.06° (2θ) arise from the mesoporous silica film. A definite determination of the pore size based on the diffraction pattern is performed through comparison with reported diffraction patterns in literature [24], [44]. For the film SS63B the pore size was further determined by ellipsometric porosimetry as well as a similar approach using our ATR setup (see **section 5.2.3**). Here throughout adsorption and desorption of water vapor in the porous structure a pore size of $\sim 12\text{--}15 \text{ nm}$ as well as size of interconnections ($\sim 7 \text{ nm}$) was found for the film SS63B.

Besides large pore sizes, the stability of the layer is essential for its implementation for later adsorption experiments from buffer solutions. Therefore, unfunctionalized, co-functionalized and post-synthesis functionalized films were immersed in buffer solution for 24 h. The results of this small but important study are presented in the following **section 3.2.3**.

3.2.3 Evaluation of the Stability of the Mesoporous Silica Films in Buffer

By introducing methyl groups into the silica network, the electron density at the silicon atom is increased. This is because electron density withdrawing inductive effect ($-I$ effect) of the oxygen atom is replaced by the electron density donating ($+I$) effect of the $-\text{CH}_3$ moiety.

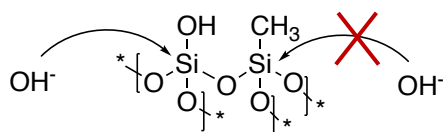


Figure 21: Scheme of the nucleophilic attack at the silicon atom. Methylated silicon atom does not allow for electrophilic attack of the hydroxyl ion

3.2.3 Evaluation of the Stability of the Mesoporous Silica Films in Buffer

As schematically visualized in **Figure 21**, the methylated silica network is less prone to a nucleophilic attack at the silicon atom performed by hydroxyl ions (OH^-) present in aqueous solution. Hence, throughout methylation of the film the stability under neutral and basic conditions can be enhanced.

For the evaluation of the stability of the mesoporous silica films the different samples were immersed in a 16.5 mM KH_2PO_4 buffer solution at pH 7 for 24 h. The film stability is evaluated through comparison of the X-ray diffraction pattern before and after incubation in buffer solution. Unfunctionalized as well as functionalized films synthesized by co-condensation as well as post synthetically grafting were investigated:

For functionalization *via* the co-condensation route, the original sol composition (**Table 1**) was varied concerning the TEOS:MTES (methyltriethoxysilane) molar ratio: (i) 0.85:0.15 (15% MTES), (ii) 0.7:0.3 (30% MTES) and (iii) 0.6:0.4 (40% MTES). The resulting X-ray diffraction patterns of the synthesized films after calcination (red) and patterns of the same films after 24 h incubation in buffer (blue) are given in **Figure 22**.

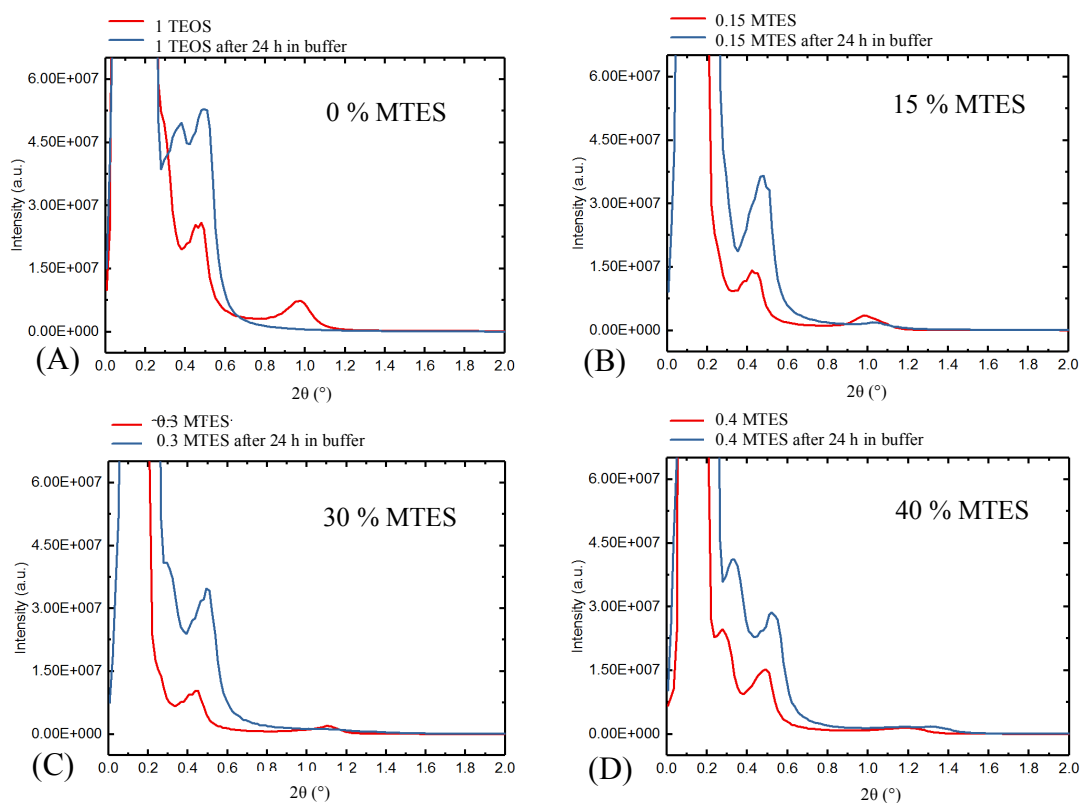


Figure 22: X-ray diffraction patterns of (A) unfunctionalized silica coating, (B-D) functionalized silica via co-condensation of TEOS:MTES using different MTES ratios (B: 15%; C: 30%; D: 40%). Synthesis were carried out under same sol composition (except of TEOS:MTES ratio) and same conditions given in Table 1. Red lines give the X-ray diffraction pattern after calcination and blue lines show the pattern after 24 h incubation of films in buffer (16.5 mM KH_2PO_4 , pH 7).

The diffraction patterns of the mesoporous silica films synthesized without co-condensation (0% MTES), hence of the unfunctionalized silica are shown **Figure 22 (A)**. It is visible that the peak at 1° (2θ) present in the pattern of the freshly synthesized film (red line) is not occurring for the pattern of the layer after 24 h of incubation in buffer solution. Therefore, it can be stated that the porous structure has decomposed. Diffraction patterns of the freshly synthesized films formed by co-condensation of TEOS and MTES, given in **Figure 22 ((B)-(D))** red lines) show a reflex at 1° (2θ) for 15% MTES, 1.12° (2θ) for 30 % MTES and 1.2° (2θ) for 40 % MTES. Hence, the higher the amount of MTES the more the peak $\sim 1^\circ$ (2θ) is shifted to larger angles, as well a decrease in intensity is recorded (compared with reflex obtained using 100% TEOS for synthesis). From the patterns after buffer incubation (**Figure 22 (A)-(D)** blue lines) it can be determined that the higher the amount of MTES hence, the higher the degree of methylation, the less change in diffraction pattern before and after incubation is visible.

The second functionalization method is a post-synthetic grafting through the usage of hexamethyldisilazane (HMDS) as methylation agent. With a thereby methylated film (TEOS HMDS) the same stability tests were performed, and the X-ray diffraction pattern is given in **Figure 23**.

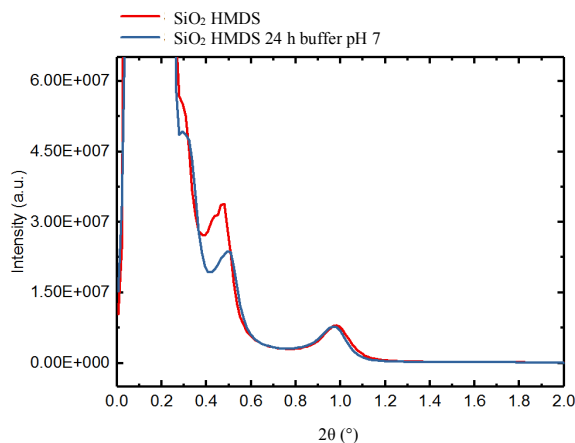


Figure 23: X-ray diffraction patterns of films synthesized using sol composition given in Table 1 with post-synthetic functionalization with HMDS. Red: freshly calcined film, Blue: film after 24 h in buffer (16.5 mM, pH 7)

From this graph, it is visible that the peak at position 1° (2θ) as well as the intensity of the reflex are identical before and after buffer incubation. Hence, we can conclude that a silica layer grafted with HMDS is stable in the buffer for at least 24 h.

In addition to the analysis *via* X-ray diffraction, the film thickness before and after incubation was investigated with the profilometer (see **Table 2**).

3.2.3 Evaluation of the Stability of the Mesoporous Silica Films in Buffer

Table 2: Film thicknesses before and after incubation in buffer (16.5 mM KH_2PO_4 , pH 7) for 24 h of unfunctionalized (SiO_2) and functionalized (15% - 30% MTES, co-condensation, SiO_2 + HMDS grafting) films.

Thickness	SiO_2	15% MTES	30% MTES	40% MTES	SiO_2 + HMDS
Calcined	585 nm	650 nm	626 nm	540 nm	620 nm
24 h buffer	46 nm	330 nm	535 nm	540 nm	610 nm

Through comparison of the thickness of the films before and after buffer incubation, the stability of the film can be additionally determined. From the film thicknesses given in **Table 2** as well as the diffraction patterns in **Figure 21**, it can be concluded that the higher the degree of methylation, the higher the stability of the film under aqueous conditions, which follows theory (see **Figure 20**). The most promising results concerning good pore formation as well as stability were obtained using post synthetic grafting with HMDS. Hence it can be concluded that throughout functionalization with methyl groups a film which is stable in buffer solution (16.5 mM KH_2PO_4) can be achieved.

Nevertheless, before evaluation of stability, unfunctionalized films were used for adsorption experiments since, such a fast decomposition was not expected for pH 7. Later, only with HMDS grafted silica films were used for investigation of the interaction of proteins with the mesoporous film.

The realization and the results of the performed protein adsorption experiments are presented in the following **section 3.3**. Therefore the interaction of LYS and LCR with (i) non-porous, silica (**section 3.3.2**) (i) mesoporous silica (**section 3.3.3**) (iii) non-porous, methylated silica (**section 3.3.4**) and (iv) mesoporous methylated silica (**section 3.3.5**) was performed. Advanced adsorption experiments towards the enrichment of proteins at low concentrations into a methylated film with 15 nm pores are given in **section 3.3.6**. As well as first approaches towards the monitoring of the activity of Lipase inside the pore is presented in **section 3.3.7**. In the beginning an overview of the workflow for performing the adsorption experiments is given in **section 3.3.1**.

3.3 Protein Adsorption on Mesoporous Silica Monitored by ATR FTIR Spectroscopy

In the following chapter the investigation of the interaction of Proteins (i) Lysozyme (LYS) and (ii) Lipase from *Candida rugosa* (LCR) with different silica surfaces (i) dense silica, (i) dense methylated silica, (iii) porous silica and (iv) methylated porous silica is presented. The adsorption out of aqueous solutions onto these surfaces was investigated using ATR FTIR spectroscopy. Here, **section 3.3.1** gives a short visualization of the overall process enabling investigation of the adsorption process performed within this thesis.

3.3.1 Workflow for Protein Adsorption Experiments

In the following section an overview of the general workflow of performed adsorption experiments is presented. Beginning with the preparation of an ATR crystal, modification of the surface and subsequent enrichment of proteins from aqueous solution monitored by ATR FTIR spectroscopy. In **Figure 24** the single steps are visualized, and a more detailed explanation is given below.

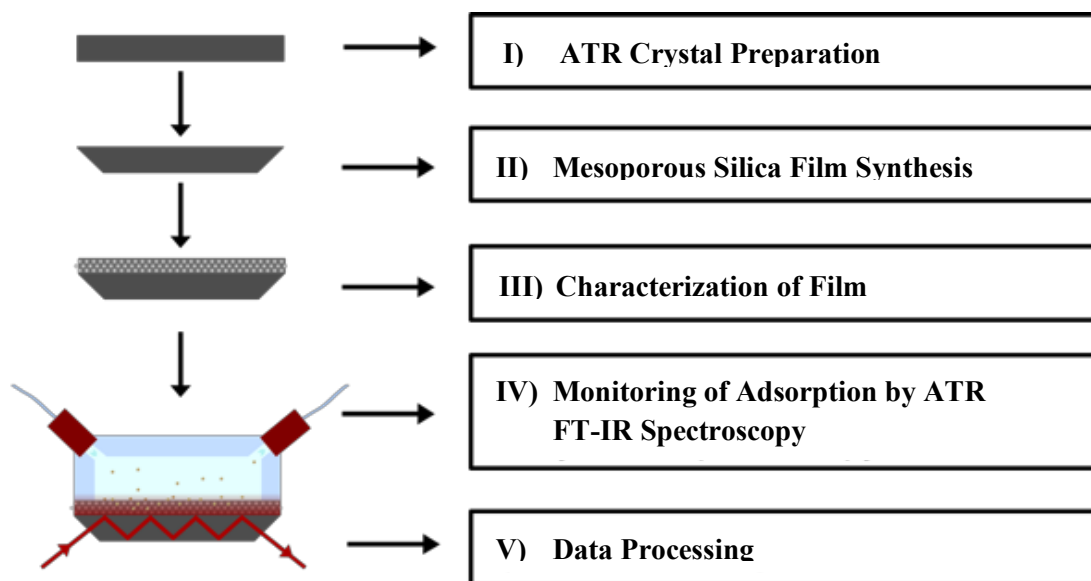


Figure 24: Scheme of the workflow. I) ATR crystal preparation by polishing narrow facets to an angle of 45° , II) Mesoporous Silica Film Preparation, III) characterization of the synthesized films using low-angle X-ray diffraction, IV) performing adsorption experiments in a flow cell, constant recording of spectra and v) data processing

I) ATR Crystal Preparation: Double-side polished CZ Si wafers of $20 \times 10 \times 0.525$ mm in size were provided by a collaboration partner (IMEC/ University of Gent). The narrow facets were polished to a angle of 45° which resulted in $N = 20$ active bounces or to 55° with $N = 14$ within the multi reflection element.

- II) **Mesoporous Silica Film Synthesis:** Polished silicon ATR crystals were coated with mesoporous silica films by spin-coating. Final porous structure was obtained by calcination and films were eventually post-synthetically functionalized with HMDS.
- III) **Characterization of the Films:** Low-angle X-ray diffraction was used for characterization and evaluation of the outcome of the film synthesis. Film thickness was determined using a profilometer.
- IV) **Monitoring of Adsorption by ATR FTIR Spectroscopy:**

For performing adsorption experiments a home-built 20 μL flow cell out of polymethylmethacrylate (PMMA) was mounted on top of the ATR crystal sealed with a FKM O-ring. Then the flow cell setup was inserted in the sample compartment of a Bruker Vertex 80v spectrometer. Solutions were applied using a peristaltic pump downstream of the flow cell (see **Figure 25**). The general sample application procedure for the adsorption experiments is:

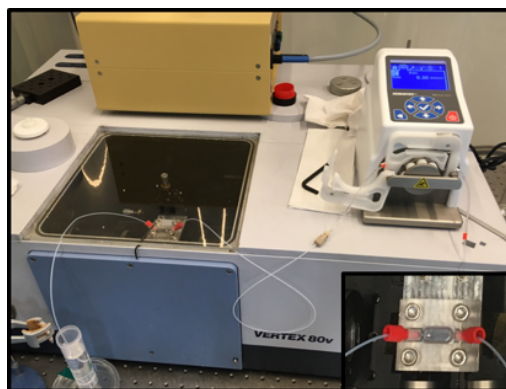


Figure 25: Picture of the spectrometer equipped with the home-built flow cell mounted on top of the ATR crystal (bottom right corner)

- 1) Equilibration of the system by flushing with buffer solution (16.5 mM KH_2PO_4 , pH 7) until a stable spectrum was recorded (~15 min).
- 2) Recording of background spectrum.
- 3) Protein application: Constant flow with protein buffer solution and continuous recording of spectra (every 30 seconds).
- 4) Removing loosely attached protein from flow cell by flushing with buffer at pH 7. Simultaneous recording of spectra.
- 5) Flush with e.g. buffer pH 3, PEG₂₀₀₀ in ethanol for protein removal from surface.

This general procedure was performed for all protein adsorption experiments, whereas depending on the used protein and surface, single steps (especially concerning protein removal) were adapted.

- V) **Data Processing:** A MatLab script was used for determination of the background corrected absorbance. Adsorption plots were generated by plotting the height of the amide II band at 1550 cm^{-1} (in A.U.) versus time (min) (details in **section 5.1.1**).

In the following sections results of the so performed adsorption experiments according to this process flow are presented.

3.3.2 Protein Adsorption Experiments on Uncoated Silica Surfaces

Prior to adsorption experiments using mesoporous silica films, protein adsorption on uncoated silica was investigated. Here important information for the possibility to distinguish between adsorption on a surface and adsorption into a porous network was gained (see **section 3.1.1.3**). For these experiments uncoated ATR crystals with $\theta = 55^\circ$ were used having a native SiO_2 layer of typically a few nm that can interact with the protein.

As a first protein, Lysozyme was used for experiments. This protein was chosen, since the protein is from a small size (14.3 kDa, $1.5 \times 2.5 \times 4.3$ nm [5]) and exhibits a pI of 11.3 (see **section 3.1.2**). For concentration dependent investigation of adsorption three different experiments with 1, 3 and 5 mg/mL LYS in buffer pH 7 were performed. Following the general procedure, described in **section 3.3.1** the adsorption plots given in **Figure 26 (B)** were obtained.

The resulting protein spectrum after $t = 18$ min flush of protein solution (3 mg/mL Lysozyme (1)) as well as a spectrum during buffer flush after protein adsorption ($t = 35$ min, (2)) are given in **Figure 26 (A)**.

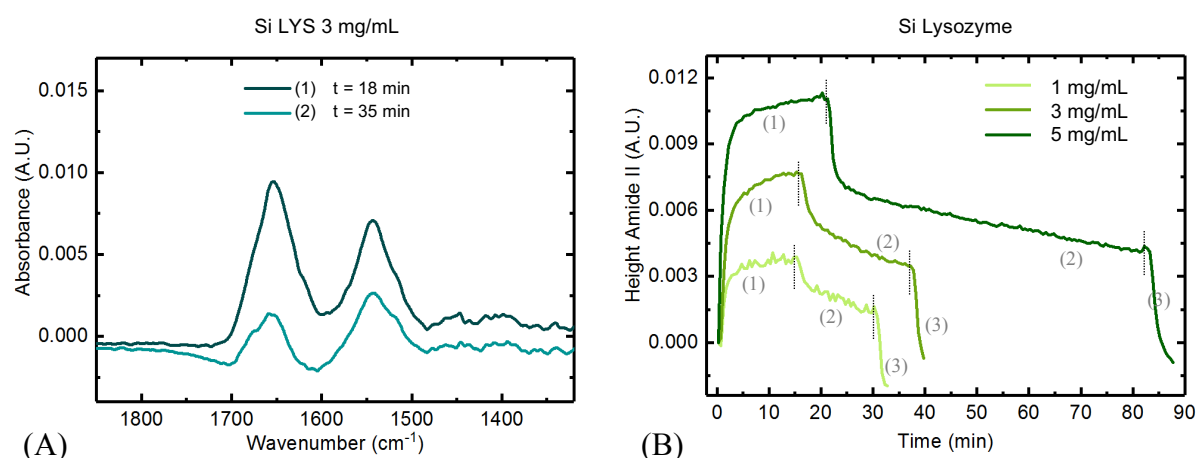


Figure 26: (A) Spectra of Lysozyme using an uncoated silicon ATR crystal (55°), 3 mg/mL LYS in 16.5 mM KH_2PO_4 (1) protein application $t = 18$ min, (2) buffer pH 7 wash $t = 35$ min. (B) Protein adsorption plots over time. Performed with different concentrations of Lysozyme (1 – 3 mg/mL) 0.5 mL/min. (1) flush with protein solution, (2) flush with buffer solution pH 7 and (3) flush with buffer pH 3.

For both spectra, the amide I (~ 1650 cm^{-1}) and amide II (1550 cm^{-1}) bands of Lysozyme are visible. Whereas upon flushing with buffer pH 7 (2) the shape and intensity of the amide I band is strongly altered. This arises from contributions of the changing water spectrum, because of air bubbles in the flow cell. During flushing of the solution air bubble formed for nearly every performed experiment. This is a problem, because eventually big air bubbles in

3.3.2 Protein Adsorption Experiments on Uncoated Silica Surfaces

the flow cell displace water in the cell, hence water absorption, which is compared to the background spectrum without air bubbles, is reduced. This results in a decreased or influenced signal around 1650 cm^{-1} . Therefore, the height of the amide II band and not the area is used for determination of the amount of protein, since the height of the amide II band was found to be less influenced by air bubbles.

In **Figure 26 (B)** the temporal progression of the adsorption using Lysozyme in buffer pH 7 at three different concentrations (1, 3, 5 mg/mL) is given. The different flushing sequences: **(1)** protein solution, **(2)** buffer at pH 7 followed by **(3)** buffer at pH 3 can be visually followed and a line highlights the exchange of the solution. The plot shows that the higher the applied concentration the higher the absorbance, hence the protein film formed on top of the ATR crystal. Interestingly, if washed with buffer pH 7, a non-negligible amount of Lysozyme stays adsorbed on the silica surface and a constant decrease of adsorbed protein can be observed. Protein is just slowly washed from the surface and *e.g.* for 5 mg/mL LYS, after 55 min of buffer wash with a constant velocity of 0.5 mL/min there is still protein on the surface. Only upon change of pH 3 leading to a change in surface charge the protein is totally desorbing from the silica surface (see **(3)** in **Figure 26 (B)**).

Hence, with these results I could prove the pH dependent adsorption of proteins with pI higher than buffer pH and silica as assumed in **section 3.1.2.**: Shortly, at pH 7 the silica surface is negatively charged (PCZ = 3.6), whereas Lysozyme is positively charged (pI = 11.3) therefore electrostatic interaction leads to adsorption. If pH is changed to pH 3, the silica surface charge is positive hence repulsion of Lysozyme occurs.

Having investigated adsorption onto non-porous silica surfaces, the next experiment were performed using a mesoporous silica film coated ATR crystal. Here a silica film with a 3D hexagonal structure and a pore size of 2 - 4 nm was casted onto the crystal. General procedure for performing the experiment was kept the same and results are shown in following **section 3.3.3.**

3.3.3 Protein Adsorption Experiments on Unfunctionalized Mesoporous Silica Films

For first investigation of the interaction of Lysozyme with mesoporous silica films, an established synthesis method for mesoporous silica films onto the ATR crystal was performed. Using CTAB as surfactant, a 3D hexagonal mesoporous silica film with 2-3 nm pores was synthesized. Within the work for the thesis, these first adsorption experiments were carried out in parallel to the optimization towards the formation of mesoporous silica films with large pore sizes using Pluronic F127 as surfactant (**section 3.2.2**).

For the experiments, all conditions were kept the same as reported for the adsorption experiments on uncoated silica ATR crystals (see **section 3.3.2**), except that a mesoporous silica layer was coated on top of the ATR crystal. The synthesized layer with number C01b was characterized by X-ray diffraction as well as film thickness was measured using profilometry (see **section 5.2**). The evaluated thickness was used for calculation of the fraction s of the intensity of the evanescent field inside the layer at the wavenumber of the amide II band. Leading to the following parameters for the 3D hexagonal layer: $d_{\text{film}} = 264$ nm, $s_{1550\text{cm}^{-1}} = 0.7624$, angle of incidence = 55° , pore size of ~ 3 nm.

Adsorption experiments were performed using concentrations of 5 mg/mL and 1 mg/mL of Lysozyme in buffer at pH 7. In **Figure 27 (A)/(B)** the resulting adsorption plots are given.

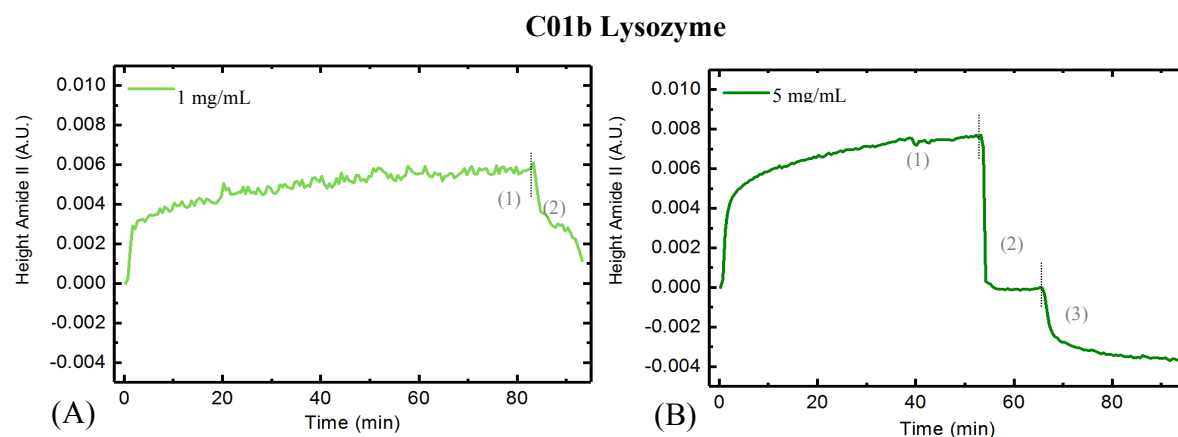


Figure 27: Adsorption plots of experiments using film C01b (3 nm pore size, $th = 264$ nm $s_{1550\text{cm}^{-1}} = 0.7624$) applying of solutions with 0.5 mL/min; (A) Lysozyme 1 mg/mL (1) flush LYS 1 mg/mL in buffer pH 7, (2) wash buffer pH 7; (B) Lysozyme 5 mg/mL (1) flush LYS 5 mg/mL in buffer pH 7, (2) wash buffer pH 7 and (3) wash buffer pH 3.

From **Figure 27** shows a similar progression of the absorbance of the amide II band in the adsorption plot using layer C01b as those using uncoated silica surfaces (**Figure 26**). A sharp increase of absorbance within the first minute followed by a slowly increasing quasi-plateau.

3.3.3 Protein Adsorption Experiments on Unfunctionalized Mesoporous Silica Films

However, observed absorbance is lower compared to uncoated Si crystals, which can be related to the lower fraction of the evanescent field above the layer because of the presence of the mesoporous silica film (see **Figure 14**).

In the spectra given in **Figure 28 (A)** the amide I (1650 cm^{-1}) and the amide II (1550 cm^{-1}) bands after 55 min flow (0.5 mL/min) of a 5 mg/mL Lysozyme solution (pH 7) are clearly visible (dark green line). Upon change to the buffer solution (pH 7) the spectrum changes, whereas a decrease in the amide II band can be referred to a desorption from loosely attached protein. Whereas, change in the spectra $\sim 1650\text{ cm}^{-1}$ can be attributed to changing water contributions due to air bubbles (blue) inside the flow cell.

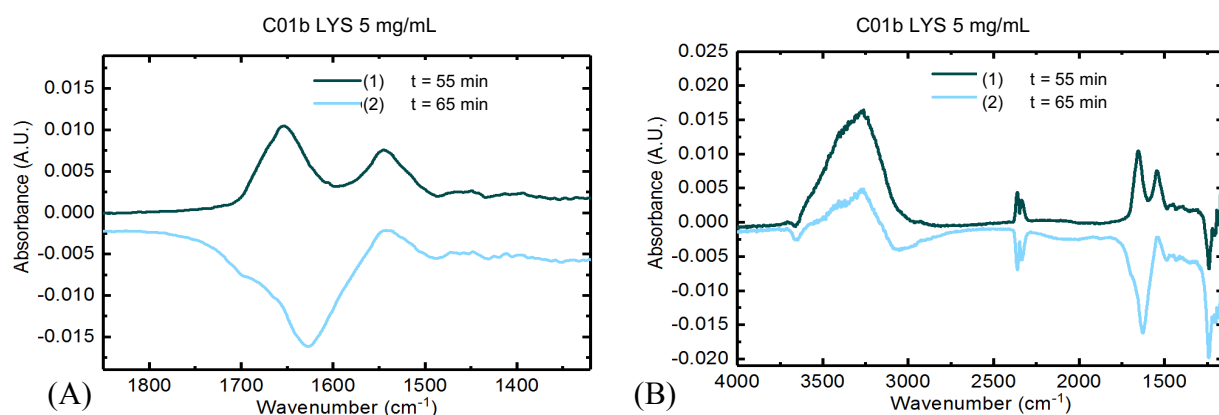


Figure 28: Spectra of the adsorption experiment using film C01b (55°) and Lysozyme 5 mg/mL in buffer solution pH 7 0.5 mL/min, (1) green spectrum 5 mg/mL LYS $t = 55\text{ min}$, blue spectrum (2) flush with buffer pH 7 $t = 65\text{ min}$, (A) close up to of amide I and amide II bands.

Whereas the full spectrum in **Figure 28 (B)** shows an increase in water absorbance $\nu_{as} \sim 3400\text{ cm}^{-1}$ (green line). Obviously more water fits in the pores giving rise to an increase in absorbance around $\nu_{as} \sim 3400\text{ cm}^{-1}$ and as well as $\delta(\text{O-H}) \sim 1650\text{ cm}^{-1}$ (green line). Hence, it can be stated that the amide I mode of LYS is superposed by the signal of the rising water content in the film. Rise in water absorbance could be due to slight destruction of the porous structure. Upon change to buffer, a decrease of water above the layer (because of air bubbles) lead to a decreasing peak arising from decrease in water vibrations ($\nu_{as} \sim 3400\text{ cm}^{-1}$ and $\delta(\text{O-H}) \sim 1650\text{ cm}^{-1}$, blue). Since the depth of penetration at 1650 cm^{-1} (350 nm) is higher than the silica film thickness ($t_h = 264\text{ nm}$) a strong decrease in absorption is recorded. Whereas due to smaller penetration depth at 3400 cm^{-1} (170 nm) decrease in water absorption is lower. Especially for the first adsorption experiments air bubble removal, without changing solution to a solution with lower surface tension (*e.g.* ethanol) was not yet optimized.

To confirm the hypothesis of potential film destruction in buffer solution the ATR crystal C01b was investigated visually and by X-ray diffraction after its use (see **Figure 29**).

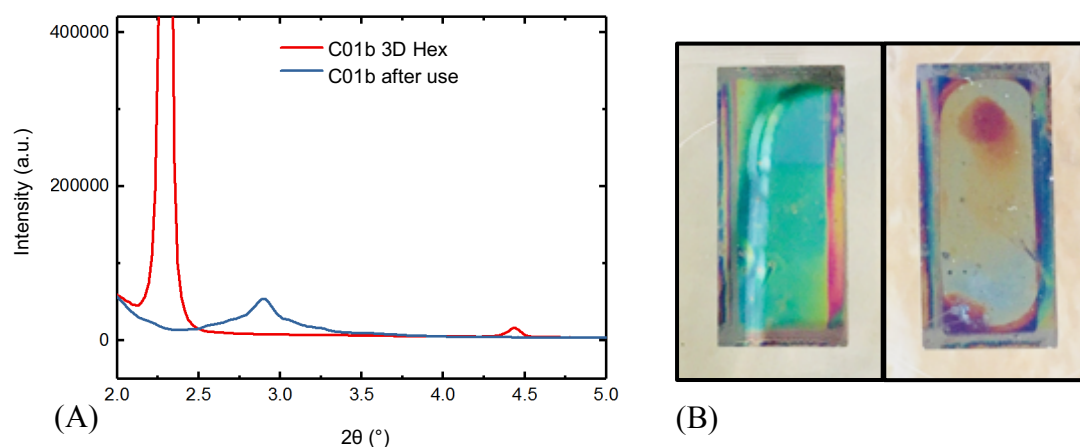


Figure 29: (A) X-ray diffraction pattern of ATR crystal C01b red: freshly synthesized 3D hexagonal structure, blue: ATR crystal C01b after use for adsorption experiments in buffer pH 7; (B) pictures of the ATR crystal C01b before use (left picture) and after the use for adsorption experiments (right picture).

If comparing the X-ray diffraction pattern in **Figure 29 (A)** of the freshly synthesized mesoporous silica film (red line) with the pattern of the coated crystal after use for adsorption experiment (blue line) it can be stated that the ordered mesostructure decomposed, because the reflections at 2.3° and 4.45° (2θ) arising from the primarily 3-dimensional hexagonal structure of the film had vanished. Furthermore, a difference in optical appearance of the films (see pictures of the ATR crystals before and after their use (**Figure 29 (B)**) left: fresh, right: used) is visible. Because of these findings and the later performed stability tests in buffer solution (**section 3.2.3**), no more experiments with unmodified mesoporous silica films were performed, since they are decomposed under these conditions.

Stabilization of the films was performed by post-synthetic modification of the films with HMDS. The results of the investigation of the interaction of proteins Lysozyme (LYS) and Lipase from *Candida rugosa* (LCR) with methylated mesoporous silica films are presented in the following **sections 3.3.4** and **3.3.5**.

3.3.4 Protein Adsorption Experiments on Methylated Silica Surfaces

In the following section the results of the protein adsorption experiments using an uncoated silicon ATR with a methylated silica surface are presented. Therefore, the synthesized porous films were functionalized with HMDS by reflux in acetone containing the silazane for 4 h (see **section 5.3.3**). In addition to LYS, Lipase from *Candida rugosa* was implemented, since this enzyme possesses interesting features towards its application in biocatalysis (see

3.3.4 Protein Adsorption Experiments on Methylated Silica Surfaces

section 3.3.5). Adsorption experiments were performed according to those using unfunctionalized silica surfaces (see **section 3.3.2**).

In **Figure 30 (A)** the resulting spectra using Lysozyme 3 mg/mL during (1) flush with protein solution pH 7 ($t = 30$ min), (2) flush with buffer solution pH 7 ($t = 40$ min) and (3) flush with buffer solution pH 3 ($t = 55$ min) are given. The resulting adsorption plots using 1 mg/mL and 3 mg/mL of LYS are given in **Figure 30 (B)**.

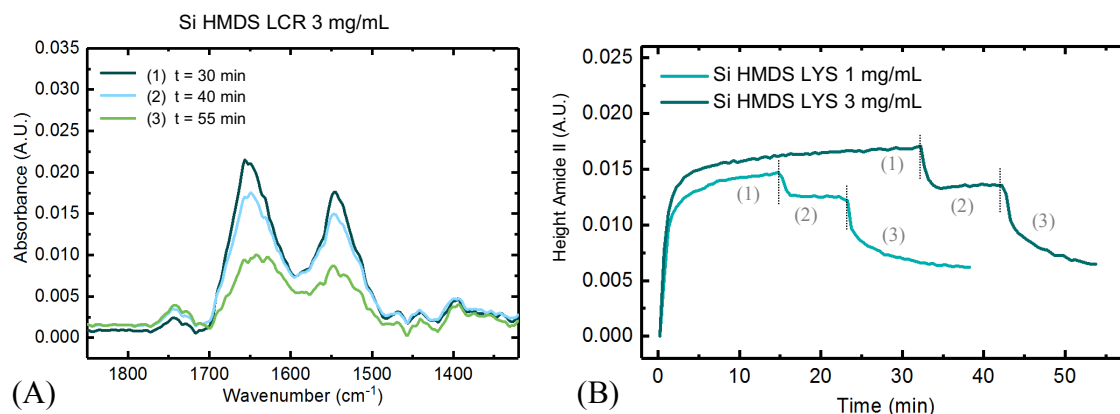


Figure 30: (A) Spectra of the adsorption experiment using Lysozyme (3 mg/mL pH 7) and a methylated silica surface (silicon ATR crystal 45°). (1) flush with 3 mg/mL LYS pH 7, after $t = 30$ min, (2) flush with buffer pH 7 after $t = 40$ min and (3) flush with buffer pH 3 after $t = 55$ min; (B) Adsorption plot: (1) flush 1 mg/mL LYS (light green) and 3 mg/mL LYS (dark green), (2) flush with buffer pH 7 and (3) flush with buffer pH 3.

From the adsorption plots it is visible that after 15 minutes of sample flow with protein solution the absorbance of the amide II band stays practically constant for both applied concentrations. If washed with a buffer of pH 7 protein absorbance decreases immediately but stays constant afterwards. Hence it can be concluded, that a certain amount of protein remains adsorbed. If the buffer is changed to pH 3 the signal decreases gradually, whereas in contrast to adsorption on unfunctionalized silica, a non-negligible amount of protein still stays adsorbed on the methylated silica surface. This can be related to the change in surface properties of the silica surface. Throughout methylation of the surface the electrostatic forces are lowered since the number of $-OH$ moieties is reduced by functionalization, while the hydrophobic interaction has a higher contribution to the adsorption process.

Note that absorption plots using films functionalized with HMDS (**Figure 30**) cannot be directly compared with the ones obtained from uncoated silica films (**Figure 26**). This is because functionalized ATR crystals (e.g. Si HMDS, BB189, SS63B) were polished to an angle of 45° which results in a number of active bounces inside the crystal of $N = 20$, whereas unfunctionalized ATR crystals (e.g. Si, C01b) were polished to an angle of 55° with $N = 14$.

This results in different effective pathlengths at 1550 cm^{-1} of $d = 6.34\text{ }\mu\text{m}$ for 45° ($N = 20$) and $d = 3.33\text{ }\mu\text{m}$ for 55° ($N = 14$).

For direct comparison the obtained absorbance for Lysozyme on uncoated surfaces the concentration of LYS can be calculated. Therefore, BEER'S Law (**Equation (4)**) with $\epsilon_{\text{LYS}} = 1.611 \times 10^4\text{ mL}/(\text{mg} \cdot \mu\text{m})$, and $d_e \cdot N = 6.34\text{ }\mu\text{m}$ for 45° and $d_e \cdot N = 3.33\text{ }\mu\text{m}$ for 55° was used for calculations (see **Table 3**). Now the adsorption of LYS onto silica and methylated silica surfaces can be compared.

Table 3: Results of calculations of Lysozyme concentration on the surfaces silica (Si) and silica functionalized with HMDS (Si HMDS) $\epsilon_{\text{LYS}} = 1.611 \times 10^4\text{ mL}/(\text{mg} \cdot \mu\text{m})$, $d_e \cdot N = 6.34\text{ }\mu\text{m}$ for 45° and $d_e \cdot N = 3.33\text{ }\mu\text{m}$ for 55° , Monolayer calculation using close packing of equal spheres $P = 0.74$ with radius $\text{LYS} = 1.5\text{ nm}$, surface area = 1 cm^2 , $MW_{\text{LYS}} = 14\text{ kDa}$, $\text{weight}_{\text{monolayer}} = 0.365\text{ }\mu\text{g LYS}$

Enzyme	LYS	LYS	LYS	LYS	LYS
ATR Crystal	Si HMDS 45°	Si HMDS 45°	Si 55°	Si 55°	Si 55°
Conc. applied protein solution [mg/mL]	1	3	1	3	5
Height of amide II after protein solution application (1) [A.U.]	0.015	0.017	0.0037	0.0077	0.0111
Height of amide II after wash pH 7 (2) [A.U.]	0.013	0.014	0.0015	0.0035	0.0042
Height of amide II after wash pH 7 (3) [A.U.]	0.006	0.006	-0.0019	-0.0012	-0.0011
Adsorbed amount after protein application (1) [mg protein /cm ³]	14.21	16.55	6.98	14.27	20.74
Adsorbed amount after wash pH 7 (2) [mg protein /cm ³]	12.30	13.27	2.78	6.47	7.84
Adsorbed amount after wash pH 7 (3) [mg protein /cm ³]	6.10	6.30	-3.59	-2.33	-2.11
Ratio (A.U. Wash pH 7/ A.U. Monolayer)	1.07	1.15	0.18	0.42	0.51
Protein on Si /Si HMDS surface (weight_{monolayer} *Ratio) [μg]	0.39	0.42	0.07	0.15	0.19

In addition, to calculations of concentrations, the theoretical absorbance expected if a monolayer of protein would be on top of the ATR crystal was calculated. Therefore, a close-packing of equal spheres of protein (filling fraction equals to 0.74), composed of protein particles of a defined radius ($\text{LYS} = 1.5\text{ nm}$) as well as other parameters were used for calculations (see **section 5.1.1** for details). The ratio of the obtained absorbance of adsorbed protein (wash with pH 7) and the theoretical absorbance of a monolayer gives the number of monolayers on the surface. Using the theoretical number of proteins and their molecular weight, the amount of protein forming the monolayer can be expressed in grams. If multiplying the weight of the monolayer with the obtained ratio, I can approximate the amount of protein adsorbed on the surface (in μg).

3.3.4 Protein Adsorption Experiments on Methylated Silica Surfaces

From the ratios given in **Table 3** it can be said, that on methylated silica, Lysozyme is forming a monolayer, even if low concentrations of protein are applied. Ratios for the unmodified silica surfaces show that in comparison a lower amount of protein is adsorbed accounting to up to half of a monolayer (which in praxis means an average of covered and not covered patches on the surface), additionally, here the concentration of the applied solutions seems to have bigger influence. Hence, we can conclude that methylation of the surface leads to a higher protein (Lysozyme) adsorption on the surface.

Since functionalization with HMDS leads to a more hydrophobic surface, interaction with the highly lipophilic protein Lipase was also investigated. As Lipases are designed to work at interfaces between water and oil, I assumed a high adsorption on a hydrophobic support being likely.

First results of the investigation of the interaction of LCR with methylated silica surfaces are shown in **Figure 31**. Experiments were performed according to those using LYS.

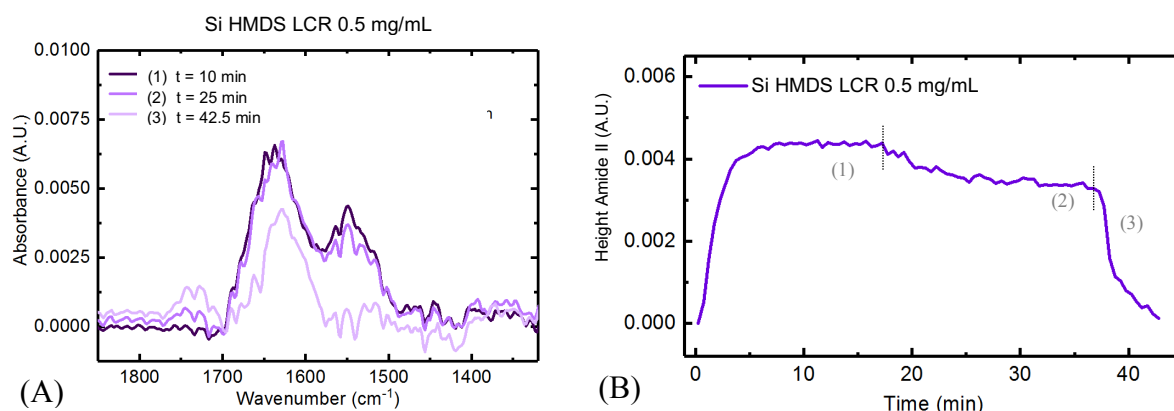


Figure 31: (A) Spectra of Lipase from *Candida rugosa* using an uncoated silicon ATR crystal functionalized with HMDS, 0.5 mg/mL LCR in 16.5 mM KH_2PO_4 buffer pH 7. (B) Protein adsorption plots over time. LCR (0.5 mg/mL). First: flush with protein solution, flush with buffer solution at pH 7 and flush with buffer pH 3.

Because of the low solubility of LCR in buffer solution, the maximum concentration, which was used, was 0.5 mg/mL. In **Figure 31 (A)** it is visible that despite the low concentration amide I and amide II bands are arising. The shape of the bands upon flushing with buffer (2) is influenced by water vapor absorption due to insufficient drying of the spectrometer's sample compartment. The progression of adsorption in **Figure 31 (B)** is similar to the adsorption curve using LYS (**Figure 30 (B)**). Whereas it is visible that by flush with pH 3 (3) LCR is, in contrast to LYS desorbed from the surface yielding an absorbance equal to 0. The peak $\sim 1650\text{ cm}^{-1}$ and band $\sim 1740\text{ cm}^{-1}$ in **Figure 31 (A) (3)** are spectral changes arising if flushing with pH 3, which were not assigned in more detail.

Same calculations as for LYS were performed using the data obtained from the LCR adsorption experiment with: $\epsilon_{LCR} = 2.799 \times 10^{-5} \text{ mL}/(\text{mg} \cdot \mu\text{m})$, and $d_e \cdot N = 6.34 \mu\text{m}$ for 45° using BEERS Law (**Equation (4)**).

Table 4: Results and calculations for adsorption experiment of 0.5 mg/mL LCR interaction with Si HMDS with $\epsilon_{LCR} = 2.799 \times 10^{-5} \text{ mL}/(\text{mg} \cdot \mu\text{m})$, $d_e \cdot N = 6.34 \mu\text{m}$ (45°) using Beers Law for concentration determination and monolayer calculation using close packing of equal spheres ($P = 0.74$) with radius LCR = 2.5 nm, surface area = 1 cm^2 , $MW_{LCR} = 60 \text{ kDa}$, $\text{weight}_{\text{monolayer}} = 0.563 \mu\text{g LCR}$

Height of amide II after protein solution application (1) [A.U.]	Height of amide II after wash buffer pH 7 (2) [A.U.]	Adsorbed amount after protein application (1) [mg protein /cm ³]	Adsorbed amount after wash pH 7 (2) [mg protein /cm ³]	Ratio (A.U. Buffer pH 7/ A.U. Monolayer)	LCR on Si HMDS ($\text{weight}_{\text{monolayer}} \cdot \text{Ratio}$) [μg]
0.00436	0.0034	24.56	19.11	1.71	0.97

Throughout referring to the signal expected if a monolayer would be adsorbed, we can say that LCR forms an almost complete bilayer on the methylated silica surface. Furthermore, due to adsorption and hence enrichment onto the surface a signal comparable with a $\sim 25 \text{ mg/mL}$ LCR solution obtained from transmission measurement with equal pathlength was observed. Therefore, simple adsorption of proteins onto planar surfaces leads to an enrichment factor of 50. Hence, calculation of the limit of detection would lead to a theoretical LOD of 0.22 mg/mL LCR (for calculation see **section 5.1.1**).

All in all, it can be stated that for LYS adsorption on a methylated silica surface is higher than on an unfunctionalized silica surface. Both proteins (LYS and LCR) form a monolayer or two monolayers, respectively, on the methylated silica surface. Adsorption of proteins on methylated silica leads to an increase in protein concentration on the surface and therefore enables the detection of Lipase at low concentrations.

By the implementation of a porous methylated silica surface, more surface for adsorption is provided. Hence it is considered to further enrich the protein in the region of the evanescent wave, and therefore even lower concentrations of the analyte can be investigated (lowering of limit of detection [15]). Therefore, and because of the fact that unfunctionalized porous films are not stable under buffer conditions, methylated mesoporous silica films were implemented for advanced adsorption experiments. The results of the experiments for investigation of the interaction of the proteins LYS and LCR with methylated mesoporous silica films with 7-8 nm or $\sim 15 \text{ nm}$ pores are presented in the following **section 3.3.5**.

3.3.5 Protein Adsorption Experiments with Methylated Mesoporous Silica Films

In order to investigate protein adsorption into methylated silica mesopores, mesoporous silica films functionalized with HMDS were prepared on ATR crystals (see **section 3.2**). Here, films with two different pore sizes, ~7 nm (BB189) and ~15 nm (SS63B) were used for investigation of adsorption of Lysozyme and Lipase from *Candida rugosa*.

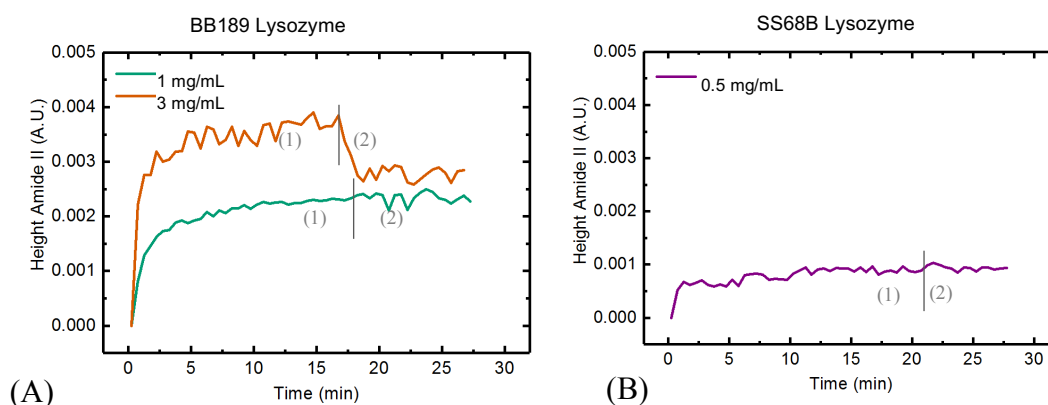


Figure 32: (A) Adsorption plot using the film BB189 (HMDS) with 7-8 nm pores, film thickness of 382 nm using 1 mg/mL and 3 mg/mL Lysozyme application, Wash buffer pH 7 after 17 min; (B) Protein adsorption plot using film SS68B (HMDS) with 15 nm pores and a film thickness of 625 nm applying 0.5 mg/mL Lysozyme and buffer pH 7 $t = 23$ min.

The resulting adsorption plots of the interaction of Lysozyme with film BB189 (~7 nm, HMDS, $t_h = 382$ nm) and film SS68B (~15 nm, HMDS, $t_h = 625$ nm) are given in **Figure 32 (A)** and **(B)**. It is visible that after 15 minutes, the intensity of the amide II band stays almost constant for all experiments. Therefore, it can be concluded, that for both films no more protein is adsorbing after 15 min. In addition, looking at the intensity of the obtained signal, the signal stays very low (single digit mA.U. values), which is a first hint for adsorption on top of the film only. The farther from the ATR crystals surface the less intense is the evanescent field. Hence, if the protein is solemnly adsorbed on the top of the surface, the signal stays very low. Whereas if protein is adsorbed inside the pores, the analyte reaches a region with higher light intensity, hence a higher signal is gained.

In order to verify the proteins position, i.e. on top of the film or within the pores, a constant height of the surface, hence the stability of the film is essential. Results of the performed stability tests (**section 3.2.3**) showed that the thickness of a HMDS functionalized mesoporous silica film layer is constant and XRD patterns remains stable. Therefore, calculations proofing of the entrance of the protein into the mesoporous network can be performed (see **Table 5**).

Based on the results of the experiments performed with uncoated methylated silica surfaces (**section 3.3.4**), the theoretical absorbance, expected on top of the film with a constant thickness th can be calculated. Therefore, the absorbance obtained on an uncoated ATR crystal where the height $z = 0$ hence with 100% of the intensity of the evanescent field is multiplied with the fraction of the evanescent field above the investigated film $(1-s)$. The calculation of the fraction of the evanescent field within the film s as well as further explanation is presented in **section 3.1.1.3**. Then a ratio of the obtained absorbance using the coated layers and the theoretical absorbance on top of the film is formed. If the ratio is larger than 1 it can be stated that the protein must be inside the pore, however, if the ratio is around 1 adsorption was most likely mainly on the films surface. Therefore, we assume for ratios around 1 that no protein has penetrated the film.

Table 5: Calculations of Lysozyme amount (concentration) using films BB189 (7 nm) and SS63B (15 nm) with $\epsilon_{LYS} = 1.611 \times 10^{-4} \text{ mL}/(\text{mg} \cdot \mu\text{m})$, $d_e \cdot N = 6.34 \mu\text{m}$ for 45° ,

Enzyme	LYS	LYS	LYS
ATR Crystal	BB189	BB189	SS68B
Conc. applied protein solution [mg/mL]	1	3	0.5
Height of amide II after protein solution application (1) [A.U.]	0.0024	0.0037	0.0009
Height of amide II after wash pH 7 (2) [A.U.]	0.0023	0.0028	0.0009
Adsorbed amount after protein application (1) [mg protein /cm ³]	2.34	3.65	0.89
Adsorbed amount after wash pH 7 (2) [mg protein /cm ³]	2.25	2.74	0.87
s	0.85	0.85	0.96
$A_{z=0}$ [A.U.]	0.0126	0.0136	0.0126
$A_{th} (A_{z=0} \cdot (1-s))$ [A.U.]	0.0019	0.002	0.0006
ratio (A.U. wash pH 7 / A.U. th (1-s))	1.22	1.38	1.57

Concentrations for Lysozyme adsorption on films BB189 and SS68B are given in **Table 5**. The obtained ratios are all around 1. Therefore, we can be concluded, that LYS is only adsorbed on the surface and not accumulated inside the pores. This is quite interesting, since the pore sizes (~ 7 or ~ 15 nm) are definitely larger than the size of Lysozyme ($1.5 \times 2.5 \times 4.3$ nm [5]). Therefore, these results of the adsorption experiments were rather unexpected and at this point only assumptions can be made to explain this behavior. A possible reason could be, that breaking the solvation shell and adsorption to a hydrophobic surface (contact angle of ca. 90°) would be energetically unfavorable hence interaction with water is more likely than with the surface. This hypothesis could be verified if using films functionalized with hydrophilic organic moieties. Furthermore, one can assume that proteins form aggregates of a size larger than the pores. These aggregates could adsorb on the surface and block the pores.

3.3.5 Protein Adsorption Experiments with Methylated Mesoporous Silica Films

As a second protein Lipase from *Candida rugosa* was taken for investigation of interaction with methylated mesopores. The experiments were performed using film BB189 with 7-8 nm and a film thickness of $th = 382$ nm and a film SS63B with 15 nm pores and a film thickness of $th = 600$ nm and a protein solution of 0.5 mg/mL of Lipase from *Candida rugosa*. The resulting adsorption plots for BB189 and SS63B are given in **Figure 33**.

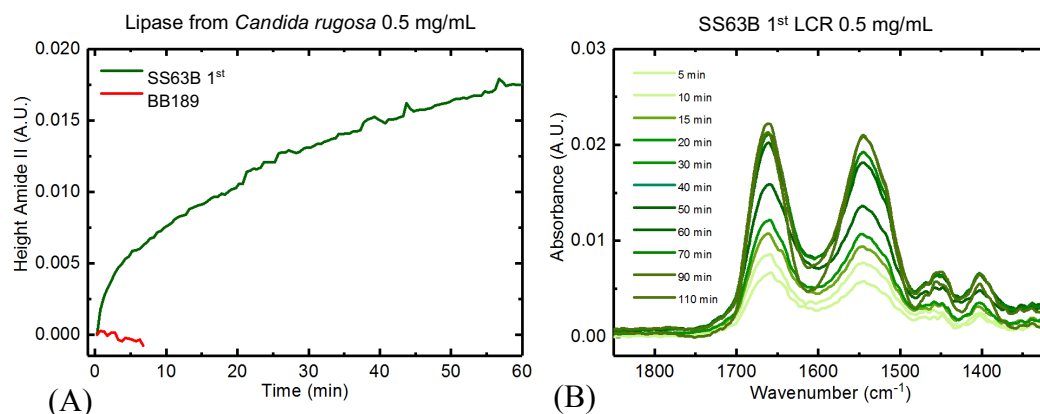


Figure 33: (A) Protein adsorption plot flushing 0.5 mg/mL Lipase from *Candida rugosa* (16.5 mM KH_2PO_4 , pH 7) over film BB189 (red) and film SS63B; (B) Spectra obtained while flushing 0.5 mg/mL Lipase over film SS63B, Spectra show the rise in amide bands over time.

By comparison of the adsorption plots using film BB189 with ~ 7 nm pores and SS63B with ~ 15 nm pores in **Figure 33 (A)** a tremendous difference in the intensity of the height of the amide II band is visible. Due to the extremely low signal of the amide bands obtained with film BB189 the experiment was canceled after 7 minutes. Whereas, if the film with the 15 nm pores (SS63B) was used a constant increase in the signal of the amide II band over time was detectable (see **Figure 33 (A)**). The obtained spectra are given in **Figure 33 (B)**. Hence, first indications towards the enrichment of LCR inside the 15 nm pores are given.

To proof our finding, the experiment was repeated. Protein removal turned out to be difficult and therefore, the first film was again calcined at 400°C to decompose the protein. After calcination the film was again used for adsorption experiments (SS63B 2nd **Figure 34**).

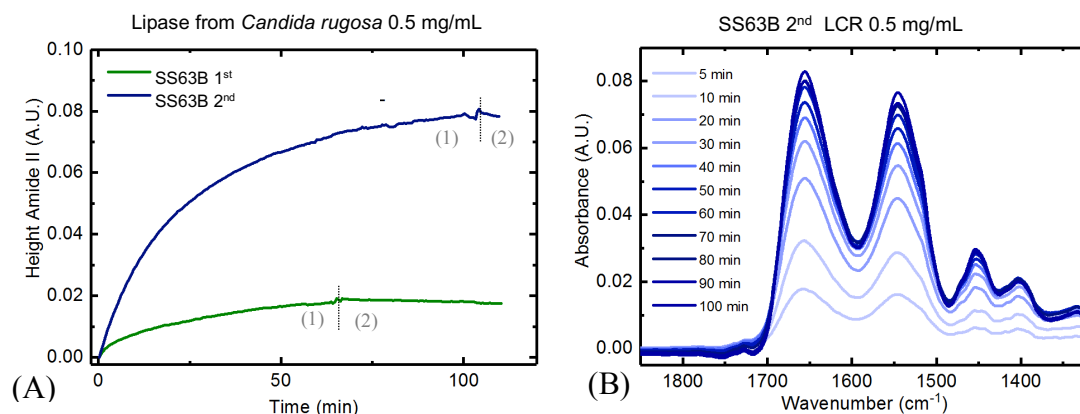


Figure 34: (A) Protein adsorption for 0.5 mg/mL Lipase from *Candida rugosa* with film SS63B 1st use: 1 mL/min; 2nd use: after protein removal by calcination, 1.5 mL/min: (1) flush with protein solution LCR 0.5 mg/mL in buffer pH 7 and (2) flush with buffer pH 7; (B) Recorded spectra while flushing 0.5 mg/mL Lipase (1) over layer SS63B 1st. Spectra show the rise in amide bands over time.

From **Figure 34** it is visible that the intensity of the amide II band for the second adsorption experiment of film SS63B is 4 times higher than for the first adsorption experiment. An intensity of 80 mA.U. for proteins amide bands in aqueous solutions is high. Since results of the repeated adsorption experiment using layer SS63B were deviating, a new ATR crystal with 15 nm pores was synthesized (SS68B).

Again, adsorption experiments were performed using 0.5 mg/mL LCR as well as keeping all parameters the same, but taking the freshly synthesized film SS68B. Whereas, now another way for protein removal after first adsorption experiment was established to avoid calcination. After trial of various solvents as (EtOH, heptane, buffer pH 3, CTAB in water) for protein removal PEG₂₀₀₀ (polyethylene glycol, MW = 2000 g/mol) dissolved in ethanol was found to be the best option to remove the protein from the porous film. After, removal of PEG with CTAB and buffer equilibration of the film, the adsorption experiment was repeated. The obtained spectra were processed, and the adsorption plots are given in **Figure 35 (A)** for 0.5 mg/mL and film SS68B (15 nm pores, 625 nm thickness), with protein removal with PEG₂₀₀₀ after the first experiment.

3.3.5 Protein Adsorption Experiments with Methylated Mesoporous Silica Films

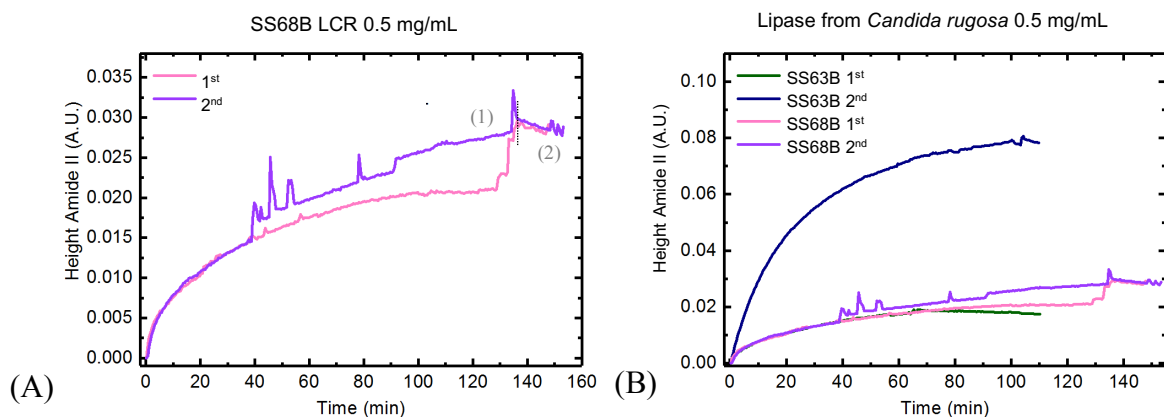


Figure 35: (A) Protein adsorption plot flushing 0.5 mg/mL Lipase from *Candida rugosa* (16.5 mM KH_2PO_4 , pH 7) over film SS68B, 1st with freshly synthesized layer, 2nd after removal of LCR with PEG₂₀₀₀ in EtOH; (B) Comparison of all adsorption plots performed with films of 15 nm in pore size. SS63B 1st: freshly synthesized, SS63B 2nd: after LCR removal by calcination, SS68B 1st: freshly synthesized, SS68B 2nd: after LCR removal by PEG₂₀₀₀ in EtOH;

From the adsorption curves in **Figure 35 (A)** it is visible, that both experiments led to same trend and height of the curves. The fluctuations and the big shift in the curve of the first use is because of air bubbles, which were accumulating in the flow cell. Manual removal of air bubbles leads to a sharp increase in signal, which can be seen in the trend of the curves. For both experiments, protein solution was changed to buffer solution at $t = 110$ min. After successful removal of all air bubbles, the heights of the amide II bands are almost identical. In addition, if comparing all four experiments using films with 15 nm pores (see **Figure 35 (B)**), it is visible that adsorption curves from SS63B first use, SS68B first use and SS68B second are very similar which proofs reproducibility of experiments and the films reusability. For all experiments using 15 nm pores flushing with buffer pH 7 leads to a slight decrease in the absorbance of amide II band. This is most probably due to slight leaching of the protein out of the mesoporous film or because of removal of the monolayer formed on top of the film.

Furthermore, we assume that second calcination of the film leads to its transformation. Therefore, protein removal with PEG₂₀₀₀ shall be preferentially used, in order to use the film several times.

The hereby obtained data were used to calculate concentrations of the protein inside the film using BEERS Law with: $\epsilon_{\text{LCR}} = 2.799 \times 10^{-5} \text{ mL}/(\text{mg} \cdot \mu\text{m})$, and $d_e \cdot N = 6.34 \mu\text{m}$ (45 °) the concentration of the protein inside the layer can be evaluated. The results are given in **Table 6**.

Table 6: Calculations of protein concentration) With $\epsilon_{LCR} = 2.799 \times 10^{-5} \text{ mL}/(\text{mg} \cdot \mu\text{m})$, $d_e \cdot N = 6.34 \mu\text{m}$ (45°) for (1), $d_{e, \text{film}} = d_e \cdot N$ for protein in film, $A_{z=0} = 0.0034$, Ratio = A.U. Wash pH 7/ ($A_{z=0} \cdot (1-s)$) with specific values for layer: SS63B $th = 600 \text{ nm}$, $s = 0.95$, SS68B = 625 nm $s = 0.96$;

ATR Crystal	SS63B 1 st	SS63B 2 nd	SS68B 1 st	SS68B 2 nd
conc. Applied Protein solution [mg/mL]	0.5	0.5	0.5	0.5
Height of amide II after protein solution application (1) [A.U.]	0.0188	0.0813	0.0288	0.0293
Height of amide II after wash pH 7 (2) [A.U.]	0.0176	0.0811	0.0284	0.0286
Adsorbed amount after wash pH 7 (2) [mg protein /cm ³]	105.9	458.0	162.2	164.9
$A_{th} (A_{z=0} \cdot (1-s))$ [A.U.]	0.00017	0.00017	0.00015	0.00015
ratio (A.U. Wash pH 7 / $A_{z=0} (1-s)$)	101.97	470.35	186.18	187.56
Protein in Film [mg/cm ³], $d_{e, \text{film}}$	94.0	433.5	152.6	153.8

Calculations in **Table 6** show that the ratio of the measured protein absorbance using the film and the theoretical calculated absorbance if only surface adsorption is occurring, is definitely higher than 1. Therefore, a proof of protein adsorption into the porous layer is given, since the signal obtained is e.g. ~180 times higher than expected if protein would be adsorbed on top of the film. The values obtained from the second use of layer SS63B must be discarded, since most probably the film was altered during second calcination.

Hence, it can be concluded, that Lipase is enriched inside the methylated mesoporous silica layer with pore sizes of 15 nm. Out of a solution with a concentration of 0.5 mg/mL in buffer pH 7 a concentration of ~150 mg/cm³ can be accumulated inside the film. This corresponds to an enrichment factor of 300. Hence, calculation of the limit of detection would lead to a theoretical LOD of 0.026 mg/mL LCR (for calculation see **section 5.1.1**).

Given these encouraging results, using the film for protein enrichment out of solution, and therefore detecting low concentrations could be of interest. To this end, experiments using very low concentrations of Lipases were performed. The results are presented in the following **section 3.3.6**.

3.3.6 Detection of Lipase at Low Concentrations

Within this section performed experiments towards the detection of Lipase at low concentrations using a coated ATR crystal SS69B (synthesized as SS63B, $th \sim 609 \text{ nm}$, $\sim 15 \text{ nm}$ pore size) are presented.

In order to investigate the concentration dependency of the absorbance of lipase and reaching towards the determination of the concentration of an applied protein solution the experimental procedure was the following: 2 mL of different concentrations of LCR in buffer pH 7 were

3.3.6 Detection of Lipase at Low Concentrations

applied to the film (1 mL/min). After protein solution application (2 mL), the film was flushed with buffer, and spectra were recorded every 15 seconds. After protein application, in order to remove the protein from the pores, firstly PEG₂₀₀₀ in ethanol (2 min), CTAB in water (2 min) and finally buffer was flushed over the film (equilibration for 15 min). Short ethanol flushes between solvent exchange for air bubble removal was performed. Concentrations ranging from 0.025 - 0.5 mg/mL were applied in the following order: 0.05 mg/mL, 0.2 mg/mL, 0.025 mg/mL, 0.5 mg/mL, 0.1 mg/mL, 0.4 mg/mL and 0.3 mg/mL.

The resulting absorption plots are shown in **Figure 36 (A)**.

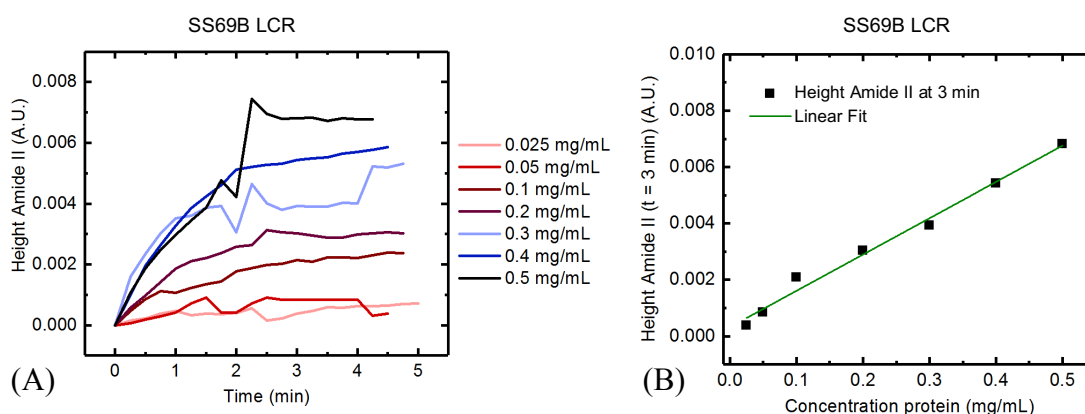


Figure 36: (A) Adsorption plot of different applied concentration experiment using SS69B and 2 mL of LCR solution ranging from 0.025-0.5 mg/mL in buffer (16.5 mM KH₂PO₄, pH 7), (B) Calibration curve of SS69B and LCR single data points were taken at $t = 3$ min, linear fit shows correlation of absorbance with applied concentration of LCR (2 mL).

From **Figure 36 (A)** it is visible, that the higher the applied concentration, the higher is the absorbance of the amide II band. Fluctuations ~ 2 min are due to solvent exchange to buffer solution, whereas upon buffer wash ~ 3 min a relatively stable height was observed. Hence, the value for absorption at 3 min was plotted against the applied concentration (see **Figure 36 (B)**). Here, a linear correlation between the applied concentration of LCR and the resulting absorbance is obtained with: $y = a + b \cdot x$ with $a = 3.22097 \times 10^{-4} \pm 1.80779 \times 10^{-4}$, $b = 0.01287 \pm 6.43111 \times 10^{-4}$, Pearson's $r = 0.99381$, R-Square (COD) = 0.98767 (calculated by linear fit in the program Origin). Thereby first approaches towards the detection and quantification of Lipase in low concentrations from 25 – 500 $\mu\text{g/mL}$ were shown.

To evaluate if the applied total amount of protein results in same absorbance, 5 mL of solution 0.2 mg/mL and 2 mL of 0.5 mg/mL, hence both times 1 mg of protein was applied to film SS69B (see **Figure 37**).

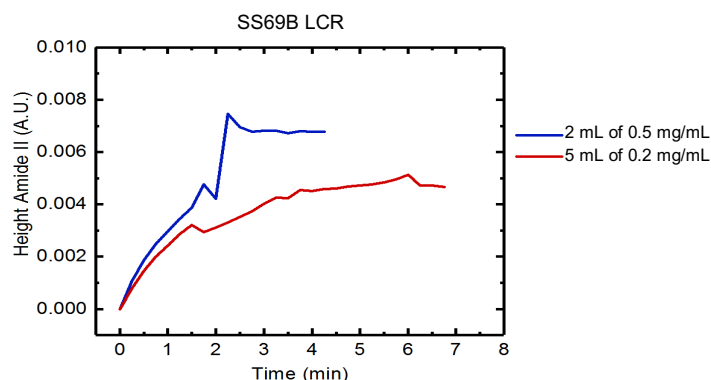


Figure 37: Adsorption plots using film SS69B and LCR. Applying 2 mL of 0.5 mg/mL LCR (blue line) and 5 mL of 0.2 mg/mL LCR (red line), followed by buffer wash for 2 min (16.5 mM KH_2PO_4 , pH 7),

From the adsorption plot in **Figure 37** it is visible that the applied concentration is influencing the obtained signal. Total amount of protein was equal for both experiments, but the obtained height of the amide II band is different. From comparing the measurement using 2 mL (see **Figure 36**) and 5 mL of 0.2 mg/mL (**Figure 37**) it is visible that using higher amounts of solution of the same concentration results in a higher signal. Therefore, it can be concluded, that the concentration as well as the total amount of applied solution are influencing the obtained absorbance.

In the last **section 3.3.7** the determination of the activity of lipase determined by FTIR spectroscopy is presented.

3.3.7 Approaches towards Activity Monitoring of LCR in Silica Pores and on Silica Surfaces

Within this section first approaches towards the determination of the activity of lipase inside the pore as well as surface adsorbed LCR are presented. Therefore, the substrate triacetin (glycerintriacetate) was dissolved in buffer pH 7 or in heptane with a concentration of ~ 320 mM [48]. Triacetin is an ester which is used for activity measurement of lipases. The enzyme catalyzes the hydrolysis of the ester to glycerin and acetic acid (see **Figure 38**).

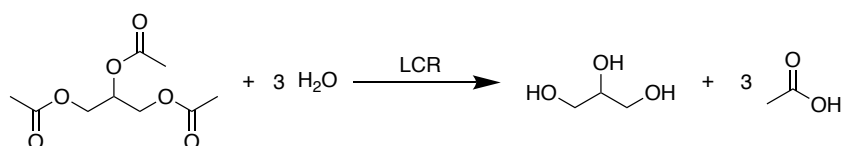


Figure 38: Reaction equation of hydrolysis of triacetin to glycerin and acetic acid catalyzed by Lipase (LCR)

For enzymatic activity experiments protein was enriched inside the film or on the silica surface and subsequent flushing of a substrate solution. After ~ 1 min of application of the solution (1 ml/min), flow was stopped, and spectra were continuously recorded.

3.3.7 Approaches towards Activity Monitoring of LCR in Silica Pores and on Silica Surface

First, experiments determining the enzymatic activity were performed using triacetin in buffer at pH 7 as substrate and the film SS63B after 2nd application of LCR. For time resolved tracing of the enzymatic hydrolysis of triacetin the height of the ester band $\sim 1730\text{ cm}^{-1}$ was plotted over time (see **Figure 39 (B)**).

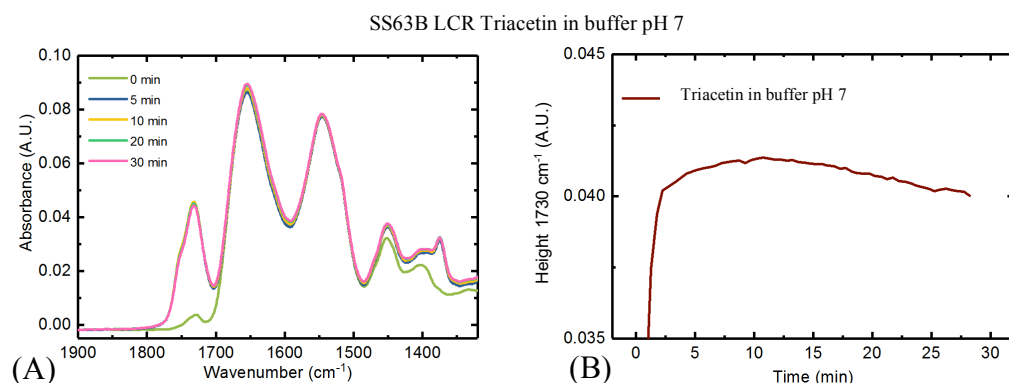


Figure 39: Film SS63B, 0.5 mg/mL LCR: (A) Spectra of the adsorbed LCR and triacetin in buffer pH 7 plotted from 0-30 min; (B) Evolution of the ester band of triacetin in buffer pH 7 over time.

From **Figure 39 (A)** it is visible that the ester band at $\sim 1730\text{ cm}^{-1}$ stays rather constant over time. Therefore, low activity of LCR inside the porous film SS63B with triacetin in buffer at pH 7 as substrate can be stated. For confirmation of the obtained result the experiment was performed a second time after adsorption of LCR inside the film SS68B. Again, triacetin dissolved in buffer pH 7 ($\sim 320\text{ mM}$) as well as triacetin in heptane was applied for $\sim 1\text{ min}$ ($\sim 2\text{ mL}$) and the flow was stopped. Temporal change of the band $\sim 1730\text{ cm}^{-1}$ was plotted over time given in **Figure 40**. A background spectrum was recorded before triacetin solution application for a better traceability of the applied amount of triacetin.

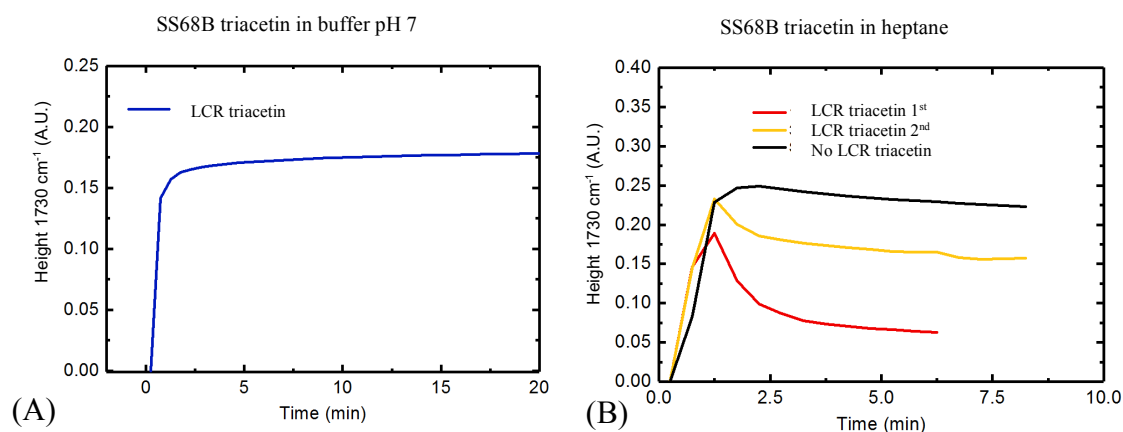


Figure 40: Film SS68B after adsorption of 0.5 mg/mL LCR: (A) application of triacetin in buffer pH 7 ($\sim 320\text{ mM}$); (B) application of triacetin in heptane ($\sim 320\text{ mM}$) two times with LCR inside the film, with red: first application and yellow: after 2nd application and black line: application of solution without LCR for blank measurement.

From **Figure 40 (A)** it is visible, that if triacetin is applied in buffer solution at pH 7 no change in the intensity of the ester band ($\sim 1730\text{ cm}^{-1}$) is recorded. If the same experiment is performed using triacetin dissolved in heptane (**Figure 40 (B)**) a decrease in absorbance of the ester band after stopping the flow ($\sim 1\text{ min}$) is obtained (see red line). Within this experiment triacetin in heptane was applied a second time after a short buffer flush, for providing essential water for the hydrolysis reaction (see **Figure 38**). Again, a decrease in peak height at $\sim 1730\text{ cm}^{-1}$ is obtained, but this time signal remains higher than for the first application (see yellow line). In addition, a measurement using the film SS68B without adsorbed LCR was performed (black line) to track eventual spectral changes arising from other effects *e.g.* diffusion of the substrate. By comparison, it can be stated, that experiments performed with LCR show higher decrease of the intensity of the ester band. Hence, enzymatic activity of LCR inside the pore with triacetin dissolved in heptane is observed.

For qualitative comparison of the activity of LCR inside the pore and on the surface, experiments were performed with LCR adsorbed on a methylated silica surface (see **Figure 41.**) The same procedure was applied as when using film SS68B.

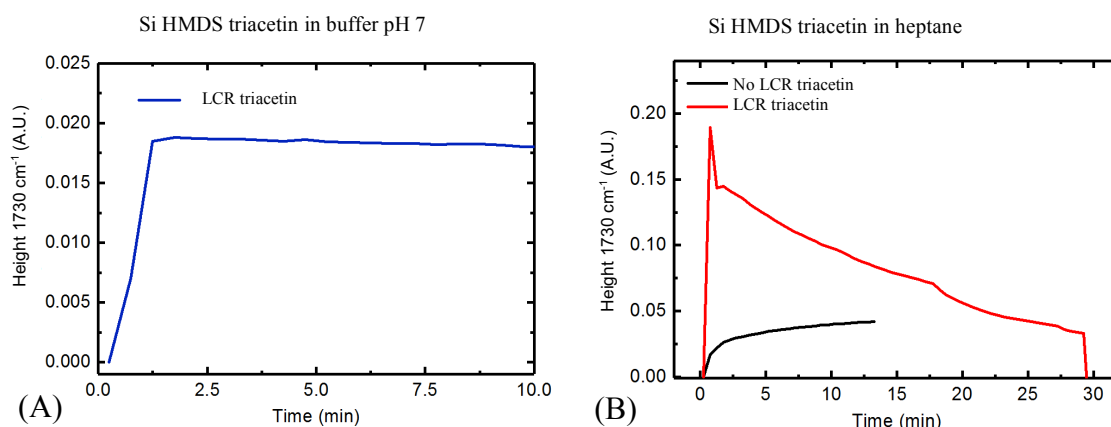


Figure 41: Si HMDS, Application of 0.5 mg/mL LCR; (A) Application of triacetin in buffer pH 7 ($\sim 320\text{ mM}$); (B) application of triacetin in heptane ($\sim 320\text{ mM}$) Red line: with LCR adsorbed on the surface. Black line: without LCR for blank measurement.

Here again a measurement without lipase on the surface was performed to exclude spectral changes due to other phenomena. Results show, that activity in heptane is higher than in buffer solution at pH 7 (compare (A) blue line with (B) red line). For performing more precise statements about the enzyme activity further experiment would be necessary. Nevertheless, results from first approaches showed, that the hydrolyzation of the ester triacetin performed by the lipase from *Candida rugosa* adsorbed inside the pores or on the surface can be investigated with my setup.

4. Conclusion

Within my thesis the interaction of the proteins Lysozyme and Lipase from *Candida rugosa* with mesoporous silica films was investigated using ATR FTIR spectroscopy. Mesoporous silica film synthesis was optimized towards large pore sizes of ~10 nm and a film thickness of ~500 nm by using an evaporation induces self-assembly (EISA) templating method. Here suitable synthesis conditions (*e.g.* sol composition, surfactant, film casting parameters) for the formation of highly ordered mesoporous silica films with ~15 nm in pore size and ~600 nm in thickness using the surfactant Pluronic F127 were determined. Coated ATR crystals were used for monitoring the adsorption of Lysozyme and Lipase out of aqueous solution. Detailed calculations enabled by my defined experimental setup allowed for differentiation if the protein is adsorbed on the outer surface or inside the film. Results obtained from experiments using Lysozyme showed that no adsorption into methylated mesopores is happening, despite the protein being smaller in size than the pores. Adsorption of Lipase of *Candida rugosa* (LCR) out of buffer pH 7 inside pores of 15 nm in size with methylated silica surface was proven. Within the highly porous coating on the ATR crystal LCR is enriched, which lead to an approximate limit of detection of 0.026 mg/mL in buffer pH 7 using FTIR spectroscopy. Throughout performed experiments detection of Lipase at low concentrations from 0.025 – 0.5 mg/mL was accomplished. Here first calibration showed linear correlation between applied concentration and obtained absorbance. Furthermore, first experiments towards the investigation of the activity of Lipase inside the pore and on methylated silica surface were performed. These showed, that the enzymatic activity using triacetin as substrate is higher using heptane as solvent than in buffer solution at pH 7.

In conclusion, throughout the successful synthesis of a stable mesoporous silica film a novel method for investigation of the interaction of proteins with mesoporous silica was developed. Thereby, differentiation between surface adsorption and protein adsorption inside the pore is possible. Furthermore, the path towards a method for investigation of proteins at very low concentration was paved. Throughout molecule specific (qualitative) as well as quantitative information enabled by IR spectroscopy, enzymatic activity under different conditions can be further analyzed.

All in all, this thesis shows a new method for investigation of the behavior of proteins towards different silica surfaces monitored by ATR FTIR spectroscopy.

5. Experimental Part

5.1 Optical Setup

Silicon ATR crystals of 10 mm x 20 mm with a thickness of $\sim 525\ \mu\text{m}$, were cut out of a double-sided Czochralski (Cz) Si wafer from our collaboration partner at IMEC/University of Gent. In our laboratory the narrow facets of the provided silicon chips were polished by hand using a custom-made sample holder with a defined angle (45° , 55°). Different diamond polishing discs with grain sizes of: $15\ \mu\text{m}$, $9\ \mu\text{m}$, $6\ \mu\text{m}$, $3\ \mu\text{m}$, $1\ \mu\text{m}$ and $0.1\ \mu\text{m}$ were used. ATR crystals were put on a sample stage and a home-built $20\ \mu\text{L}$ PMMA flow cell was mounted on top. A fluor-elastomer (FKM) O-ring with an area of $\sim 1\ \text{cm}^2$ was used to make the flow cell watertight. The transparent material of the flow cell allowed visual detection of air bubbles inside the cell. The setup was placed in the sample compartment of a Bruker Vertex 80v spectrometer equipped with a liquid nitrogen cooled mercury-cadmium-telluride (MCT) detector. Two gold mirrors directed the IR beam on the angled facets of the ATR crystal and to the detector, respectively (see **Figure 42**). IR spectra were acquired with a spectral resolution of

$4\ \text{cm}^{-1}$, a total of 64 scans (12 s, double-sided, backward forward acquisition mode) were averaged per spectrum. The rms noise was determined to be 5×10^{-4} A.U. between 2200 and $2000\ \text{cm}^{-1}$ from 64 averaged scans (4 s scan time). Spectra analysis was performed using the software package OPUS 7.5 or 8.0 (Bruker Corp., Ettlingen, Germany).

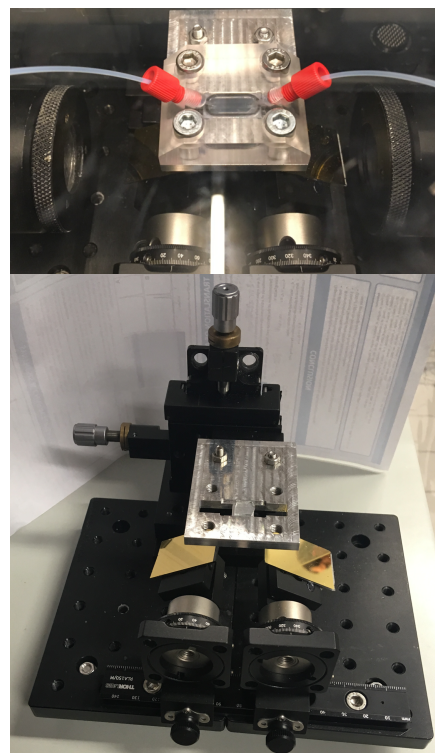


Figure 42: Picture of the home-built sample holder. Gold mirrors are directing the IR beam to the ATR crystal (not shown). The tray for the ATR crystal allows for tight sealing of the flow cell. The “clipsy”. As well as with the flow cell, with ATR crystal on the sample holder, inside the spectrometer.

5.1.1 Spectra and Data Processing

For processing of the spectra, a MatLab script was used for evaluation of the amide II band ($\sim 1550 \text{ cm}^{-1}$) as well as the ester band ($\sim 1730 \text{ cm}^{-1}$).

For processing of the amide II band, the maximum height between wavenumbers $1575 - 1490 \text{ cm}^{-1}$ was taken. For calculation of the peak height a straight baseline was formed between 1900 cm^{-1} and 1460 cm^{-1} . Background spectra were recorded while buffer flush at the beginning of the sequence. Processing of ester band of triacetin was performed by taking the maximum height between wavenumbers $1815 - 1668 \text{ cm}^{-1}$. For calculation of the peak height a straight baseline was formed between 1900 cm^{-1} and 1647 cm^{-1} . Background spectra were recorded before triacetin solution application. The time scales of the experiments were obtained since spectra were recorded every 30 seconds through the repeated spectrum measurement made in OPUS 8.0.

The concentration of protein was evaluated using BEERS Law (**Equation (12)**) for the amide II band with following parameters at 1550 cm^{-1} : $\epsilon_{\text{LCR}} = 2.799 \times 10^{-5} \text{ mL}/(\text{mg} \cdot \mu\text{m})$ determined by performed transmission measurements with optical pathlength $d = 50 \mu\text{m}$ for 1 mg/mL , $\epsilon_{\text{LYS}} = 1.611 \times 10^{-4} \text{ mL}/(\text{mg} \cdot \mu\text{m})$ ($d = 25 \mu\text{m}$ average of, 1 mg/mL , 3 mg/mL and 5 mg/mL), $d_e \cdot N = 0.317 \mu\text{m} \cdot 20 = 6.34 \mu\text{m}$ for 45° , $d_e \cdot N = 0.2379 \mu\text{m} \cdot 14 = 3.33 \mu\text{m}$ for 55° .

For the calculation of a monolayer on the surface, a close packing of equal squares of 74 % spacefill built the basis of approximations ($P = \frac{\pi}{3\sqrt{2}} = 0.74 = \frac{N \frac{4}{3} \pi r^3}{V_{\text{monolayer}}}$). Using the formula with radius of spheres: $r_{\text{LCR}} = 2.5 \text{ nm}$, $r_{\text{LYS}} = 1.5 \text{ nm}$, surface area o-ring = 1 cm^2 , height of monolayer $h = 2 \cdot r$, Volume of monolayer $\text{Vol}_{\text{mono, LCR}} = 5 \cdot 10^{14} \text{ nm}^3$ $\text{Vol}_{\text{mono, LYS}} = 3 \cdot 10^{14} \text{ nm}^3$, the amount N of the spheres filling the volume of the monolayer on the ATR crystal was calculated. With the usage of the Avogadro constant $N_A = 6.023 \cdot 10^{23} \text{ mol}^{-1}$ and the molecular weight $\text{MW}_{\text{LCR}} = 60 \text{ kDa}$, $\text{MW}_{\text{LYS}} = 60 \text{ kDa}$, the mass of proteins forming the monolayer was obtained $\text{mass}_{\text{mono, LCR}} = 0.563 \mu\text{g}$ LCR, $\text{mass}_{\text{mono, LYS}} = 0.365 \mu\text{g}$ LYS. Through the usage of the effective pathlength d_e at 1550 cm^{-1} the volume of the evanescent field can be calculated $\text{Vol}_{\text{evanfield}} = 3.17 \cdot 10^{16} \text{ nm}^3$. Therefore the concentration of the protein inside the layer can be calculated $c_{\text{mono, LCR}} = 17.76 \text{ mg/mL}$ $c_{\text{mono, LYS}} = 15.35 \text{ mg/mL}$. Hence now the concentration can be inserted in BEERS Law with already given values at 1550 cm^{-1} and the absorbance, expected from a monolayer can be evaluated $A_{\text{mono, LCR}} = 0.002 \text{ A.U.}$ (45°), $A_{\text{mono, LYS}} = 0.0082 \text{ A.U.}$ (55°). Hence, a ratio of the obtained absorbance and the theoretical absorbance from a monolayer can be formed.

For calculation of the limit of detection (LOD) signal to noise ratio calculated between 2000 – 2200 cm^{-1} was taken 5×10^{-4} A.U. LOD is 3 times S/N ratio, hence concentration which would give this signal was calculated. $\text{LOD} = (0.0015 \text{ A.U.} / A_{\text{measured}} (\text{Signal from } 0.5 \text{ mg/mL LCR}) * 0.5 \text{ mg/mL LCR}$.

5.2 Materials and Methods

5.2.1 Chemicals

Tetraethoxysilane (TEOS, Sigma-Aldrich, 99.5%), absolute ethanol (Fisher, 99.6%), hydrochloric acid (VWR, 37%), hexamethyldisilazane (HMDS, TCI Chemicals, >96.0%), Absolute acetone (Sigma-Aldrich, >99.9%, sealed), Pluronic® F127, (PEO₁₀₆-PPO₇₀-PEO₁₀₆ Sigma-Aldrich, powder), cetyltrimethylammonium bromide (CTAB, Sigma-Aldrich, 99%), were used as received. Silicon wafers were cut with a glass dicer into 2 cm x 1 cm chips and used as substrate for synthesis. Lipase from *Candida rugosa* (Sigma-Aldrich, Type VII, ≥ 700 unit/mg solid, Triacylglycerol lipase), Lysozyme from hen egg white (Fluka, 76344 U/mg, Muramidase), Triacetin (Glyceryl Triacetat, Sigma-Aldrich $\geq 99\%$) Buffer preparation: Potassiumdihydrogenphosphat (KH_2PO_4) was dissolved in aqua dest. to a concentration of 16.5 mM (2.16 g/L, pH~5.6). Using a pH electrode, the pH was adjusted with NaOH solution to pH 7 and diluted HCl solution to pH 3.

5.2.2 Spin coating and Dip coating

For film casting by spin coating a spin coater equipped with a little box for providing a surrounding with constant humidity during spinning (see **Figure 43**, right picture) was used. Relative



humidity was adjusted using a gas flow adjuster with a dry air and a wet air flow. Humidity was checked in the box before spinning. For spin coating the beforehand cut silicon wafers were inserted onto the home printed sample holder, the lid was closed, spinning with constant speed (e.g. 2000 rpm) was started. Subsequently, 50 μL of the sol solution were deposited on top of the rotating substrate. After 30 seconds rotating in the

Figure 43: left/middle picture: home-built Dip-Coater, “Dippert 3000” right picture: Spin coater equipped with a plastic box

Figure 43: left/middle picture: home-built Dip-Coater, “Dippert 3000” right picture: Spin coater equipped with a plastic box

chamber films were differently treated as *e.g.* immediate heat treatment at 110°C or aging of the film under controlled humidity at room temperature (RT).

Dip coating was performed with a home-built dip-coater, shown in **Figure 43** (left and middle picture). Here the sol was put into a box with controlled humidity and dipping speed was adjusted. Film treatment after film deposition was similar to those casted by spin coating.

5.2.3 Characterization of Mesoporous Silica Films

Low-angle X-ray diffraction data were recorded with an Empyrean PANalytical multipurpose diffractometer in Bragg-Brentano geometry operation with a Cu anode at 45 kV and 40 mA ($\lambda = 1.54 \text{ \AA}$). Divergent slit of $1/8^\circ$, a 10 mm mask, soller slit of 0.04° and an anti-scatter slit of $1/2^\circ$ and a GalliPix detector were used. Samples were placed on the silicon single crystal sample holder, which was rotated during measurements at a rate of 4 s/turn. The diffraction patterns were recorded at room temperature between 0.1° and 6° (2θ) at a rate of 100 s/step and a step size of 0.01° . Film thickness was determined *via* a Bruker Dektak XTL Stylus profilometer by measuring a scratch on the film.

For the film SS63B the pore size was determined by ellipsometric porosimetry as well as using a similar approach using our ATR setup (established by Bettina). Thereby air with different relative humidity was applied to the film. The resulting absorbance of water ($\sim 3400 \text{ cm}^{-1}$) was used for determination of the adsorbed amount of water inside the pores giving an adsorption and desorption plot similar to those obtained from N_2 adsorption measurements. The pore size distribution (PSD) obtained from the adsorption branch gives the actual pore diameter, while the PSD of the desorption branch gives information on the interconnection sizes. Both applied methods result in a size of 7-8 nm for interconnections and 12-15 nm for the actual pore diameter of the film SS63B (see **Figure 44**).

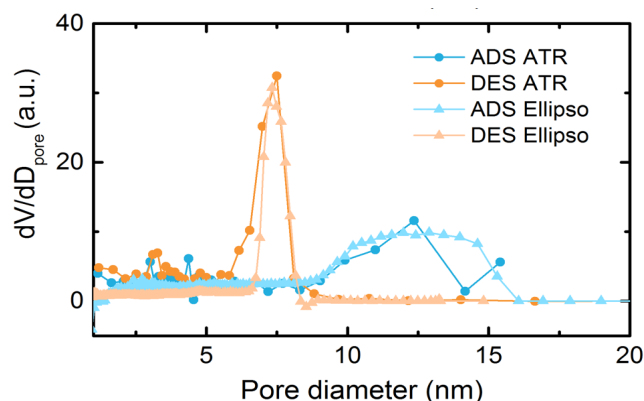


Figure 44: Pore size distribution of sample SS63B determined by ellipsometric porosimetry (Ellipso) and our ATR setup. (ATR). ADS: Adsorption, DES: desorption curves. dV/dD_{pore} differential pore volume distribution.

5.3 Synthesis of the Mesoporous Silica Films

All produced samples were chronologically numbered *e.g.* SS01Bx. Whereas SS stands for Sophia Steinbacher, the letters behind the number represent the used surfactant (B for F127, C for CTAB). For samples synthesized by dip coating a “d” stands after SS *e.g.* SSd01Bx. Occurring small letters at the end of the number symbolize the heat treatment after deposition: (x) no treatment storage at RT, (y) heat treatment at 80°C / 110°C / 150°C and (z) calcination at 400°C for 4 h.

For samples using F127 the volume fraction of surfactant is calculated according to Holmqvist *et. al* [25]. Here the total volume fraction of the polymer ϕ_{pol} is calculated by dividing the volume of the polymer V_{pol} by the volume of SiO_2 $V_{inorganic}$

5.3.1 Synthesis of Silica Films Using CTAB as Surfactant

For the synthesis of mesoporous silica films using CTAB as surfactant the sol was prepared by 2.2 mL of ethanol 2.08 g of TEOS and 0.9 mL of 0.056 molar HCl which were inserted respectively in a round-necked flask and refluxed at 40°C for 3 h. For 3D hexagonal structures 0.041 g (0.12 equivalent) CTAB and for cubic structures 0.054 g (0.16 equivalent) CTAB were dissolved in 1 mL of ethanol followed by the addition of 0.5 mL of the beforehand prepared sol. The solution was stirred for 5 minutes and immediately used for spin coating. The resulting final molar ratio were 1:13:5:5x10⁻³:0.12-0.16 for TEOS:EtOH:H₂O:HCl:CTAB.

Spinning conditions were: spinning speed of 2000 rpm, 50% relative humidity for 3D hexagonal and 2000 rpm, 65% RH for the cubic structures. Prior to deposition, the ATR crystals were cleaned using the ultrasonification bath (chips immersed in ethanol) and dried with an air flow. Subsequently after sol deposition by spin coating, the samples were put in the oven at 110° over night (o/n). For the ATR crystal C01b (3D hexagonal structure) the template CTAB was removed by solvent extraction with reflux in acetone for 6 h and subsequent drying in the oven (110°C, o/n).

5.3.2 Synthesis of Silica Films Using F127 as Surfactant

5.3.2.1 Synthesis Using Spin Coating for EISA

Samples: SS01B – SS08B and SS34B – SS42B

First synthesis of mesoporous films using F127 as surfactant and was performed according to Dunphy *et al.* [24].

5.3.2 Synthesis of Silica Films Using F127 as Surfactant

Here the synthesis route using 45.4 mg F127 per mmol SiO₂ was reproduced, but different relative humidity in the chamber during spin coating (20 %, 40 %, 60 % and 80 %) as well as different spinning speeds (2000 rpm / 3000 rpm) were applied.

Table 7: Sol composition for the Synthesis of samples SS01B - SS08B (16.4.18) as well for samples SS34B - SS42B (4.6.18)

SS01B - SS08B; SS34B - SS42B					
16.4.18 & 4.6.18					
45.4 mg F127/mmol SiO ₂					
	TEOS	F127	EtOH	HCl (0.056 M)	H ₂ O
molar ratio	1	0.0036	18.67	0.0145	16.13
mmol	0.55	0.0019	10.28	0.008	8.88
mg	114.7	25	473.6	0.143	0.017
mL	0.122		0.6		0.017
$\phi_{\text{pol}} = 40.02 \%$					

For the sol synthesis 25 mg of F127 was dissolved in 0.6 mL of ethanol, 0.1428 mL of 0.056 M HCl and 0.01715 mL water (see **Table 7**). After dissolution of the polymer 0.122 mL TEOS are added as well as the solution was shortly shaken. After 10 min of aging (just storing solution at RT, no stirring) the sol was used for spin-coating.

All obtained X-ray diffraction patterns did not show defined reflexes, hence no highly ordered mesoporous structures were obtained.

Samples: SS09B – SS33B and SS44B – SS49B

Principle synthesis from Dunphy *et al.* [24] was maintained, but the content of F127 was altered. For the sol synthesis F127 was dissolved in ethanol, with subsequent addition of 0.056 M HCl and TEOS (for amount of chemicals see **Table 8**). The solution was shortly shaken and stored for 10 min (aging) before spin coating.

Spin coating conditions:

SS09B-12B: Sol 1: RH 45% 500 rpm, 1000 rpm, 15000 rpm and 2000 rpm

SS13B-16B: Sol 2: RH 45% 500 rpm, 1000 rpm, 15000 rpm and 2000 rpm

SS17B-20B: Sol 1: RH 65% 500 rpm, 1000 rpm, 15000 rpm and 2000 rpm

SS21B-24B: Sol 2: RH 65% 500 rpm, 1000 rpm, 15000 rpm and 2000 rpm

SS25B-28B: Sol 3: RH 45% 500 rpm, 1000 rpm, 15000 rpm and 2000 rpm

SS44B – SS46B: 2000 rpm Sol 1 20% RH, 40% RH, 60% RH

SS47B – SS49B: 2000 rpm Sol 2 20% RH, 40% RH, 60% RH

All films were calcined at 350°C with no prior heat treatment.

Table 8: Sol composition for samples SS09B - SS33B (~45.4 mg F127/mmol SiO₂) synthesized 26.04.18 and SS44B – SS49B (45.4 or 118 mg F127/mmol SiO₂) synthesized 8.10.2018.

SS09B - SS33B,					
	TEOS	F127	EtOH	HCl	H ₂ O
26.04.2018					
Sol 1 (SS09B - SS12B, SS17B – SS20B)					
molar ratio	1	0.0039	18.67	0.0145	16.13
mmol	0.55	0.0021	10.28	0.008	8.88
g	0.115	0.027	0.47	0.05 M	0.16
mL	0.122		0.60	0.143	0.16
$\phi_{\text{pol}} = 41.6 \%$					
Sol 2 (SS13B - SS16B, SS21B – SS24B)					
molar ratio	1	0.006	18.67	0.0145	16.13
mmol	0.55	0.0033	10.28	0.0088	8.88
g	0.115	0.042	0.47	0.05 M	0.16
mL	0.122		0.60	0.143	0.16
$\phi_{\text{pol}} = 52.36 \%$					
Sol 3 (SS25B – SS33B)					
molar ratio	1	0.0042	18.67	0.0145	16.13
mmol	0.55	0.0023	10.28	0.008	8.88
g	0.115	0.029	0.47	0.05 M	0.16
mL	0.122		0.60	0.143	0.16
$\phi_{\text{pol}} = 43.2 \%$					

SS44B – SS49B					
	TEOS	F127	EtOH	HCl	H ₂ O
08.10.2018					
45.4 mg F127/mmol SiO ₂ : SS44B – SS46B					
molar ratio	1	0.0036	18.67	0.0145	16.13
mmol	0.55	0.002	10.28	0.008	8.88
g	0.115	0.025	473.6	0.05 M	16
mL	0.122		0.6	0.143	0.16
$\phi_{\text{pol}} = 40.02 \%$					
118 mg F127/mmol SiO ₂ : SS47B – SS49B					
molar ratio	1	0.0094	18.67	0.0145	16.13
mmol	0.55	0.005	10.28	0.008	8.88
g	0.115	0.065	473.6	0.05 M	16
mL	0.122		0.6	0.143	0.16
$\phi_{\text{pol}} = 63 \%$					

For samples SS09B – SS33B all obtained X-ray diffraction patterns did not show defined reflexes hence no highly ordered mesoporous structure was obtained.

The obtained by X-ray diffraction patterns of samples SS44B-SS49B, which were showing reflections are given in **Figure 45**.

Exemplary thickness after calcination was for 45.4 mg F127 per mmol SiO₂ (Sol 1): SS44Bz = 237 nm and 118 mg F127 per mmol TEOS (sol 2): SS48B = 420 nm.

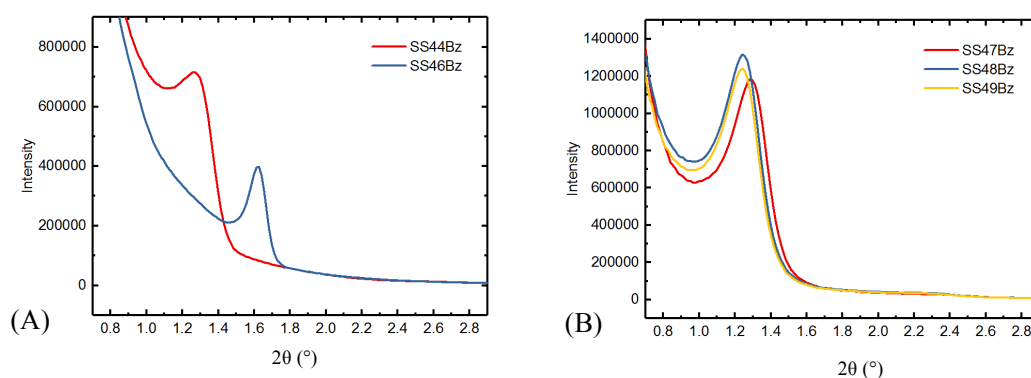


Figure 45: Diffraction pattern of the samples spin coated at 2000 rpm SS44Bz (Sol 1, 20% RH), SS46Bz (Sol 1, 60% RH), SS47Bz (Sol 2, 20% RH), SS48Bz (Sol 2, 40% RH), SS49Bz (Sol 2, 60% RH) for sol compositions see Table 8.

5.3.2 Synthesis of Silica Films Using F127 as Surfactant

Samples: SS50B-SS58B

For the synthesis of the sol, EtOH, TEOS and HCl (0.01 M) were stirred for 20 min at room temperature. Polymer solution was prepared by stirring F127, EtOH, HCl (0.01 M) and H₂O for 10 min. Exact amounts and ratios for the sol and the polymer solution (Pol) are given in **Table 9**. Solutions were combined and slightly stirred for 3 h at RT before spin coating.

Table 9: Sol compositions for the synthesis of the samples SS50B-SS58B spin coated at 2000 rpm, 20 % RH, 40% RH, 60% RH respectively for 0.0029 F127/TEOS, SS50B-SS52B, 0.0037 F127/TEOS, SS53B-SS55B 0.0096 F127/TEOS, SS56B-SS58B;

08.10.2018										
SS "Sol1" altered BB										
	TEOS		F127		EtOH		HCl		H ₂ O	
	Sol	Pol	Sol	Pol	Sol	Pol	Sol	Pol	Sol	Pol
0.0029 F127/TEOS, SS50B-SS52B										
Σ mol ratio	1		0.0029		0.0160		0.0152		16.28	
molar ratio	1	0	0	0.0029	0.009	0.007	0.0108	0.0044	6.00	10.28
mmol	6.24	0	0	0.0184	0.054	0.046	0.068	0.027	37.46	64.15
g	1.3	0	0	0.232	2.5	2.1	0.1 M	0.1 M	0.1 M	1.156
mL	1.38	0			3.17	2.66	0.675	0.272	0.675	0.884
φ _{pol} = 35 %										
0.0037 F127/TEOS, SS53B-SS55B										
Σ mol ratio	1		0.0037		0.0160		0.0152		16.28	
molar ratio	1	0	0	0.0037	0.009	0.007	0.0108	0.0044	6.00	10.28
mmol	6.24	0	0	0.0228	0.054	0.046	0.068	0.027	37.46	64.15
g	1.3	0	0	0.287	2.5	2.1	0.1 M	0.1 M	0.1 M	1.156
mL	1.38	0			3.17	2.66	0.675	0.272	0.675	0.884
φ _{pol} = 40.02 %										
0.0096 F127/TEOS, SS56B-SS58B										
Σ mol ratio	1		0.0096		0.0160		0.0152		16.28	
molar ratio	1	0	0	0.0096	0.009	0.007	0.0108	0.0044	6.00	10.28
mmol	6.24	0	0	0.0598	0.054	0.046	0.068	0.027	37.46	64.15
g	1.3	0	0	0.754	2.5	2.1	0.1 M	0.1 M	0.1 M	1.156
mL	1.38	0			3.17	2.66	0.675	0.272	0.675	0.884
φ _{pol} = 63.66 %										

Spin coating was performed at 2000 rpm, 20 % RH, 40% RH, 60% RH respectively for 0.0029 F127/TEOS, SS50B-SS52B, 0.0037 F127/TEOS, SS53B-SS55B 0.0096 F127/TEOS, SS56B-SS58B.

The resulting diffraction patterns using the sol compositions given in **Table 9** are shown in **Figure 46**.

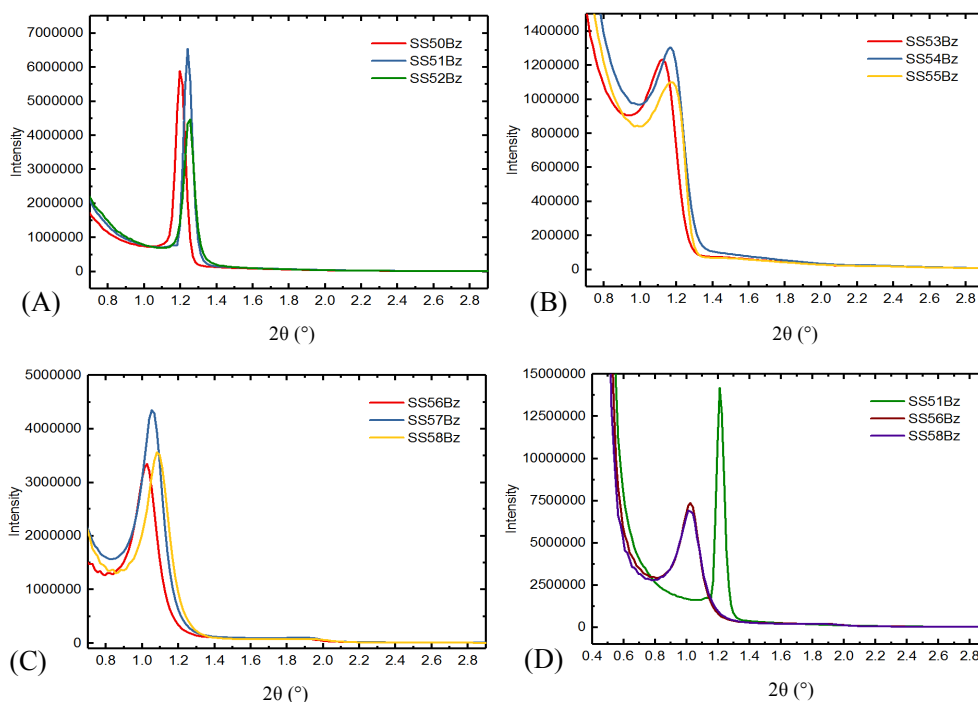


Figure 46: Diffraction pattern of (A) Samples SS50Bz-SS52Bz 0.0029 F127/TEOS, SS53Bz-SS55Bz 0.0037 F127/TEOS, SS56Bz-SS58Bz 0.0096 F127/TEOS, all films coated at 2000 rpm and for each sol, 20%, 40% and 60% RH respectively. (D) Comparison of Samples SS51B, SS56B and SS58B.

Within the novel sol formation, different diffraction patterns depending on the concentration of the pluronic F127 can be obtained. Relative humidity during spin coating from 20-60% was not influencing the formation of the mesoporous structure. Thickness was measured for a molar ratio of 0.0029 F127/TEOS: SS51Bz = 246 nm, 0.0037 F127/TEOS: SS55Bz = 270 nm and 0.0096 F127/TEOS: SS56B = 618 nm.

Samples: SS59B-SS61B

For the synthesis sol solution was constituted of ethanol, TEOS, 0.1 M HCl and stirred for 20 min at RT. Polymer solution was composed of F127, ethanol, H₂O and 0.1 M HCl and stirred until the polymer was dissolved. After 20 min solutions were combined and stirred for 3 h at RT before use for spin coating. For exact amount of chemicals, see **Table 10**.

For the following synthesis of the samples SS59B, SS60B, SS61B the amount of F127 was further increased, whereas samples x no heat treatment, y: 80° 6 h and z after calcination at 350°C 4 h were investigated by X-ray diffraction (see **Table 10** for Sol, **Figure 47** for corresponding X-ray diffraction patterns).

5.3.2 Synthesis of Silica Films Using F127 as Surfactant

Table 10: Sol compositions for the synthesis of the samples at 2000 rpm,, 40% RH, respectively for 0.0094 F127/TEOS, SS59B, 0.01175 F127/TEOS, SS60B, 0.0141 F127/TEOS, SS61B

22.10.2018										
	TEOS		F127		EtOH		HCl		H ₂ O	
	Sol	Pol	Sol	Pol	Sol	Pol	Sol	Pol	Sol	Pol
0.0094 F127/TEOS, SS59Bx, y, z										
Σ mol ratio	1		0.0094		0.0160		0.0152		16.28	
molar ratio	1	0	0	0.0094	0.009	0.007	0.0108	0.0044	6.00	10.28
mmol	6.24	0	0	0.0587	0.054	0.046	0.068	0.027	37.46	64.15
g	1.3	0	0	0.739	2.5	2.1	0.1 M	0.1 M	0.1 M	1.16
mL	1.38	0			3.17	2.66	0.675	0.272	0.675	0.88
φpol = 63.21 %										
0.01175 F127/TEOS SS60Bx, y, z										
Σ mol ratio	1		0.0118		0.0160		0.0152		16.28	
molar ratio	1	0	0	0.0118	0.009	0.007	0.0108	0.0044	6.00	10.28
mmol	6.24	0	0	0.0733	0.054	0.046	0.068	0.027	37.46	64.15
g	1.3	0	0	0.924	2.5	2.1	0.1 M	0.1 M	0.1 M	1.16
mL	1.38	0			3.17	2.66	0.675	0.272	0.675	0.88
φpol = 68.23 %										
0.0141 F127/TEOS SS61Bx, y, z										
Σ mol ratio	1		0.0141		0.0160		0.0152		16.28	
molar ratio	1	0	0	0.0141	0.009	0.007	0.0108	0.0044	6.00	10.28
mmol	6.24	0	0	0.0880	0.054	0.046	0.068	0.027	37.46	64.15
g	1.3	0	0	1.109	2.5	2.1	0.1 M	0.1 M	0.1 M	1.16
mL	1.38	0			3.17	2.66	0.675	0.272	0.675	0.88
φpol = 72.04 %										

Spin coating was performed at 2000 rpm and 40% RH with x... no heat treatment, y_z... 80° for 6 h and 350°C for 4 h, z... no pre heat treatment and calcination at 350°C 4 h The resulting diffraction patterns using the sol compositions given in **Figure 47**.

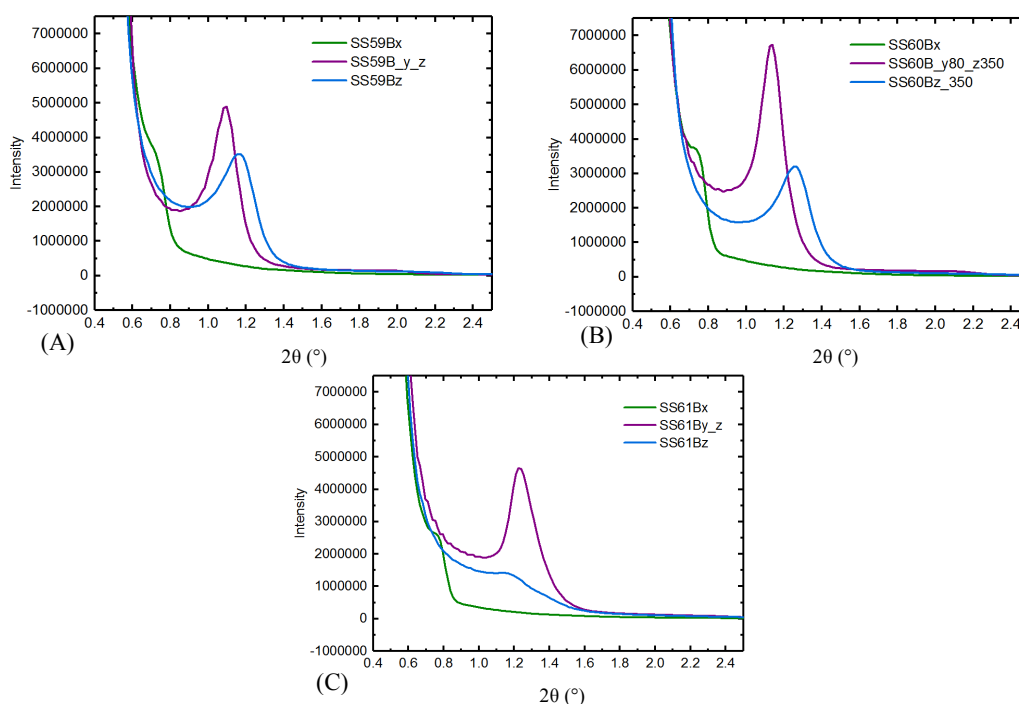


Figure 47: X-ray diffraction patterns of the samples with: x ... no heat treatment, y_z... 6 h 80°C and 4 h 350°C and z ... 350°C: (A) SS59B 0.0094 F127/TEOS, (B) SS60B 0.01175 F127/TEOS and (C) SS61B 0.0141 F127/TEOS.

Exemplary thickness was measured for a molar ratio of 0.0096 F127/TEOS: SS59Bz = 590 nm, 0.01175 F127/TEOS: SS60Bz = 420 nm and 0.0141 F127/TEOS: SS61Bz = 750 nm.

Hence, a suitable sol composition for the coating of ATR crystals was found with 0.0094 F127/TEOS (given in **Table 11**). Film synthesis is performed by stirring for 20 min at RT for sol formation without template, 3 h aging of solution containing template for formation of the final sol. Subsequent spin coating at 40% RH, 2000 rpm and heat treatment 110° immediately after synthesis for 4 – 12 h and calcination at 400°C for 4 h lead to highly ordered porous silica films with high pore sizes.

Table 11: Sol composition for the formation of the ATR crystal SS63B and SS68B

ATR crystals: SS63B, SS68B, SS69B										
20.11.18, 10.12.18, 29.1.19										
	TEOS		F127		EtOH		HCl		H ₂ O	
	Sol	Pol	Sol	Pol	Sol	Pol	Sol	Pol	Sol	Pol
0.0094 F127/TEOS										
Σ mol ratio	1		0.0096		0.0160		0.0152		16.28	
molar ratio	1	0	0	0.0096	0.009	0.007	0.0108	0.0044	6.00	10.28
mmol	6.24	0	0	0.06	0.054	0.046	0.068	0.027	37.46	4.15
g	1.3	0	0	0.754	2.5	2.1	0.1 M	0.1 M	0.1 M	1.16
mL	1.38	0			3.17	2.66	0.675	0.272	0.68	0.88
φ _{pol} = 63.66 %										

5.3.2 Synthesis of Silica Films Using F127 as Surfactant

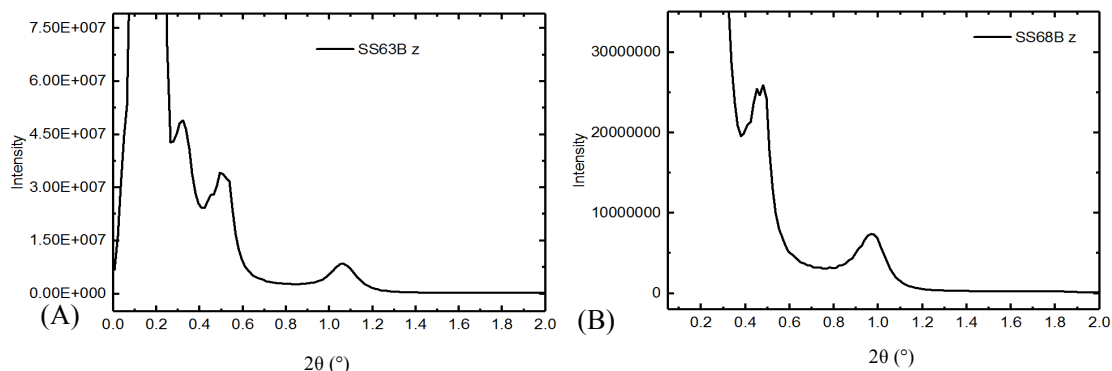


Figure 48: X-ray diffraction patterns of the ATR coatings SS63Bz and SS68Bz.

The so performed synthesis of mesoporous silica films leads to the formation of ~15 nm pores with 8 nm bottle necks. The resulting layer thickness was 600 nm for SS63Bz and 625 nm for SS68Bz whereas X-ray diffraction pattern are given in **Figure 48**.

Further experiments were performed, using the final sol composition for a co-condensation approach towards methylated silica surfaces. Here different amounts of TEOS were replaced by MTES. Specific sol compositions for the synthesis are given in **Table 12**.

Table 12: Sol compositions for the synthesis of the samples SS65B-SS67B for functionalization by co-condensation. Film processing at 2000 rpm, 40% RH,

Co-Condensation TEOS MTES – SS65B – SS67B												
05.12.2018												
	TEOS		MTES		F127		EtOH		HCl		H ₂ O	
	Sol	Pol	Sol	Pol	Sol	Pol	Sol	Pol	Sol	Pol	Sol	Pol
0.0094 F127 : TEOS + MTES 15% - SS65B												
Σ mol ratio	0.85		0.15		0.0096		0.0160		0.0152		16.28	
molar ratio	0.85	0	0.15	0	0	0.0096	0.009	0.007	0.0108	0.0044	6.00	10.28
mmol	5.30	0	0.94	0	0	0.06	0.054	0.046	0.068	0.027	37.46	64.15
g	1.1	0	0.167	0	0	0.754	2.5	2.1	0.1 M	0.1 M	0.1 M	1.156
mL	1.18	0	0.18	0			3.17	2.66	0.675	0.272	0.675	0.884
φ _{pol} = 67 %												
0.0094 F127 : TEOS + MTES 30% - SS66B												
Σ mol ratio	0.7		0.3		0.0096		0.0160		0.0152		16.28	
molar ratio	0.7	0	0.3	0	0	0.0096	0.009	0.007	0.0108	0.0044	6.00	10.28
mmol	4.37	0	1.87	0	0	0.06	0.054	0.046	0.068	0.027	37.46	64.15
g	0.91	0	0.334	0	0	0.754	2.5	2.1	0.1 M	0.1 M	0.1 M	1.156
mL	0.97	0	0.36	0			3.17	2.66	0.675	0.272	0.675	0.884
φ _{pol} = 67 %												

0.0094 F127 : TEOS + MTES 40% - SS67B													
Σ mol ratio	0.6		0.4		0.0096		0.0160		0.0152		16.28		
molar ratio	0.6	0	0.4	0	0	0.0096	0.009	0.007	0.0108	0.0044	6.00	10.28	
mmol	3.74	0	2.50	0	0	0.06	0.054	0.046	0.068	0.027	37.46	64.15	
g	0.78	0	0.445	0	0	0.754	2.5	2.1	0.1 M	0.1 M	0.1 M	1.156	
mL	0.83	0	0.47	0			3.17	2.66	0.675	0.272	0.675	0.884	
φpol = 67 %													

Film synthesis was performed as for samples SS63B and SS68B. The resulting diffraction patterns of the silica films synthesized by co-condensation are given in **Figure 49**.

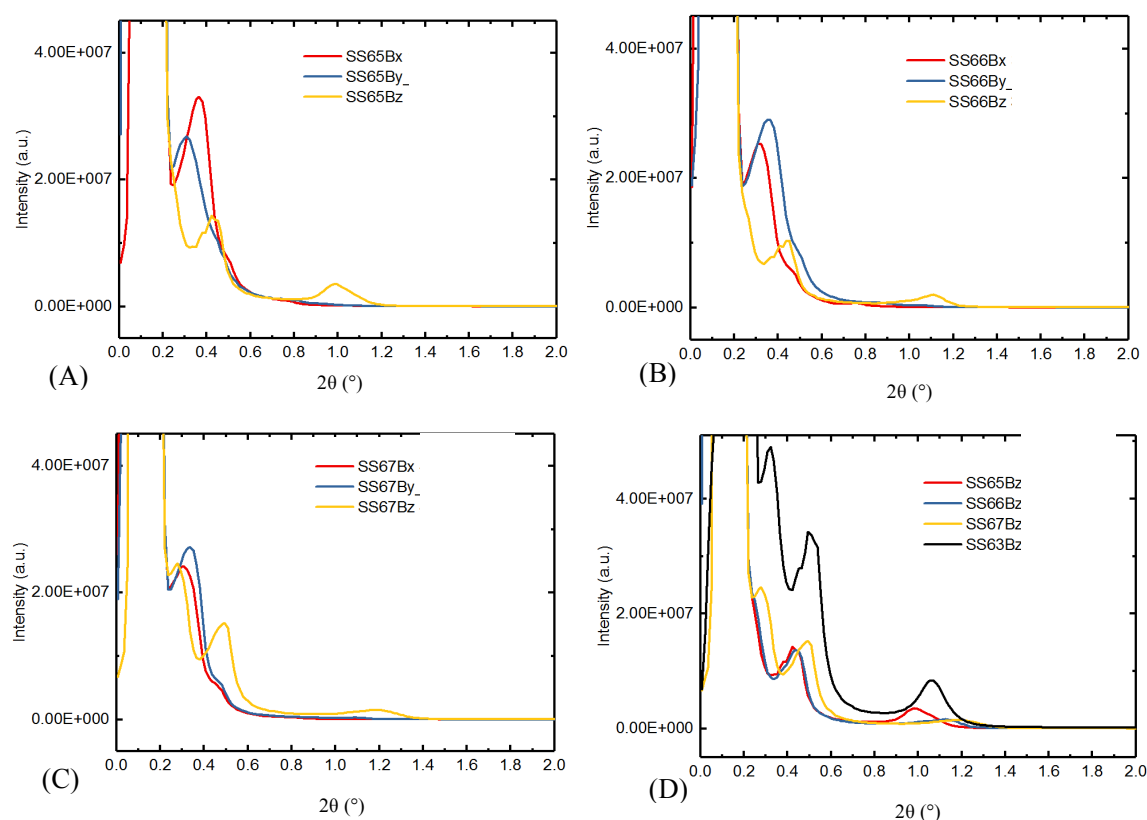


Figure 49 X-ray diffraction patterns of the mesoporous silica films synthesized by co-condensation: For exact sol composition see Table 12: x...storage at RT, y... heat treatment at 110°C 6 h, z... heat treatment at 110°C 6 and 400°C 4 h (A) SS65B 15% MTES (B) SS66B 30 % MTES, (C) SS67B 40% MTES and (D) comparison of the different amount of MTES whereas for SS63B no MTES was used.

The layers synthesized by co condensation (SS65Bz-SS67Bz), were used for investigation of the stability of the layers in buffer solution (**section 3.2.3**).

5.3.2 Synthesis of Silica Films Using F127 as Surfactant

5.3.2.2 Synthesis using Dip Coating for EISA

Samples: SSd01B – SSd20B

For the synthesis of the sol for dip coating of films 10 mL of EtOH and TEOS and HCl were stirred for 20 min at room temperature. Polymer solution was prepared by dissolving F127 in remaining EtOH (see **Table 13** for exact amounts of chemicals). Solutions were combined and slightly stirred for 3 h at RT.

Table 13: Sol composition for the synthesis of mesoporous silica films using F127 and dip coating as deposition method. SSd01B - SSd09B (20.06.2018), SSd10B - SSd20B, (25.06.2018)

Dip Coating - F127					
	TEOS	F127	EtOH	HCl	H ₂ O
20.06.2018, SSd01B - SSd09B- Sol 1					
molar ratio	1	0.01	8.65	0.00108	6.00
mmol	24.96	0.21	215.87	0.027	149.83
g	5.2	2.59	9.95		2.7
mL	5.53		12.6	0.01 M	2.7
Φ pol = 60.23 %					
	TEOS	F127	EtOH	HCl (0.01 M)	H ₂ O (0.01 M)
25.06.2018, SSd10B - SSd20B – Sol 2					
molar ratio	1	0.008	12.1	0.001	6.00
mmol	24.96	0.205	301.5	0.027	149.83
g	5.2	2.585	13.9		2.7
mL	5.53		17.6	0.01 M	2.7
Φ pol = 60.23 %					

For samples SSd01B-SSd09B, dip withdrawal was 1 mm/s, 30%, 50% and 70% RH with 1, 5, 10 min after dipping at controlled RH in humidity chamber respectively (e.g. SSd01B, 30% RH, 1 min; SSd02B 30% RH, 5 min *etc.*). Thickness was measured exemplarily for sample SSd01Bz = 716 nm, SSd02Bz = 841 nm and SSd03Bz = 960 nm. For SSd10B-SSd20B the ethanol concentration was varied, whereas dip coating was performed at 30% RH with variation of withdrawal speed 0.5-2 mm/s and 1/5 min at controlled RH after deposition.

For both synthesis the obtained by X-ray diffraction patterns showing reflexes are given in **Figure 50**.

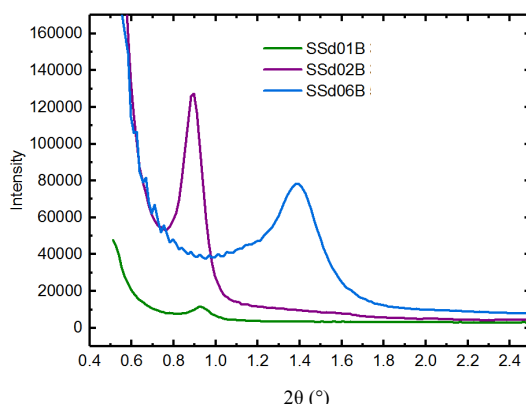


Figure 50: X-ray diffraction patterns of samples using sol compositions from Table 13: SSd01B: (Sol 1, 3 h age, 1 mm/s, 1 min, 30% RH), SSd02B: (Sol 1, 3 h age, 1 mm/s, 5 min, 30% RH), SSd06B: (Sol 1, 3 h age, 1 mm/s, 10 min, 50% RH)

Samples: SSd21B – SSd30B:

For the synthesis of the sol 10 mL of EtOH and TEOS and HCl were stirred for 20 min at room temperature. Polymer solution was prepared by dissolution of F127 in EtOH (see **Table 14** for exact amounts of chemicals). Solutions were combined and slightly stirred for 3 h (Samples: 21, 22, 25, 26), or 4.5 h (Samples: 23, 24) or 20 h (Samples: 27, 28, 29, 30) at RT for final sol formation.

Table 14: Sol composition for the synthesis of mesoporous silica films using F127 and dip coating as deposition method. SSd21B – SSd30B (4.7.2018),

Dip Coating - F127, 4.7.2018					
	TEOS	F127	EtOH	HCl	H ₂ O
Sol 1, SSd21B-24Bxyz, 27B, 29B					
molar ratio	1	0.003	16	0.001	6.07
mmol	24.99	0.074	399.7	0.027	151.66
g	5.21	0.927	18.41	2.733	2.733
mL	5.54		12.6	0.0093 M	2.733
Φ pol = 12.17 %					
	TEOS	F127	EtOH	HCl (0.69 M)	H ₂ O
Sol 2, SSd25B-26Bxyz, 28B-30B					
molar ratio	1	0.00054	3	0.0002	0.96
mmol	208.72	0.1123	625.1	0.0360	199.8
g	5.215	1.415	28.80	3.6	3.6
mL				0.69 M	
Φ pol = 9.16 %					

Samples were dip coated at 30 % RH, 2.5 min at controlled RH (30%) after deposition and withdrawal speed of 0.15 mm/s (for Samples: 22, 24, 26) or 1 mm/s (for all other). Post deposition heat treatment: x...RT, y...80°C, 12 h, z...400°C, 4 h; Exemplary thickness of samples are: Sol 1: SSd23: x =246 nm; y = 204 nm; z = 147 nm; Sol 2: SSd25: x =210 nm;

5.3.2 Synthesis of Silica Films Using F127 as Surfactant

y = 142 nm; z = 121 nm; All synthesized samples showing reflexes in the X-ray diffraction patterns using sol compositions in **Table 14** and final calcination at 400°C 4 h are given in **Figure 51**. For samples y_z heat treatment at 80° and calcination 400°C h 4. For samples z (x_z) storage at RT until calcination at 400° 4h.

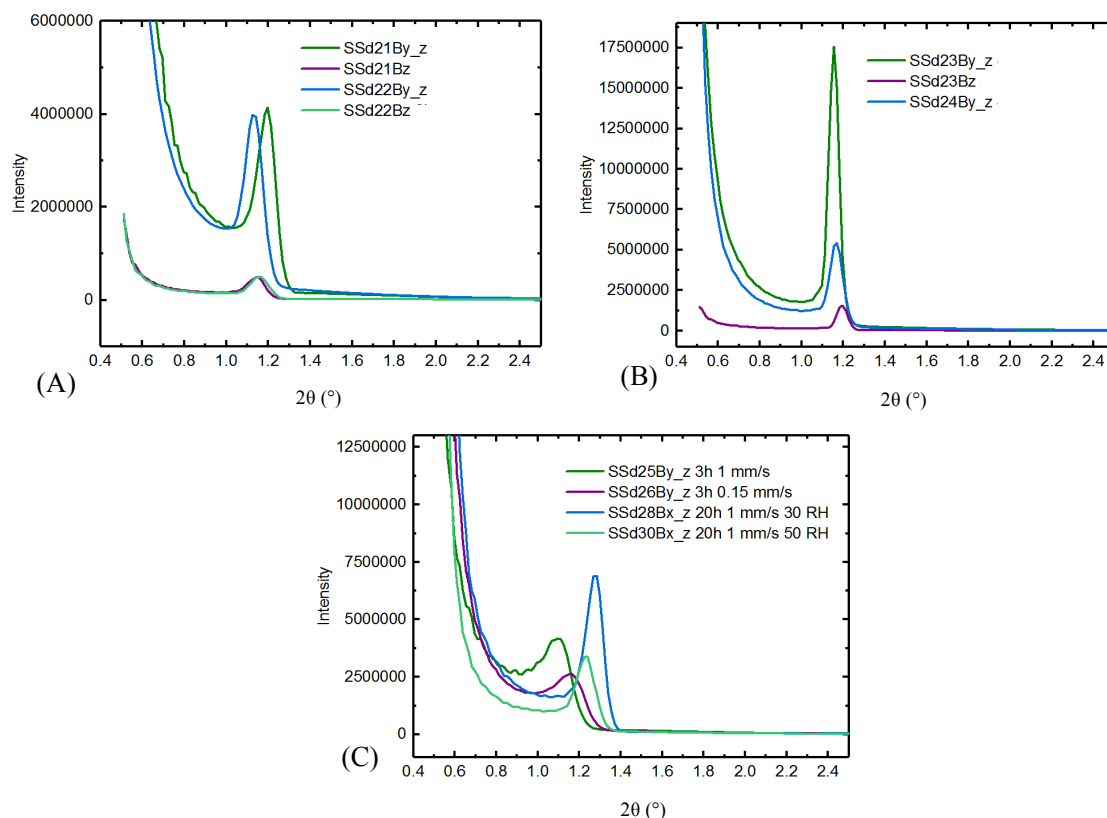


*Figure 51: X-ray diffraction patterns of samples using sol compositions from **Table 14**: (A) SSd21B: (Sol 1, 3 h age, 0.15 mm/s, 2.5 min, 30% RH) SSd22B: (Sol 1, 3 h age, 0.15 mm/s, 2.5 min, 30% RH); (B): SSd23B: (Sol 1, 4.5 h age, 0.15 mm/s, 2.5 min, 30% RH) SSd24B: (Sol 1, 4.5 h age, 0.15 mm/s, 2.5 min, 30% RH); (C): SSd25B: (Sol 2, 3 h age, 1 mm/s, 30% RH, 2.5 min); SSd26B: (Sol 2, 3 h age, 0.15 mm/s, 2.5 min, 30% RH); SSd28B: (Sol 2, 20 h age, 1 mm/s, 2.5 min, 30% RH); SSd30B: (Sol 2, 20 h age, 1 mm/s, 2.5 min, 50% RH);*

Most defined reflex was obtained for sample SSd23B_z using sol 1, 3 h at RT for sol formation, dip coating at 30% RH with 1 mm/s withdrawal speed, 2.5 min at controlled humidity of 30% RH after deposition, subsequent heat treatment for 12 h at 80°C and 4 h at 400°C.

Samples: SSd31B – SSd36B

For the synthesis of the sol 10 mL of EtOH and TEOS and HCl were stirred for 20 min at room temperature. Polymer solution was prepared by dissolving F127 in EtOH (see **Table 15**). Solutions were combined and slightly stirred for 3 h (Samples: 31, 32, 33, 34), or 4 h (Samples: 34, 35).

Table 15: Sol composition for the synthesis of mesoporous silica films using F127 and dip coating as deposition method. SSd31B – SSd36B (6.7.2018),

SSd31B-SSd36B , 6.7.2018					
	TEOS	F127	EtOH	HCl	H ₂ O
Sol 1 (repeat from 4.7.2018)					
molar ratio	1.000	0.003	16.1	0.001	6.07
mmol	24.99	0.073	401.6	0.027	151.66
g	5.206	0.926	18.5	2.720	2.73
mL	5.538		12.6	0.0093 M	2.73
Φ pol = 12.16 %					

Samples were dip coated at 30 % RH (Samples: 31,32,33,35,36) or 50% (Sample: 34), 2.5 min at controlled RH after deposition and withdrawl speed of 0.15 mm/s (for Samples: 32, 36) or 1 mm/s (Samples 31, 33, 35). Post deposition heat treatment: x...RT, y...80°C, 12 h, z...400°C, 4 h; Exemplary thickness of samples: SSd31: x = 233 nm; y = 214 nm; z = 167 nm; SSd33: x = 213 nm; y = 220 nm; z = 180 nm; SSd35: x = 248 nm; y = 229 nm; z = 199 nm; All samples synthesized which showed reflexes in the X-ray diffraction pattern using sol compositions given in **Table 15** are given in **Figure 52**. For samples x..no heat treatment after deposition for y... heat treatment at 80° and for z...calcination 400°C 4 h.

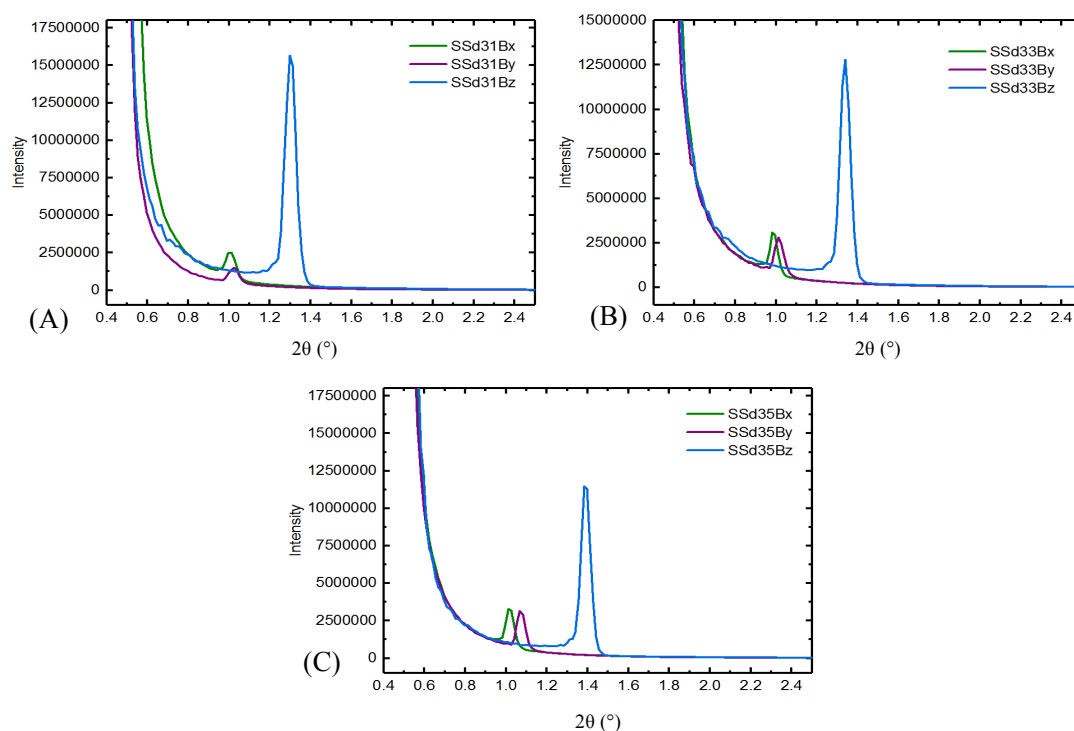


Figure 52: X-ray diffraction patterns of samples using sol compositions from Table 15: (A) SSd31B: (Sol 1, 3 h age, 1 mm/s, 2.5 min, 30% RH),; (B): SSd33B: (Sol 1, 3 h age, 1 mm/s, 1 min, 30% RH); (C): SSd35B: (Sol 1, 4 h age, 1 mm/s, 30% RH, 2.5 min);

All synthesized films at 30% RH and 1 mm/s withdrawl speed showed defined reflexes.

5.3.2 Synthesis of Silica Films Using F127 as Surfactant

Samples: SSd37B – SSd44B

For the synthesis towards higher film thickness the sol 10 mL of EtOH and TEOS and HCl were stirred at 50°C (Samples: 37, 38, 41, 42) and at 80°C (Samples: 39,40,43,44) for 1 h for sol formation without template. Polymer solution was prepared dissolving F127 in EtOH (see **Table 16**). Solutions were combined and slightly stirred for 2 h (Samples: 37–40), or 4 h (Samples: 41-44).

Table 16: Sol composition for the synthesis of mesoporous silica films using F127 and dip coating as deposition method. SSd37B – SSd44B (16.7.2018),

SSd37B-SSd44B , 16.7.2018					
	TEOS	F127	EtOH	HCl	H ₂ O
Sol 1					
molar ratio	1	0.0029	16.07	0.001	6.07
mmol	24.99	0.0735	401.6	0.0272	151.66
g	5.21	0.926	18.5	2.72	2.733
mL	5.54		12.6	0.0093 M	2.733
Φ pol = 12.16 %					

Samples were dip coated at 30 % RH, 1 min at controlled RH after deposition and with drawl speed of 1 mm/s (for Samples: 37, 39, 41, 43) or 2 mm/s (for Samples: 38,40,42,44).

Post deposition Heat treatment: x...RT, y...80°C, 12 h, z...400°C, 4 h; Exemplary thickness of samples: SSd37B: x = 309 nm; y = 246 nm; z = 156 nm; SSd42B: x = 330 nm; y = 240 nm; z = 220 nm; SSd44B: x = 356 nm; y = 345 nm; z = 250 nm; All samples synthesized which showed reflexes in the X-ray diffraction pattern using sol compositions given in **Table 16** are shown in **Figure 53**.

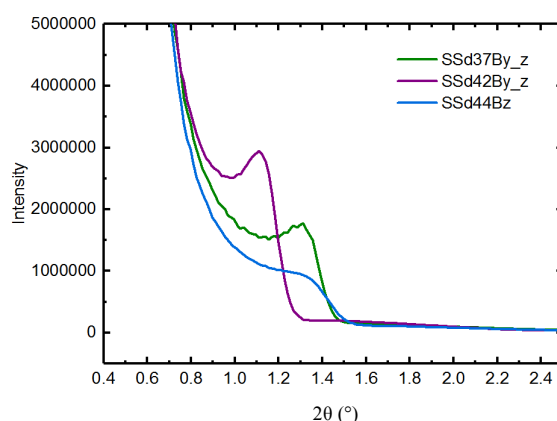


Figure 53: X-ray diffraction patterns of samples using sol compositions from Table 16 : SSd37B: (Sol 1, 50°C, 2 h age, 1 mm/s, 1 min, 30% RH), SSd42B: (Sol 1, 50°C, 4 h age, 1 mm/s, 1 min, 30% RH), SSd44B: (Sol 1, 80°C, 4 h age, 1 mm/s, 1 min, 30% RH),

5.3.3 Post-Synthesis Functionalization with HMDS

For the post-synthesis functionalization of the mesoporous silica films with HMDS, the chips were put into a round-necked flask, flushed 3 times with nitrogen and drying under vacuum at 120°C for 2 h. In nitrogen flow, dry acetone (15 mL) and HMDS (1.5 mL) were inserted. The solution was refluxed for 4 h. Films were subsequently washed with acetone and heated overnight at 110°C. Successful functionalization was verified by investigation with ATR FTIR (see **Figure 54**). Here the C-H vibrations $\sim 2900\text{ cm}^{-1}$ as well as the Si-C band at 1259 cm^{-1} are visible showing novel moieties on the surface.

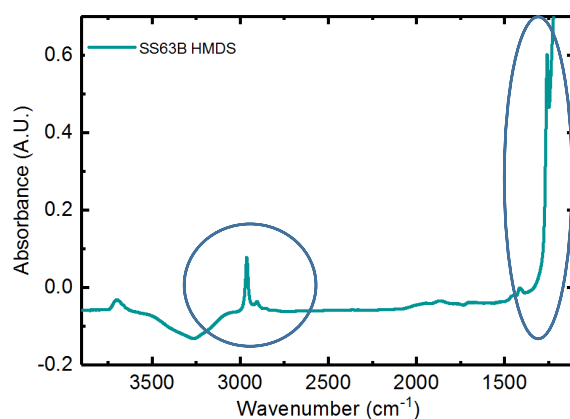


Figure 54: Spectrum of layer SS63B after functionalization with HMDS. Background spectrum uncoated silicon ATR crystal.

6. References

- [1] C. Lee, T. Lin, and C. Mou, “Mesoporous materials for encapsulating enzymes,” *Nano Today*, vol. 4, pp. 165–179, 2009.
- [2] C. Mateo, J. M. Palomo, G. Fernandez-lorente, J. M. Guisan, and R. Fernandez-lafuente, “Improvement of enzyme activity , stability and selectivity via immobilization techniques,” *Enzyme Microb. Technol.*, vol. 40, no. May, pp. 1451–1463, 2007.
- [3] S. Datta and L. R. Christena, “Enzyme immobilization : an overview on techniques and support materials,” *Biotechnology*, vol. 3, pp. 1–9, 2013.
- [4] P. M. Zdarta Jakub, Meyer S. Anne, Jesionowski Teofil, “A General Overview of Support Materials for Enzyme Immobilization: Characteristics, Properties, Practical Utility,” *Catalysts*, vol. 8, no. 92, p. 92, 2018.
- [5] S. P. Hudson *et al.*, “Proteins in mesoporous silicates,” *ACS Symp. Ser.*, vol. 986, pp. 49–60, 2008.
- [6] N. Carlsson, H. Gustafsson, C. Thörn, L. Olsson, K. Holmberg, and B. Åkerman, “Enzymes immobilized in mesoporous silica: A physical-chemical perspective,” *Adv. Colloid Interface Sci.*, vol. 205, pp. 339–360, 2014.
- [7] A. Katiyar, L. Ji, P. Smirniotis, and N. G. Pinto, “Protein adsorption on the mesoporous molecular sieve silicate SBA-15: Effects of pH and pore size,” *J. Chromatogr. A*, vol. 1069, no. 1, pp. 119–126, 2005.
- [8] M. Miyahara, A. Vinu, and K. Ariga, “Adsorption myoglobin over mesoporous silica molecular sieves : Pore size effect and pore-filling model,” *Mater. Sci. Eng. C*, vol. 27, pp. 232–236, 2007.
- [9] J. Deere, E. Magner, J. G. Wall, and B. K. Hodnett, “Adsorption and activity of proteins onto mesoporous silica,” *Catal. Letters*, vol. 85, no. 1–2, pp. 19–23, 2003.
- [10] D. Moelans, P. Cool, J. Baeyens, and E. F. Vansant, “Using mesoporous silica materials to immobilise biocatalysis-enzymes,” *Catal. Commun.*, vol. 6, pp. 307–311, 2005.
- [11] J. Lei *et al.*, “Immobilization of enzymes in mesoporous materials: Controlling the entrance to nanospace,” *Microporous Mesoporous Mater.*, vol. 73, no. 3, pp. 121–128, 2004.
- [12] C. Woo, M. Young, J. Bum, J. Kil, H. Kun, and E. Kyu, “Analysis of protein adsorption characteristics to nano-pore silica particles by using confocal laser scanning microscopy,” *J. Biotechnol.*, vol. 112, pp. 267–277, 2004.

-
- [13] M. Piras, A. Salis, M. Piludu, D. Steri, and M. Monduzzi, "3D vision of human lysozyme adsorbed onto a SBA-15 nanostructured matrix w," *Chem. Commun.*, vol. 47, pp. 7338–7340, 2011.
- [14] Z. Zhou and M. Hartmann, "Progress in enzyme immobilization in ordered mesoporous materials and related applications," *Chem. Soc. Rev.*, vol. 42, no. 9, pp. 3894–3912, 2013.
- [15] B. Baumgartner, J. Hayden, A. Schwaighofer, and B. Lendl, "In Situ IR Spectroscopy of Mesoporous Silica Films for Monitoring Adsorption Processes and Trace Analysis," *ACS Appl. Nano Mater.*, vol. 1, pp. 7083–7091, 2018.
- [16] J. Livage, M. Henry, and C. Sanchez, "Sol-Gel Chemistry of Transition Metal Oxides," *Prog. Solid State Chem.*, vol. 18, pp. 259–341, 1988.
- [17] N. H. Ulrich Schubert, *Synthesis of Inorganic Materials*, Third Edit. 2012.
- [18] B. C. J. Brinker, Y. Lu, A. Sellinger, and H. Fan, "Evaporation-Induced Self-Assembly : Nanostructures Made Easy **," *Adv. Funct. Mater.*, vol. 11, no. 7, pp. 579–585, 1999.
- [19] G. M. Whitesides, "Self-Assembly at All Scales," *Science*, vol. 2418, no. 2002, pp. 2418–2422, 2011.
- [20] D. Andrienko, "Introduction to liquid crystals," *J. Mol. Liq.*, vol. 267, pp. 520–541, 2018.
- [21] J. Rouquerol *et al.*, "Recommendations for the characterization of porous solids," *Pure Appl. Chem.*, vol. 66, no. 8, pp. 1739–1758, 1994.
- [22] D. Grosso *et al.*, "Fundamentals of mesostructuring through evaporation-induced self-assembly," *Adv. Funct. Mater.*, vol. 14, no. 4, pp. 309–322, 2004.
- [23] T. Schneller and R. Waser, *Chemical Solution Deposition of Functional Oxide Thin Films*. Springer Berlin Heidelberg, 2013.
- [24] D. R. Dunphy, P. H. Sheth, F. L. Garcia, and C. J. Brinker, "Enlarged pore size in mesoporous silica films templated by pluronic F127: Use of poloxamer mixtures and increased template/SiO₂ ratios in materials synthesized by evaporation-induced self-assembly," *Chem. Mater.*, vol. 27, no. 1, pp. 75–84, 2015.
- [25] P. Holmqvist, P. Alexandridis, and B. Lindman, "Modification of the Microstructure in Block Copolymer–Water–‘Oil’ Systems by Varying the Copolymer Composition and the ‘Oil’ Type: Small-Angle X-ray Scattering and Deuterium-NMR Investigation," *J. Phys. Chem. B*, vol. 102, no. 7, pp. 1149–1158, 1998.
- [26] G. L. Athens, R. M. Shayib, and B. F. Chmelka, "Current Opinion in Colloid &
-

- Interface Science Functionalization of mesostructured inorganic – organic and porous inorganic materials,” *Curr. Opin. Colloid Interface Sci.*, vol. 14, no. 4, pp. 281–292, 2009.
- [27] C. LibreTexts, “Electromagnetic Spectrum.” [Online]. Available: [https://chem.libretexts.org/Bookshelves/Physical_and_Theoretical_Chemistry_Textbook_Maps/Map%3A_Physical_Chemistry_\(McQuarrie_and_Simon\)/13%3A_Molecular_Spectroscopy/13-01._Different_Regions_of_the_Electromagnetic_Spectrum_Are_Used_to_Investigate_Different_Molecular_Processes](https://chem.libretexts.org/Bookshelves/Physical_and_Theoretical_Chemistry_Textbook_Maps/Map%3A_Physical_Chemistry_(McQuarrie_and_Simon)/13%3A_Molecular_Spectroscopy/13-01._Different_Regions_of_the_Electromagnetic_Spectrum_Are_Used_to_Investigate_Different_Molecular_Processes).
- [28] A. Beer, “Bestimmung der Absorption des rothen Lichts in farbigen Flüssigkeiten,” pp. 78–88, 1852.
- [29] P. R. Griffiths, *Fourier Transform Infrared Spectrometry*, Second Edi. WILEY-VCH Verlag, 2007.
- [30] G. Ramer and B. Lendl, “Attenuated Total Reflection Fourier Transform Infrared Spectroscopy,” *Encycl. Anal. Chem.*, 2013.
- [31] F. Mirabella, *Internal Reflection Spectroscopy*, vol. 21. 1985.
- [32] D. L. Nelson, M. M. Cox, and W. H. Freeman, *Principles of Biochemistry*, Fifth. Lehninger, 2008.
- [33] A. ELLIOTT and E. J. AMBROSE, “Structure of Synthetic Polypeptides,” *Nature*, vol. 165, p. 921, Jun. 1950.
- [34] A. Barth, “Infrared spectroscopy of proteins,” *Biochim. Biophys. Acta - Bioenerg.*, vol. 1767, no. 9, pp. 1073–1101, 2007.
- [35] H. Fabian and D. Naumann, *Protein Folding and Misfolding*. 2012.
- [36] A. Schwaighofer, M. R. Alcaráz, C. Araman, H. Goicoechea, and B. Lendl, “External cavity-quantum cascade laser infrared spectroscopy for secondary structure analysis of proteins at low concentrations,” *Sci. Rep.*, vol. 6, no. August, pp. 1–10, 2016.
- [37] A. Vinu, V. Murugesan, and M. Hartmann, “Adsorption of lysozyme over mesoporous molecular sieves MCM-41 and SBA-15: Influence of pH and aluminum incorporation,” *J. Phys. Chem. B*, vol. 108, no. 22, pp. 7323–7330, 2004.
- [38] R. Fernandez-Lafuente, P. Armisen, P. Sabuquillo, G. Fernández-Lorente, and J. M. Guisán, “Immobilization of lipases by selective adsorption on hydrophobic supports,” *Chem. Phys. Lipids*, vol. 93, no. 1–2, pp. 185–197, 1998.
- [39] A. Vinu *et al.*, “Lysozyme adsorption onto mesoporous materials: Effect of pore geometry and stability of adsorbents,” *J. Nanosci. Nanotechnol.*, vol. 7, pp. 828–832,
-

-
- 2007.
- [40] S. Gao, Y. Wang, X. Diao, G. Luo, and Y. Dai, “Effect of pore diameter and cross-linking method on the immobilization efficiency of *Candida rugosa* lipase in SBA-15,” *Bioresour. Technol.*, vol. 101, no. 11, pp. 3830–3837, 2010.
 - [41] C. Lipase, P. Grochulskisq, J. D. Schrags, F. Bouthilliers, P. Smithll, and D. Harrisonll, “Insights into Interfacial Activation from an Open Structure of,” vol. 268, no. 17, pp. 12843–12847, 1993.
 - [42] F. Hasan, A. A. Shah, and A. Hameed, “Industrial applications of microbial lipases,” *Enzyme Microb. Technol.*, vol. 39, no. 2, pp. 235–251, 2006.
 - [43] K.-E. Jaeger and T. Eggert, “Lipases for biotechnology,” *Curr. Opin. Biotechnol.*, vol. 13, no. 4, pp. 390–397, 2002.
 - [44] S. P. Naik, S. Yamakita, M. Ogura, and T. Okubo, “Studies on mesoporous silica films synthesized using F127, a triblock co-polymer,” *Microporous Mesoporous Mater.*, vol. 75, no. 1–2, pp. 51–59, 2004.
 - [45] S. Besson, T. Gacoin, C. Ricolleau, C. Jacquiod, and J.-P. Boilot, “Phase diagram for mesoporous CTAB–silica films prepared under dynamic conditions,” *J. Mater. Chem.*, vol. 13, no. 2, pp. 404–409, 2003.
 - [46] M. Matheron *et al.*, “Highly ordered CTAB-templated organosilicate films,” *J. Mater. Chem.*, vol. 15, no. 44, pp. 4741–4745, 2005.
 - [47] D. Grosso and P. Marie, “How to exploit the full potential of the dip-coating process to better control film formation,” pp. 17033–17038, 2011.
 - [48] M. Stoytcheva, G. Montero, R. Zlatev, J. Á. León, and V. Gochev, “Analytical methods for lipases activity determination : A review Analytical Methods for Lipases Activity Determination : A Review,” no. January 2012, 2014.
-